Powerful diode-pumped ultrafast solid-state laser oscillators based on bulk Yb:$KGd(WO_4)_2$ crystals

by

Haitao Zhao

A Thesis submitted to the Faculty of Graduate Studies of
The University of Manitoba
in partial fulfilment of the requirements of the degree of

DOCTOR OF PHILOSOPHY

Department of Electrical and Computer Engineering
University of Manitoba
Winnipeg

Abstract

Yb-ion doped gain media have become the material of choice for reliable generation of ultrashort pulses at wavelength around 1 μm. This can be attributed to their excellent lasing properties, broad emission bandwidths and compatibility with diode pumping. However, operation at high average power (>1 W) with sub-100 fs pulses still remains quite challenging. The efforts of developing an Yb-ion oscillator towards this goal, therefore, are the main focus of this thesis.

In this work, the commercially available Yb:$KGd(WO_4)_2$ (Yb:KGW) crystals were chosen to serve as the gain media. To achieve high power operation, the thermal issues and the intracavity losses are the two fundamental factors that one has to carefully consider. In this thesis, a new pumping scheme was proposed to alleviate the thermal issues in the Yb:KGW crystal. As the traditional methods have limitations to characterize the intracavity losses in the broadband Yb-ion oscillators, a new method was introduced in this work. By using it with a continuous wave (CW) Yb:KGW laser oscillator, this method was proved to be simple, dynamic and accurate. As a side effect in the process of optimizing the CW operation, a bistable regime with simultaneous two-wavelength emission was observed. Reasons of this bistable operation were discussed based on the understanding of the thermal effects and the loss mechanism in the Yb-ion oscillators.

With the knowledge and experimental understanding of the fundamental issues in laser oscillators operated in the CW regime, the next step of our work was concentrated on their operation in a pulsed regime. The pulsed operation was initiated by incorporating a semiconductor saturable absorber mirror (SESAM) and was stabilized by adjusting the laser cavity to achieve the optimized Kerr-lens mode locking. This dual action of the Kerr-lens and saturable absorber (KLAS) mode locking resulted in greatly enhanced performance. The laser delivered pulses with 67 fs duration at a repetition rate of 77 MHz. The average output power reached 3 W, corresponding to >38 nJ of pulse energy and >570 kW of peak power. To the best of our knowledge, this is the highest average output power produced to date from Yb-ion based bulk lasers with such a short pulse duration. The scalability of pulse energy and peak power was also demonstrated by

reducing the repetition rate to either 36 MHz or 18 MHz. The cavity with latter repetition rate produced 85 fs pulses with the pulse energy up to 83 nJ, which corresponds to a peak power as high as 1 MW.

The developed lasers had a fixed wavelength at around 1 μm. Many applications, however, require wavelength tunability. The wavelength of the generated pulses can be tuned in the near-infrared region by coupling them into an optical parametric oscillator (OPO). The feasibility of the wavelength tuning was demonstrated in the last part of this thesis, through a thorough theoretical analysis of three OPO materials suitable for excitation at 1.04 μm.

Acknowledgments

First of all, I would like to give my greatest thanks to my supervisor Prof. Arkady Major, who provided me with this valuable opportunity to engage in such an interesting and important research project. Through my years working with him, I have gained a lot from him, not only the professional knowledge but also his patience and positive attitude towards scientific research. I really appreciate his guidance and contribution in the success of this research as well as his support and help in my daily life in Canada.

I wish to express my gratitude to my committee members Prof. Sherif Sherif and Prof. Jitendra Paliwal for their helpful discussion and advices on the whole project and the formation of this thesis. A special thank you should go to Prof. Ivan T. Lima Jr. from the North Dakota State University for his detailed suggestions on the theoretical research of the optical parametric oscillators.

I would like to thank the University of Manitoba for awarding me the graduate fellowship, the international graduate student scholarship, and the financial support for attending academic conferences.

I really enjoyed the time spent working with my colleagues Dr. V. M. Collado, K. Sukhoy, L. Mostaco-Guidolin, S. Manjooran, S. Ghanbari, R. Akbari, H. Mirzaeian, T. Waritanant, E. Alimohammadian, and A. Sherniyozov. I learned a lot through fruitful discussions with them. A sincere thank you goes to all my friends in Winnipeg for bringing me so many joyful moments worth to remember.

Finally, I would like to give my deepest appreciation to my wife Hong Xiao. Thank you for your understanding, company and giving me the most valuable gift in my life – my little boy Nathan – during the writing up of this thesis.

Table of Contents

List of symbols and abbreviations

Symbols

α	Absorption coefficient
β	Fractional population inversion
c	The speed of light
d_{eff}	Effective nonlinear coefficient
δ_{reabs}	Reabsorption loss
D_{th}	Photorefractive damage threshold
ε_0	Vacuum permittivity
E	Electrical field of the light
E_{in}	Intracavity energy
E_p	Pulse energy
$E_{sat,G}$	Saturation energy of the gain medium
$E_{sat,A}$	Saturation energy of the absorber
f	Repetition rate
f_u	Fractional population in the upper energy state
f_l	Fractional population in the lower energy state
g	Gain coefficient
h	Plank constant
I	Intensity
k	Wave vector
λ	Wavelength
Λ	Grating period
l_c	Crystal length
L	Single-trip cavity length
L_{in}	Intracavity loss
υ_p	Frequency of pump light
n	Index of refraction
n_2	Nonlinear index of refraction

N_0	Doping concentration
ω	Angular frequency
P	Polarization
P_0	Pump power
P_{abs}	Absorbed pump power
P_{ave}	Average output power
P_{peak}	Peak power
P_{th}	Threshold pump power
q	Quantum defect
r	Radius of curvature
R_{oc}	Output coupler reflectivity
σ_{abs}	Absorption cross section
σ_{em}	Emission cross section
τ_f	Lifetime of upper energy state
τ_p	Pulse duration
T	Temperature
T_{oc}	Output coupler transmission
v	Group velocity
V_{co}	Coercive field
w_p	Pump spot radius
w_L	Laser mode radius
χ	Susceptibility

Abbreviations

AR	Antireflection
BPM	Birefringent phase-matching
CW	Continuous wave
FEA	Finite element analysis
FWHM	Full width at half maximum
HR	High reflection

KLM	Kerr-lens mode locking
KLAS	Kerr-lens and saturable absorber
GTI	Gires–Tournois interferometer
GVD	Group velocity dispersion
GVM	Group velocity mismatch
ML	Mode locking
MPC	Multipass cell
OC	Output coupler
PBS	Polarizing beamsplitter cube
OPO	Optical parametric oscillator
QML	Q-switched mode-locking
QPM	Quasi-phase-matching
SAM	Self-amplitude modulation
SPM	Self-phase modulation
SESAM	Semiconductor saturable absorber mirror

List of Figures

List of Tables

Chapter 1

Introduction and background

1.1 Ultrafast lasers: split a second into 1000000000000000 pieces!

As early as in the year of 1878, driven by a wager on whether all the four hooves of a galloping horse are lifted simultaneously off the ground, the innovative photographer Eadweard Muybridge took a series of snapshots, each of which froze a motion of the horse in one thousandth of a second (Fig. 1.1). These unprecedented images exposed an entirely unique world that would otherwise pass too fast to be followed by human eyes. In the present days, one thousandth of a second has been quite a long period of time with respect to the modern technologies. A fast mechanical shutter or an instant flash of a strobe light can freeze the time in 1/40,000 of a second, which can provide us a clear visualization of many fast-moved objects such as the darting bullets, popping balloons, and the splashing water to name a few.

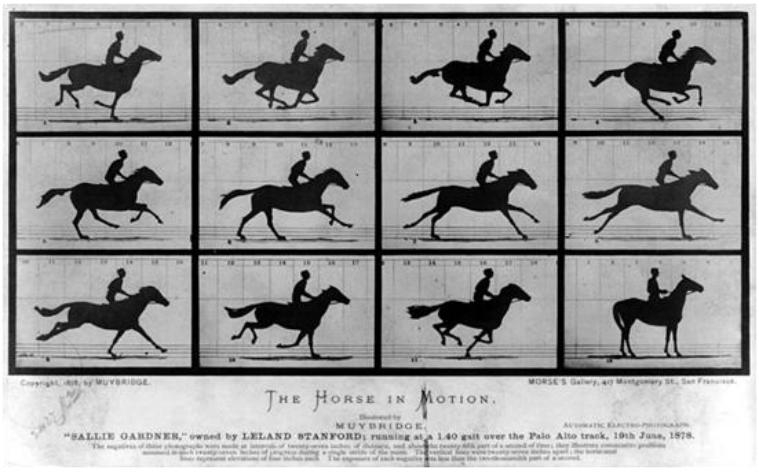

Fig. 1.1. The famous photographs named "the horse in motion" taken by Eadweard Muybridge in 1878, showing the detailed gait of a galloping horse in 1/1000 second.

Shortly after the advent of the first laser in the early 1960s [1], the ultrafast lasers became available. The shortest time period that can be controlled by human beings was then brought down to a previously untouchable level. With the modern mode locking

technology (Section 5.1), a laser pulse could only occupy a few pieces if a second is split into 10^{15} of them! In other words, the time involved in a laser pulse is only on the order of a femtosecond.

1.2 What can we do with ultrafast pulsed lasers?

Since an ultrafast pulse defines an event that occurs within an extremely short time window, it seems quite naturally that the first thing to come to mind is to use it to probe really fast-moving objects – just like using an instant flash of strobe to freeze a darting bullet but in a much shorter time domain. One important example of the fast-moving objects is of a chemical reaction. With an ultrafast laser, the scientists now are able to freeze the motions of the particles and "see" those elementary chemical processes in real time [2].

As the lasing energy is confined in a femtosecond time period, the peak power of each individual laser pulse can reach to a very high value. Tightly focusing of a femtosecond laser beam into a matter can give rise to a nonlinear response but only within the tiny focal volume where the peak intensities are the highest. By scanning the laser beam across the sample and collecting the nonlinear signal point by point, a high-resolution 3D image can be built up. This imaging technique, i.e. the so-called nonlinear microscopy [3-4], holds many advantages such as deep and noninvasive penetration, making it particularly suited for visualizing of living biological tissues at scales ranging from a single molecule to the whole surface of an organism with a penetration depth of hundreds of microns (Fig. 1.2).

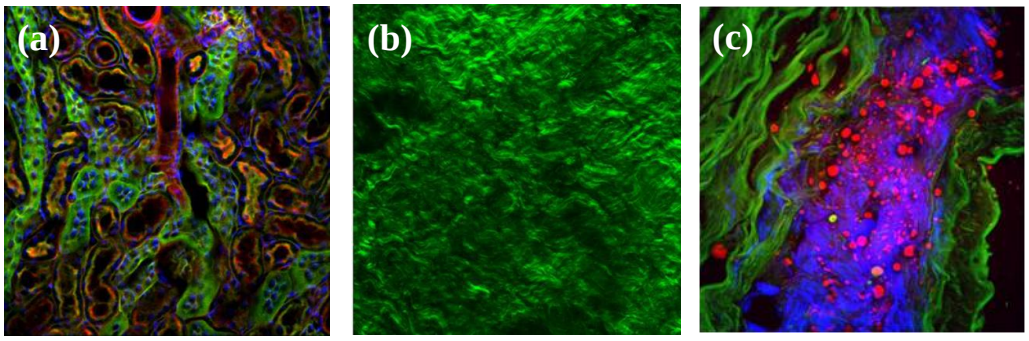

*(a) and (b): Reprinted by permission from Macmillan Publishers Ltd: A. M. Larson, "Multiphoton microscopy," Nat. Photonics **5**, (2011), copyright 2010.*
(c): Reprinted by permission from The Optical Society: A. F. Pegoraro, A. Ridsdale, D. J. Moffatt, Y. Jia, J. P. Pezacki, and A. Stolow, "Optimally chirped multimodal CARS microscopy based on a single Ti:sapphire oscillator," Opt. Express 17, 2984-2996 (2009), copyright 2009.

Fig. 1.2. (a) Two-photon fluorescence imaging of a mouse kidney labeled with different fluorescent dyes [3]. (b) Image of collagen in chicken skin obtained from a second harmonic generation (SHG) microscopy [3]. (c) Image of rabbit aorta obtained from a multimodal nonlinear microscopy: lipids (red) from coherent anti-Stokes Raman scattering microscopy, collagen (blue) from SHG microscopy and muscle elastin (green) from two-photon fluorescence microscopy [4].

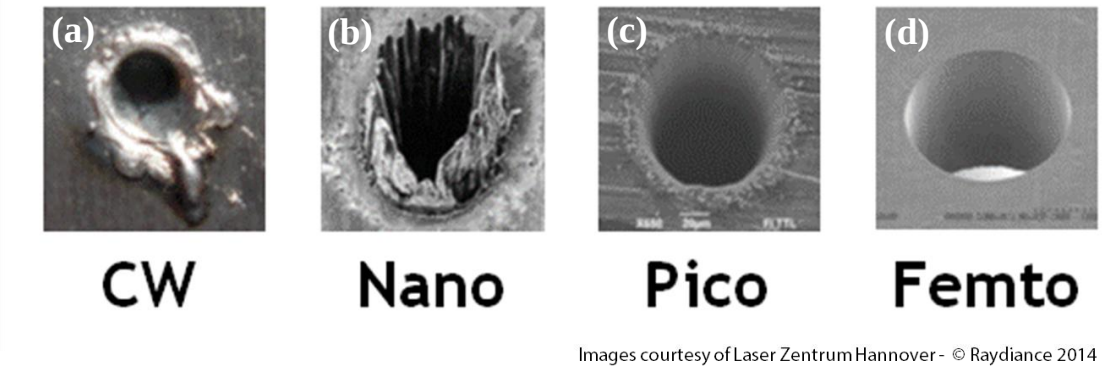

Fig. 1.3. Comparison of laser drilling with continuous wave (a), nanosecond pulses (b), picosecond pulses (c) and femtosecond pulses (d).

At peak intensities above 10 TW/cm^2, the irradiated materials will experience a series of stronger nonlinear responses, which finally will give rise to a permanent modification or removal of the materials. The removal happens so fast that the heat has no time to diffuse out of the focal volume, leaving a very clean and highly precise processing area with sub-micrometer accuracy (Fig. 1.3). When applied to the biomedical tissues, the femtosecond lasers have been able to provide safe, bladeless and precise ophthalmic surgeries [5] and even surgeries conducted within a cell are possible [6].

When it comes to the frequency domain, the short time scale of the pulses implies their broad spectral bandwidth. The spectrum of a well-stabilized ultrafast laser actually contains hundreds of thousands of equally spaced sharp spectral lines, making them naturally suitable to be exploited as frequency combs, which play an important role in precision frequency metrology, optical atomic clock, spectroscopy (Fig. 1.4 (a)) and astronomy [7-9]. By coupling the femtosecond pulses into a microstructure fiber, the spectrum can be stretched to several hundreds of nanometers, leading to the generation of supercontinuum light sources. These sources are perfectly fit for ultra-high axial resolution optical coherence tomography (Fig. 1.4 (b)) and high-speed telecommunications [10-11].

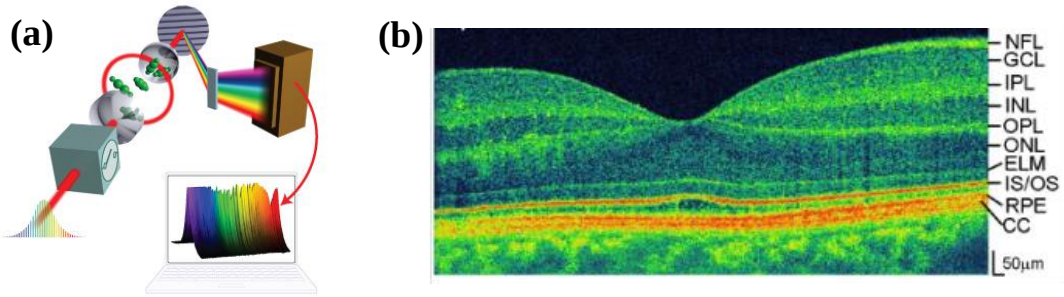

(a) Image courtesy of the Ye Research Lab, JILA, NIST, and the University of Colorado.

(b) Reprinted by permission from The Optical Society: M. Wojtkowski, V. J. Srinivasan, T. H. Ko, J. G. Fujimoto, A. Kowalczyk, and J. S. Duker, "Ultrahigh-resolution, high - speed, Fourier domain optical coherence tomography and methodsfor dispersion compensation," Opt. Express 12, 2404-2422 (2004),

Fig. 1.4. (a) Molecular fingerprinting. (b) Ultrahigh-resolution optical coherence tomography image of human macula obtained by using broadband pulses as a light source [10].

The applications listed above are merely the tip of an iceberg compared to the huge application potential of the ultrafast lasers. With the improvement of the lasing performance, reduction of cost and commercial availability, the ultrafast lasers will stretch their arms into more scientific and industrial fields. On the other hand, the rapidly growing demand for ultrafast lasers in turn will largely promote their technological advances.

1.3 Overview of the Yb-ion ultrafast lasers

In this section, a brief review of the Yb-ion ultrafast lasers is given by highlighting the features of different Yb-doped gain media and by summarizing the laser performance obtained from these Yb-doped gain media.

1.3.1 Why Yb-ion ultrafast lasers?

Since the mode locking technique, which is the ultrashort pulse shaping mechanism, was demonstrated in 1964 [12], the ultrafast lasers underwent several remarkable revolutions. One of the most important aspects in the revolution was development of the new laser gain media. Many of the early efforts were concentrated on the dye solutions. However, the short lifetime and strong toxicity of the dye molecules destined them to be eventually replaced by the Ti:sapphire crystals [13], which soon became the routinely used gain media in the realm of ultrafast lasers. The Ti:sapphire crystals, on one hand, have very broad emission spectrum with more than 300 nm of bandwidth, which is sufficient to support the generation of sub-10-fs pulses [14-15]. On the other hand, they require green pumping lasers such as argon-ion lasers or frequency-doubled neodymium-ion solid-state lasers, which are either inefficient or expensive. Moreover, the Ti:sapphire crystals have large quantum defect, which indicates the large energy mismatch between the pump and laser photons. This creates a lot of waste heat during the lasing process, leading to the reduced efficiency and output power capacity. For many applications where high power (or energy) is required, one has to resort to the complicated and expensive amplification systems [16-17].

In the past decade, accompanying the development of Ti:sapphire ultrafast oscillators, another branch based on the Yb-ion doped materials have received increased interest. Unlike the Ti:sapphire crystals, Yb-doped materials can be directly pumped by the high power semiconductor diode lasers at a wavelength around 980 nm. This gives them a significant advantage towards achieving powerful, compact and inexpensive ultrafast lasers. Moreover, the Yb-doped materials have much smaller quantum defect (<10%) when compared to that of the Ti:sapphire crystals (~35%), resulting in a lower level of thermal issues and greatly enhanced lasing efficiency. Besides, they posses many favourable lasing properties, such as large emission cross section, broad gain spectrum and absence of excited-state absorption, all of which make the Yb-ion ultrafast lasers a promising branch in the realm of ultrafast lasers.

1.3.2 Features of different Yb-doped gain media

The Yb-ion ultrafast lasers have experienced more than two decades of development. In the first decade, research activities were mainly concentrated on two materials: Yb:$Y_3Al_5O_{12}$ (Yb:YAG) and Yb:glass (such as Yb:phosphate, Yb:silicate and Yb:fluoride) [18]. Both of these materials have their advantages and serious drawbacks. Yb:YAG crystals have high emission cross section (~2×10^{-20} cm^{-2}) and large thermal conductivity (~6 $Wm^{-1}K^{-1}$). These two factors are beneficial for their low lasing threshold, high lasing efficiency and power scalability. However, very short pulses are difficult to generate using Yb:YAG crystals because of their narrow spectral bandwidth (~6 nm). The Yb:glasses, in contrast, have the very opposite properties: broad spectral bandwidth (>30 nm) but low emission cross section (~0.1×10^{-20} cm^{-2}) and small thermal conductivity (~1 $Wm^{-1}K^{-1}$). The breakthrough of this dilemma came in the second decade with the prosperity of a wealth of Yb-doped crystals and ceramics, including Yb:tungstates, Yb:silicates, Yb:sesquioxides, Yb:vanadates, Yb:borates and so on. Strongly affected by the nature of the hosts, the Yb-ions exhibit very different spectral, thermal and mechanical properties, therefore resulting in a varied laser performance. Below I will provide a summary of the most important properties of these laser crystal families.

(a) Yb:tungstates

Yb:tungstates (Yb:$KRe(WO_4)_2$ Re=Y, Gd or Lu) are an important family that have received much attention because of their favorable spectroscopic properties and fairly good thermal conductivity. In fact, the Yb:KGW and Yb:KYW crystals have the largest emission cross section (~3×10^{-20} cm^{-2}) among the broadband Yb-doped materials. The thermal conductivity of Yb:tungstates (~3.5 $Wm^{-1}K^{-1}$) is about twice lower than that of the Yb:YAG crystals, but is four times higher compared to the thermal conductivity of Yb:glass, thus allowing a relatively efficient heat removal at high pump power levels [19]. With their fairly broad spectral bandwidth (~25 nm), pulses as short as 65 fs and 100 fs have been demonstrated from Yb:KYW and Yb:KGW oscillators respectively [20-21]. In these two cases, the average output power was limited to 182 mW for the former and 120 mW for the latter. Significant power scaling of the Yb:KGW oscillator was achieved by pumping the crystal with two powerful laser diode modules. Output power of 10 W with a pulse duration of 290 fs was produced [22]. Further power scaling was realized by using Yb:KYW and Yb:KLuW crystals with the thin-disk geometry (see appendix A), resulting in 240 fs pulses with 22 W of average power for the former and 440 fs pulses with 25 W of output power for the later [23-24].

(b) Yb:sesquioxides

Yb:sesquioxides (Yb:Re_2O_3, Re=Y, Sc or Lu) are very attractive for high power generation because of their superior thermo-mechanical properties. Among them the Yb:Lu_2O_3 crystals are the most prominent ones because their thermal conductivity can be maintained almost constantly with the increase of the Yb-ion doping level. Thermal conductivity of the Yb:Lu_2O_3 crystals with 2.7 at.% doping can be as high as 11 $Wm^{-1}K^{-1}$, which is about twice higher in comparison with Yb:YAG crystals [25]. When combined with the thin-disk technique, the heat load can be removed very efficiently, resulting in an output power of 141 W with a pulse duration of 738 fs [25]. Very similar to the Yb:YAG crystals, the spectral bandwidth of Yb:sesquioxides is quite narrow. To overcome this drawback, one strategy is to use the mixed crystal of Yb:$LuScO_3$, whose emission spectrum can be broadened inhomogeneously by their disordered lattice structure. Pulses with 74 fs duration and 40 mW of output power have been delivered from a bulk

Yb:$LuScO_3$ crystal, and pulses with 235 fs and 23 W of output power have been obtained from a thin-disk Yb:$LuScO_3$ laser [26-27]. Another strategy for broadening the spectral bandwidth is to use multiple gain media in a single oscillator. By combining the Yb:Sc_2O_3 and Yb:Y_2O_3 ceramics, 66 fs pulses with 1.5 W of average power were demonstrated [28].

(c) Yb:vanadates

Yb:vanadates (Yb:$ReVO_4$, Re=Y, Lu, and Gd) are known for their broad spectral bandwidth (>30 nm) and large nonlinear index of refraction. The latter feature makes them well-suited to be used in the Kerr-lens mode locking (Section 5.1), which can further broaden the spectral bandwidth through self-phase modulation (SPM). Although the Yb:vanadates have comparably large thermal conductivity, they usually suffer from low emission cross section and high reabsorption losses (Section 2.1), which limit their capability for high power operation. So far, pulses with 61 fs and 58 fs of duration have been delivered from Yb:YVO_4 and Yb:$LuVO_4$ crystals, respectively. The average powers, however, were only limited to 54 mW for the former and 85 mW for the later [29-30].

(d) Yb:silicates and Yb:borates

Many crystals included in the Yb:silicates and Yb:borates families exhibit a similar feature: highly disordered lattice structure, which largely benefits their extremely broad spectral bandwidth compared to other Yb-doped crystals. In fact, some of them such as Yb:$SrY_4(SiO_4)_3O$ (Yb:SYS), Yb:$GdYSiO_5$ (Yb:GYSO), Yb:$Sr3Y(BO_3)_3$ (Yb:BOYS) and Yb:$LaSc_3(BO_3)_4$ (Yb:LSB) have emission spectra with more than 60 nm of bandwidth, making it easy for them to deliver pulses with less than 100 fs of duration [31-34]. For example, pulses with as short as 58 fs and 70 fs durations have been extracted from oscillators based on Yb:LSB and Yb:SYS crystals, respectively [31, 34]. It is worth to note that, very recently, pulses with 35 fs duration were delivered from an Yb:YCOB oscillator with external pulse compression (47 fs directly from the oscillator) [35].

Besides the broad spectral bandwidth, the large Stark splitting of the ground energy manifold of the Yb:silicates crystals can reduce the undesired reabsorption losses, therefore resulting in reduced threshold pump intensity and enhanced lasing efficiency. The minimum pump intensity (a.k.a. transparency intensity) required for Yb:GSO

crystals, for instance, is as low as 0.15 kW/cm^2, which is several times lower than for other Yb-doped crystals [36].

(e) Yb:CALGO crystals

Crystal of the Yb:$CaGdAlO_4$ (Yb:CALGO) is quite a unique candidate that has become the object of intensive investigations in recent years. The disordered substitution of Yb ions to Ca and Gd ions not only inhomogeneously broadens the emission spectrum to 80 nm wide, but also gives rise to a gain plateau in the 1000-1050 nm wavelength range, making Yb:CALGO a very attractive material to produce pulses with sub-50 fs in duration [37]. In 2012, A. Agnesi *el al.* delivered 40 fs pulses with 15 mW of output power from a semiconductor saturable absorber mirror (SESAM) mode-locked (see Chapter 5) Yb:CALGO oscillator with external compression [38]. Very recently, the pulse duration has been brought down to 32 fs as a Kerr-lens mode-locked Yb:CALGO oscillator with external compression was developed. While pumped by a single-mode fiber laser (instead of a multi-mode diode laser), this oscillator has demonstrated so far the shortest pulses generated from the Yb-ion oscillators [39]. Power scaling is possible for this crystal because of its large thermal conductivity (>6.3 $Wm^{-1}K^{-1}$), which is similar to that of Yb:YAG crystals [37]. A remarkable power scaling was achieved by Greborio *et al.* in 2012, reaching 12.5 W of average power with a pulse duration of 94 fs [40]. With the thin-disk geometry, 300 fs pulses with 28 W of output power and 62 fs pulses with 5 W of output power have been demonstrated [41-42].

1.3.3 Summary – the goal of this thesis

In this subsection, I summarized the laser properties of different Yb-doped materials. This can provide us a guideline in the selection of the gain medium. The goal of this thesis will then be concluded from a summary of the previously reported laser performance.

In Fig. 1.5, four important properties: emission cross section, spectral bandwidth, thermal conductivity and transparency intensity are presented. As was mentioned, large emission cross section and high thermal conductivity are beneficial for power scaling. Broad spectral bandwidth is necessary for pulse shortening. Low transparency intensity is desired for obtaining a low threshold and highly efficient lasing process.

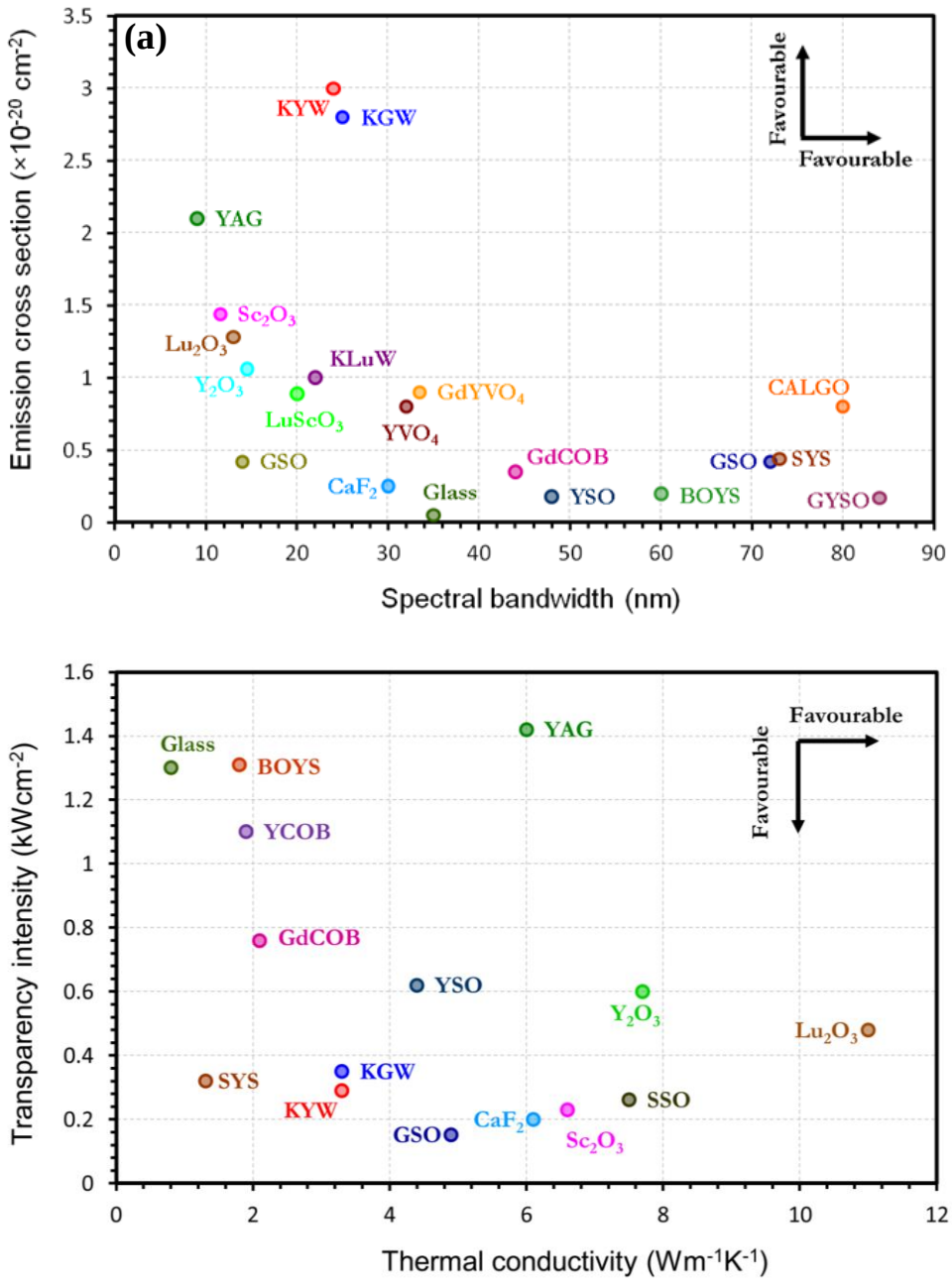

Fig. 1.5. Laser properties of different Yb-doped materials: (a) spectral bandwidth and emission cross section; (b) thermal conductivity and transparency intensity. All the values can be found in [18, 32, 36, 43-57].

Fig. 1.6 presents a summary of the literature results in terms of the average output power and the pulse duration achieved from different Yb-doped materials. Pulses with <100 fs of duration have been delivered from many of the Yb-doped materials. However, in most of the cases, the average output power of the pulses with such a short duration was limited and was in the range from several tens of mW to several hundreds of mW. Power scaling beyond this range has been achieved but largely at the expense of the pulse duration. Clearly, it is still quite challenging to obtain high output power (>1 W) while keeping the pulse duration at a short level (<100 fs). One reason is tied to the fact that some properties like the spectral bandwidth (for pulse shortening) and the thermal conductivity (for power scaling) are typically contradictory to each other. Another reason arises from the compromised performance of the current mode locking techniques (details on this point will be discussed in Chapter 5). These issues were addressed to some extent by combining Yb:Y_2O_3 and Yb:Sc_2O_3 ceramics (dual gain) in a single oscillator based on Kerr-lens mode locking. Pulses with 66 fs in duration and 1.5 W of average output power were demonstrated [28]. Very recently, two atypical materials, Yb:CaF_2 and Yb:CALGO, were employed and have shown quite promising performance: pulses with 75 fs duration and 2.3 W average output power from the former, and pulses with 62 fs duration and 5.1 W average output power from the latter [42, 58] were demonstrated. It should be noted that the latter case was based on the thin-disk technique, which requires quite complex configuration.

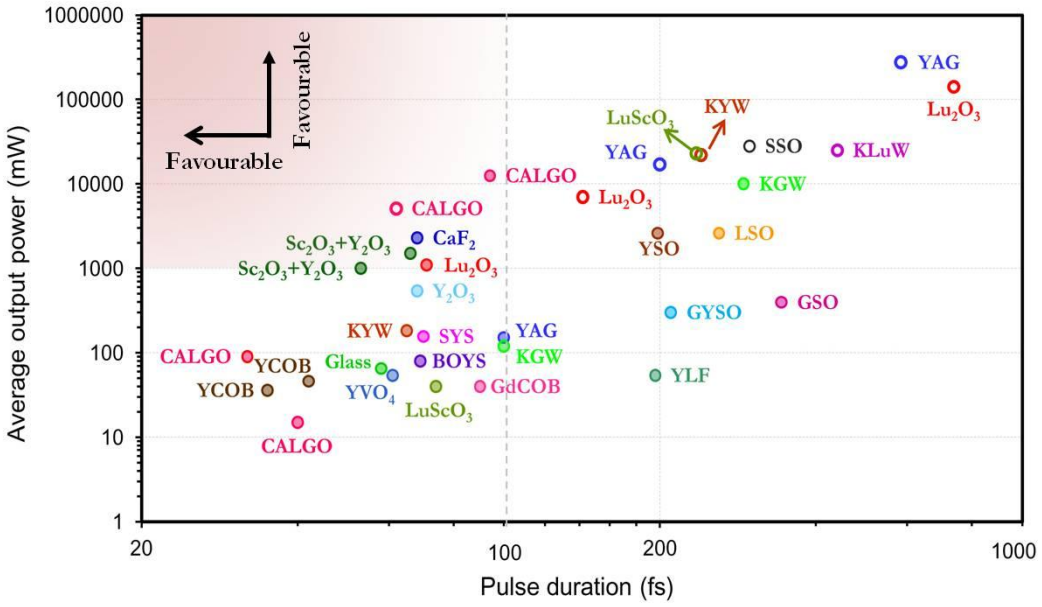

Fig. 1.6. Previously reported diode-pumped laser performance for different Yb-doped materials (Yb:CaF_2 and Yb:CALGO with 32 fs pulse duration were pumped by Yb-doped single-mode fiber lasers). The solid dots are the oscillators with bulk crystals and the hollow dots are those with thin-disk crystals. This figure is plotted based on the results in refs. [20-25, 26-29, 31, 33, 35, 38-40, 42, 44, 58-69].

In this context, the main purpose of this thesis was to develop simple and compact Yb-ion bulk oscillators that scale the average output power to a higher level while keeping the pulse duration short. Short pulse duration is desirable for many applications since it gives rise to a high peak power. The high average output power makes them well-suited, for example, to drive subsequent systems such as second harmonic generation and optical parametric oscillators for continuous wavelength tuning in both visible and infrared ranges.

In the whole work presented in this thesis, the Yb:KGW crystal was chosen as the gain medium. Our motivation for using the Yb:KGW laser crystal comes from the fact that it has one of the highest emission cross-sections (2.8×10^{-20} cm^2), fairly broad amplification bandwidth (>20 nm), and relatively high thermal conductivity (~3.3 $Wm^{-1}K^{-1}$) (Fig. 1.5) [19]. High average output power in the continuous wave and mode-locked regimes (10 W) was demonstrated [22] and the shortest reported pulses (100 fs) [21] were not limited by the available gain bandwidth (Fig 1.6). In addition, the crystal is characterized by a high

value of the nonlinear index of refraction [70] and absence of two-photon absorption at 1 μm wavelength [71], all of which contributes to the efficient Kerr lensing both at low and high intensities.

1.4 Organization of this thesis

The work presented in this thesis is partially based on several journal publications. The organization of this thesis is graphically represented in Fig. 1.7. The goal of this work was the development of powerful pulsed laser oscillators. This resembles the blossom of a flower, which requires the support of fertile soil, firm roots and a strong stem. Similarly, the whole work presented in this thesis was based on the background knowledge of mode locking and the overall understanding of current development of Yb-ion ultrafast lasers (like the soil). Development of a high power femtosecond laser oscillator necessitates the development of a powerful laser oscillator in continuous wave regime (like the stem), operation of which is based on solid understanding and characterization of fundamental issues like thermal lensing and intracavity losses (i.e. the roots). During the development of a continuous wave laser oscillator, there were many interesting phenomena that were worth to investigate (like the leaves). Among them, we studied the simultaneous dual-wavelength operation of a CW laser oscillator. The developed pulsed lasers will further be applied to pump optical parametric oscillators for wavelength tuning. This is graphically depicted as a bee collecting the pollen from the flower to transform it into a honey later on. The related background knowledge in each chapter will be given at the beginning of that chapter.

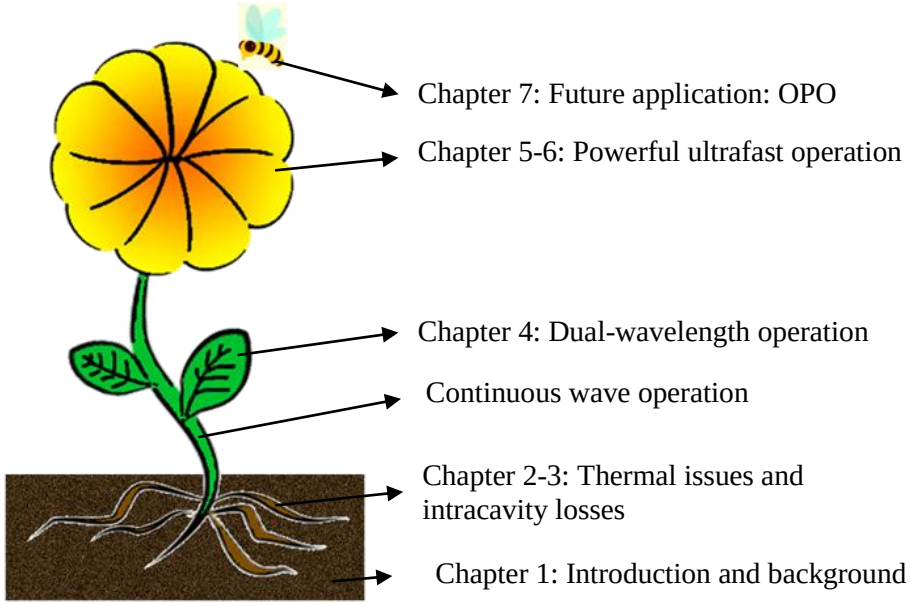

Fig. 1.7. Organization of the thesis.

In Chapter 2, we proposed a new pumping technique to alleviate the thermal issues for the end-pumped Yb:KGW bulk laser oscillator, which are a fundamental factor in power scaling of lasers. This chapter is based on the following publication:

H. Zhao and A. Major, "A continuous wave Yb:KGW laser with polarization-independent pump absorption," Laser Physics **23**, 095001 (2013).

Chapter 3 presents a simple, dynamic and accurate technique to characterize the intracavity losses in broadband Yb-ion lasers, in which case the conventional analysis has serious limitations and cannot be used. It is based on the following publication:

H. Zhao and A. Major, "Dynamic characterization of intracavity losses in broadband quasi-three-level lasers," Optics Express **22**, 26651-26658 (2014).

During the development of the continuous wave Yb:KGW laser, a dual-wavelength operation was observed. The experimental results and a discussion of the mechanism are presented in Chapter 4.

The following two chapters report on the pulsed operation of the Yb:KGW laser oscillator. Chapter 5 describes the generation of 67 fs pulses at an average output power of 3 W, which is, to the best of our knowledge, the highest average output power

produced to date from the Yb-ion based bulk lasers with such a short pulse duration. By lowering the repetition rate of the pulse train, pulses with high energy and high peak power (~1 MW) were delivered. These experimental results will be presented in Chapter 6. Chapter 5 and Chapter 6 are based on the following publications:

H. Zhao and A. Major, "Powerful 67 fs Kerr-lens mode-locked prismless Yb:KGW oscillator," Optics Express **21**, 31846-31851 (2013).

H. Zhao and A. Major, "Megawatt peak power level sub-100 fs Yb:KGW oscillators," Optics Express Optics Express **22**, 30425-30431 (2014).

Chapter 7 gives a theoretical analysis that predicts the potential of the presented ultrafast oscillator in driving a subsequent optical parametric oscillator (OPO), which is an indispensable light source for the future biomedical imaging system that is being built in our laboratory. This chapter is based on the following publication:

H. Zhao, I. T. Lima Jr., and A. Major, "Near-infrared properties of periodically poled $KTiOPO_4$ and stoichiometric MgO-doped $LiTaO_3$ crystals for high power optical parametric oscillation with femtosecond pulses," Laser Physics **20**, 1404-1409 (2010).

The work presented in this thesis will be concluded in Chapter 8.

References

[1] T. H. Maiman, "Stimulated Optical Radiation in Ruby," Nature **187**, 493-494 (1960).

[2] J. S. Baskin, and A. H. Zewail, "Freezing atoms in motion: principles of femtochemistry and demonstration by laser stroboscopy," J. Chem. Ed. **78**, 737-751 (2001).

[3] A. M. Larson, "Multiphoton microscopy," Nat. Photonics 5, (2011), doi:10.1038/nphoton.an.2010.2.

[4] A. F. Pegoraro, A. Ridsdale, D. J. Moffatt, Y. Jia, J. P. Pezacki, and A. Stolow, "Optimally chirped multimodal CARS microscopy based on a single Ti:sapphire oscillator," Opt. Express **17**, 2984-2996 (2009).

[5] H. K. Soong, and J. B. Malta. "Femtosecond lasers in ophthalmology," Am. J. Ophthalmol. **147**, 189-197 (2009).

[6] A. Vogel, J. Noack, G. Hüttman, and G. Paltauf. "Mechanisms of femtosecond laser nanosurgery of cells and tissues," Appl. Phys. B **81**, 1015-1047 (2005).

[7] T. Udem, R. Holzwarth, and T. W. Hänsch, "Optical frequency metrology," Nature **416**, 233-237 (2002).

[8] S. A. Diddams, L. Hollberg, and V. Mbele, "Molecular fingerprinting with the resolved modes of a femtosecond laser frequency comb," Nature **445**, 627-630 (2007).

[9] T. Steinmetz, T. Wilken, C. Araujo-Hauck, R. Holzwarth, T. W. Hänsch, L. Pasquini, A. Manescau, S. D'Odorico, M. T. Murphy, T. Kentischer, W. Schmidt, and T. Udem, "Laser Frequency Combs for Astronomical Observations," Science **321**, 1335–1337 (2008).

[10] M. Wojtkowski, V. J. Srinivasan, T. H. Ko, J. G. Fujimoto, A. Kowalczyk, and J. S. Duker, "Ultrahigh-resolution, high-speed, Fourier domain optical coherence tomography and methods for dispersion compensation," Opt. Express **12**, 2404-2422 (2004).

[11] S. V. Smirnov, J. D. Ania-Castanon, T. J. Ellingham, S. M. Kobtsev, S. Kukarin, and S. K. Turitsyn, "Optical spectral broadening and supercontinuum generation in telecom applications," Opt. Fiber Technol. **12**, 122-147 (2006).

[12] L. E. Hargrove, R. L. Fork, and M. A. Pollack, "Locking of He-Ne Laser Modes Induced by Synchronous Intracavity Modulation," Appl. Phys. Lett. **5**, 4-5 (1964).

[13] D. E. Spence, P. N. Kean, and W. Sibbett, "60-fsec pulse generation from a self-mode-locked Ti:sapphire laser," Opt. Lett. **16**, 42-44 (1991).

[14] U. Morgner, F. X. Kärtner, S. H. Cho, Y. Chen, H. A. Haus, J. G. Fujimoto, E. P. Ippen, V. Scheuer, G. Angelow, and T. Tschudi, "Sub-two-cycle pulses from a Kerr-lens mode-locked Ti:sapphire laser," Opt. Lett. **24**, 411-413 (1999).

[15] R. Ell, U. Morgner, F. X. KÃÂrtner, J. G. Fujimoto, E. P. Ippen, V. Scheuer, G. Angelow, T. Tschudi, M. J. Lederer, A. Boiko, and B. Luther-Davies, "Generation of 5-fs pulses and octave-spanning spectra directly from a Ti:sapphire laser," Opt. Lett. **26**, 373-375 (2001).

[16] K. Yamakawa, M. Aoyama, S. Matsuoka, T. Kase, Y. Akahane, and H. Takuma, "100-TW sub-20-fs Ti: sapphire laser system operating at a 10-Hz repetition rate," Opt. Lett. **23**, 1468-1470 (1998).

[17] X. Zhang, E. Schneider, G. Taft, H. Kapteyn, M. Murnane, and S. Backus, "Multi-microjoule, MHz repetition rate Ti:sapphire ultrafast regenerative amplifier system," Opt. Express **20**, 7015-7021 (2012).

[18] C. Hönninger, R. Paschotta, M. Graf, F. Morier-Genoud, G. Zhang, M. Moser, S. Biswal, J. Nees, A. Braun, G.A. Mourou, I. Johannsen, A. Giesen, W. Seeber, and U. Keller, "Ultrafast ytterbium-doped bulk lasers and laser amplifiers," Appl. Phys. B **69**, 3-17 (1999).

[19] N. V. Kuleshov, A. A. Lagatsky, A. V. Podlipensky, V. P. Mikhailov, and G. Huber, "Pulsed laser operation of Yb-doped $KY(WO_4)_2$ and $KGd(WO_4)_2$", Opt. Lett. **22**, 1317 (1997).

[20] A. Schmidt, S. Rivier, V. Petrov, U. Griebner, G. Ebert, A. Gross, V. Wesemann, S. Vernay, and D. Rytz, "65 fs diode-pumped diffusion-bonded Yb:KY(WO4)2/ KY(WO4)2 laser," Electron. Lett. 46, 641-643 (2010).

[21] G. Paunescu, J. Hein, and R. Sauerbrey, "100-fs diode-pumped Yb:KGW mode-locked laser," Appl. Phys. B 79, 555-558 (2004).

[22] G. R. Holtom, "Mode-locked Yb: KGW laser longitudinally pumped by polarization-coupled diode bars," Opt. Lett. 31, 2719-2721 (2006).

[23] F. Brunner, T. Südmeyer, E. Innerhofer, F. Morier-Genoud, R. Paschotta, V. E. Kisel, V. G. Shcherbitsky, N. V. Kuleshov, J. Gao, K. Contag, A. Giesen, and U. Keller, "240-fs pulses with 22-W average power from a mode-locked thin-disk $Yb:KY(WO_4)_2$ laser," Opt. Lett. **27**, 1162-1164 (2002).

[24] G. Palmer, M. Schultze, M. Siegel, M. Emons, U. Bünting, and U. Morgner, "Passively mode-locked $Yb:KLu(WO_4)_2$ thin-disk oscillator operated in the positive and negative dispersion regime," Opt. Lett. **33**, 1608-1610 (2008).

[25] C. R. E. Baer, Ch. Kränkel, C. J. Saraceno, O. H. Heckl, M. Golling, R. Peters, K. Petermann, Th. Südmeyer, G. Huber, and U. Keller, "Femtosecond thin-disk laser with 141 W of average power," Opt. Lett. **35**, 2302–2304 (2010).

[26] A. Schmidt, V. Petrov, U. Griebner, R. Peters, K. Petermann, G. Huber, C. Fiebig, K. Paschke, and G. Erbert, "Diode-pumped mode-locked $Yb:LuScO_3$ single crystal laser with 74 fs pulse duration," Opt. Lett. **35**, 511-513 (2010).

[27] C. J. Saraceno, O. H. Heckl, C. R. E. Baer, M. Golling, T. Südmeyer, K. Beil, C. Kränkel, K. Petermann, G. Huber, and U. Keller, "SESAMs for high-power femtosecond modelocking: power scaling of an $Yb:LuScO_3$ thin disk laser to 23 W and 235 fs," Opt. Express **19**, 20288-20300 (2011).

[28] M. Tokurakawa, A. Shirakawa, K. Ueda, H. Yagi, M. Noriyuki, T. Yanagitani and A. A. Kaminskii, "Diode-pumped ultrashort-pulse generation based on $Yb^{3+}:Sc_2O_3$ and $Yb^{3+}:Y_2O_3$ ceramic multi-gain-media oscillator," Opt. Express **17**, 3353-3361 (2009).

[29] A. A. Lagatsky, A. R. Sarmani, C. T. A. Brown, W. Sibbett, V. E. Kisel, A. G. Selivanov, I. A. Denisov, A. E. Troshin, K. V. Yumashev, N. V. Kuleshov, V. N. Matrosov, T. A. Matrosova, and M. I. Kupchenko, "Yb^{3+}-doped YVO_4 crystal for efficient Kerr-lens mode locking in solid-state lasers," Opt. Lett. **30**, 3234-3236 (2005).

[30] S. Rivier, X. Mateos, J. Liu, V. Petrov, U. Griebner, M. Zorn, M. Weyers, H. Zhang, J. Wang, and M. Jiang, "Passively mode-locked Yb:$LuVO_4$ oscillator," Opt. Express **14**, 11668-11671 (2006).

[31] F. Druon, F. Balembois, and P. Georges, "Ultra-short-pulsed and highly-efficient diode-pumped Yb:SYS mode-locked oscillators," Opt. Express **12**, 5005-5012 (2004).

[32] W. Li, Q. Hao, L. Ding, G. Zhao, L. Zheng, J. Xu, and H. Zeng, "Continuous-Wave and Passively Mode-Locked Yb:GYSO Lasers Pumped by Diode Lasers," IEEE J. Quantum Electron. **44**, 567-572 (2008).

[33] F. Druon, S. Chénais, P. Raybaut, F. Balembois, P. Georges, R. Gaumé, G. Aka, B. Viana, S. Mohr, and D. Kopf, "Diode-pumped Yb:$Sr_3Y(BO_3)_3$ femtosecond laser," Opt. Lett. **27**, 197-199 (2002).

[34] S. Rivier, A. Schmidt, C. Kränkel, R. Peters, K. Petermann, G. Huber, M. Zorn, M. Weyers, A. Klehr, G. Erbert, V. Petrov, U. Griebner, "Ultrashort pulse Yb:$LaSc_3(BO_3)_4$ mode-locked oscillator," Opt. Express **15**, 15539-15544 (2007).

[35] A. Yoshida, A. Schmidt, V. Petrov, C. Fiebig, G. Erbert, J. Liu, H. Zhang, J. Wang, and U. Griebner, "Diode-pumped mode-locked Yb:YCOB laser generating 35 fs pulses," Opt. Lett. **36**, 4425-4427 (2011).

[36] Y. Xue, C. Wang, Q. Liu, Y. Li, L. Chai, C. Yan, G. Zhao, L. Su, X. Xu, and J. Xu, "Characterization of Diode-Pumped Laser Operation of a Novel Yb:GSO Crystal," IEEE J. Quantum Electron. **42**, 517-521 (2006).

[37] Y. Zaouter, J. Didierjean, F. Balembois, G. Lucas Leclin, F. Druon, P. Georges, J. Petit, P. Goldner, and B. Viana, "47-fs diode-pumped Yb^{3+}:$CaGdAlO_4$ laser," Opt. Lett. **31**, 119-121 (2006).

[38] A. Agnesi, A. Greborio, F. Pirzio, G. Reali, J. Aus der Au, and A. Guandalini, "40-fs Yb^{3+}:$CaGdAlO_4$ laser pumped by a single-mode 350-mW laser diode," Opt. Express. **20**, 10077-10082 (2012).

[39] P. Sévillano, P. Georges, F. Druon, D. Descamps, and E. Cormier, "32-fs Kerr-lens mode-locked Yb:$CaGdAlO_4$ oscillator optically pumped by a bright fiber laser" Opt. Lett. **39**, 6001-6004 (2014).

[40] A. Greborio, A. Guandalini, and J. Aus der Au, "Sub-100 fs pulses with 12.5 W from Yb:CALGO based oscillators," Solid State Lasers XXI: Technology and Devices, in SPIE Photonics West 2012, paper 8235-11.

[41] S. Ricaud, A. Jaffres, K. Wentsch, A. Suganuma, B. Viana, P. Loiseau, B. Weichelt, M. Abdou-Ahmed, A. Voss, T. Graf, D. Rytz, C. Hönninger, E. Mottay, P. Georges, and F. Druon, "Femtosecond Yb:$CaGdAlO_4$ thin-disk oscillator," Opt. Lett. **37**, 3984-3986 (2012).

[42] A. Diebold, F. Emaury, C. Schriber, M. Golling, C. J. Saraceno, T. Südmeyer, and U. Keller, "SESAM mode-locked Yb:$CaGdAlO_4$ thin disk laser with 62 fs pulse generation," Opt. Lett. **38**, 3842-3845 (2013).

[43] F. Druon, F. Balembois, and P. Georges, "New laser crystals for the generation of ultrashort pulses," C. R. Physique **8**, 153-164 (2007).

[44] C. J. Saraceno, F. Emaury, O. H. Heckl, C. R. E. Baer, M. Hoffmann, C. Schriber, M. Golling, T. Südmeyer, and U. Keller, "275 W average output power from a femtosecond thin disk oscillator operated in a vacuum environment," Optics Express **20**, 23535-23541 (2012).

[45] A. Brenier, and G. Boulon, "Overview of the best Yb^{3+}-doped laser crystals," J. Alloys Compd. **323-324**, 210-213 (2001).

[46] V. Petrov, M. C. Pujol, X. Mateos, Ó. Silvestre, S. Rivier, M. Aguiló, R. M. Solé, J. Liu, U. Griebner, and F. Díaz, "Growth and properties of $KLu(WO_4)_2$, and novel ytterbium and thulium lasers based on this monoclinic crystalline host," Laser & Photon. Rev. **1**, 179–212 (2007).

[47] L. Zheng, J. Xu, G. Zhao, L. Su, F. Wu, and X. Liang, "Bulk crystal growth and efficient diode-pumped laser performance of Yb^{3+}:Sc_2SiO_5," Appl. Phys. B **91**, 443-445 (2008).

[48] H. Yu, X. Liang, J. He, Y. Leng, R. Li, Z. Xu, L. Zheng, G. Zhao, L. Su, and J. Xu, "Comparison of laser performances of 5at.% Yb:$Gd_{2x}Y_{2(1-x)}SiO_5$ crystals between different cutting directions," Chin. Phys. Lett. **25**, 2496-2499 (2008).

[49] P. Klopp, V. Petrov, U. Griebner, K. Petermann, V. Peters, and G. Erbert, "Highly efficient mode-locked Yb:Sc_2O_3 laser," Opt. Lett. **29**, 391-393 (2004).

[50] U. Griebner, V. Petrov, K. Petermann, and V. Peters, "Passively mode-locked Yb:Lu_2O_3 laser," Opt. Express **12**, 3125-3130 (2004).

[51] C. R. E. Baer, C. Kränkel, O. H. Heckl, M. Golling, T. Südmeyer, R. Peters, K. Petermann, G. Huber, and U. Keller, "227-fs pulses from a mode-locked Yb:$LuScO_3$ thin disk laser," Opt. Express **17**, 10725-10730 (2009).

[52] T. Südmeyer, C. Kränkel , C. R. E. Baer, O. H. Heckl, C. J. Saraceno, M. Golling, R. Peters, K. Petermann, G. Huber, U. Keller, "High-power ultrafast thin disk laser oscillators and their potential for sub-100-femtosecond pulse generation," Appl. Phys. B **97**, 281-295 (2009).

[53] P.-H. Haumesser, R. Gaumé, B. Viana, and D. Vivien, "Determination of laser parameters of ytterbiumdoped oxide crystalline materials," J. Opt. Soc. Am. B **19**, 2365-2375 (2002).

[54] S. Chénais, F. Balembois, F. Druon, G. Lucas-Leclin, and P. Georges, "Thermal Lensing in Diode-Pumped Ytterbium Lasers—Part I: Theoretical Analysis and Wavefront Measurements," IEEE J. Quantum Electron. **40**, 1217–1234 (2004).

[55] V. E. Kisel, N. A. Tolstik, A. E. Troshin, N. V. Kuleshov, V. N. Matrosov, T. A. Matrosova, M. I. Kupchenko, F. Brunner, R. Paschotta, F. Morier-Genoud, and U. Keller, "Spectroscopy and femtosecond laser performance of Yb^{3+}:$Gd_{0.64}Y_{0.36}VO_4$ crystal," Appl. Phys. B **85**, 581–584 (2006).

[56] F. Druon, S. Ricaud, D. N. Papadopoulos, A. Pellegrina, P. Camy, J. L. Doualan, R. Moncorgé, A. Courjaud, E. Mottay, and P. Georges, "On Yb:CaF_2 and Yb:SrF_2: review of spectroscopic and thermal properties and their impact on femtosecond and high power laser performance," Opt. Mater. Express **1**, 489-502 (2011).

[57] N. Coluccelli, G. Galzerano, L. Bonelli, A. Toncelli, A. Di Lieto, M. Tonelli, and P. Laporta, "Roomtemperature diode-pumped Yb^{3+}-doped $LiYF_4$ and KYF_4 lasers," Appl. Phys. B **92**, 519–523 (2008).

[58] G. Machinet, P. Sevillano, F. Guichard, R. Dubrasquet, P. Camy, J.-L. Doualan, R. Moncorgé, P. Georges, F. Druon, D. Descamps, and E. Cormier, "High-brightness fiber laser-pumped 68 fs–2.3 W Kerr-lens mode-locked Yb:CaF_2 oscillator," Opt. Lett. **38**, 4008-4010 (2013).

[59] O. Pronin, J. Brons, C. Grasse, V. Pervak, G. Boehm, M.-C. Amann, V. L. Kalashnikov, A. Apolonski, and F. Krausz, "High-power 200 fs Kerr-lens mode-locked Yb:YAG thin-disk oscillator," Opt. Lett. **36**, 4746-4748 (2011).

[60] S. Uemura, and K. Torizuka, "Kerr-lens mode-locked diode-pumped Yb: YAG laser with the transverse mode passively stabilized," Appl. Phys. Express **1**, 012007 1-3 (2008).

[61] C. Hönninger, F. Morier-Genoud, M. Moser, U. Keller, L. R. Brovelli, and C. Harder, "Efficient and tunable diode-pumped femtosecond Yb:glass lasers," Opt. Lett. **23**, 126-128 (1998).

[62] W. Li, Q. Hao, H. Zhai, H. Zeng, W. Lu, G. Zhao, L. Zheng, L. Su, and J. Xu, "Diode-pumped Yb:GSO femtosecond laser," Opt. Express **15**, 2354-2359 (2007).

[63] F. Thibault, D. Pelenc, F. Druon, Y. Zaouter, M. Jacquemet, and P. Georges, "Efficient diode-pumped Yb^{3+}:Y_2SiO_5 and Yb^{3+}:Lu_2SiO_5 high-power femtosecond laser operation," Opt. Lett. **31**, 1555-1557 (2006).

[64] B. Zhou, Z. Wei, Y. Zhang, X. Zhong, H. Teng, L. Zheng, L. Su, and J. Xu, "Generation of 210 fs laser pulses at 1093 nm by a self-starting mode-locked Yb:GYSO laser," Opt. Lett. **34**, 31-33 (2009).

[65] C. J. Saraceno, S. Pekarek, O. H. Heckl, C. R. E. Baer, C. Schriber, M. Golling, K. Beil, C. Kränkel, G. Huber, U. Keller, and T. Südmeyer, "Self-referenceable frequency comb from an ultrafast thin disk laser," Opt. Express **20**, 9650-9656 (2012).

[66] M. Tokurakawa, A. Shirakawa, K. Ueda, R. Peters, S. T. Fredrich-Thornton, K. Petermann, and G. Huber, "Ultrashort pulse generation from diode pumped mode-locked Yb^{3+}:sesquioxide single crystal lasers," Opt. Express **19**, 2904-2909 (2011).

[67] A. Yoshida, A. Schmidt, H. Zhang, J. Wang, J. Liu, C. Fiebig, K. Paschke, G. Erbert, V. Petrov, and U. Griebner, "42-fs diode-pumped Yb:$Ca_4YO(BO_3)_3$ oscillator," Opt. Express **18**, 24325-24330 (2010).

[68] F. Druon, F. Balembois, P. Georges, A. Brun, A. Courjaud, C. Hönninger, F. Salin, A. Aron, F. Mougel, G. Aka, and D. Vivien, "Generation of 90-fs pulses from a mode-locked diode-pumped Yb^{3+}:$Ca_4GdO(BO_3)_3$ laser," Opt. Lett. **25**, 423-425 (2000).

[69] Katrin Sarah Wentsch, Lihe Zheng, Jun Xu, Marwan Abdou Ahmed, and Thomas Graf, "Passively mode-locked Yb^{3+}:$ScSiO_5$ thin-disk laser," Opt. Lett. 4750-4752 (2012).

[70] A. Major, J. S. Aitchison, P. W. E. Smith, F. Druon, P. Georges, B. Viana, and G. P. Aka, "Z-scan measurements of the nonlinear refractive indices of novel Yb-doped laser crystal hosts," Appl. Phys. B **80**, 199-201 (2005).

[71] A. Major, J. S. Aitchison, P.W.E. Smith, N. Langford, and A.I. Ferguson, "Coherent two-photon absorption spectroscopy of the Raman-active $KGd(WO_4)_2$ crystal," Opt. Lett. **29**, 2896-2898 (2004).

Chapter 2
Polarization-independent pumping for reduction of thermal lensing

As was mentioned in the introduction, one of the main advantages of the Yb-doped solid state lasers is their capability to be pumped by the bright, compact and inexpensive laser diodes at a wavelength around 980 nm. For high-power pumping, fiber-coupled laser diode modules are widely used in the modern laser community. Such pumping sources provide a simple and flexible method of beam delivery to the gain medium and offer a round-shaped and homogeneous beam profile. The pump radiation can be easily imaged into the gain medium through a simple focusing system such as a pair of spherical lenses. On the other hand, the fiber-coupled laser diode modules usually offer unpolarized pump because of the depolarization of light in the fiber. Due to the anisotropic absorption behaviour of Yb:KGW crystals, the unpolarized pumping would consequently cause non-uniform absorption profiles along the length of the crystal. Moreover, the absorption profiles are strongly dependent on the current polarization state of the pump beam. Consequently, the non-uniform and polarization-sensitive absorption would cause considerable thermal lensing effect, which is detrimental to the efficiency, beam quality and overall stability of a laser. In this chapter, we propose a new pumping scheme to deal with the thermal issues of the Yb:KGW crystals, making them more suitable for pumping by high power unpolarized radiation from the fiber-coupled laser diode modules.

2.1 Thermal lensing

In the lasing process, the Yb:KGW crystal absorbs the pump radiation at a wavelength of 981 nm and emits laser radiation at around 1040 nm. Obviously, there is an energy difference between the pump photons and the laser photons. The excess energy will be

released as a waste heat deposited in the crystal. This photon energy difference is usually described as quantum defect that can be estimated by the following equation:

$$q = (1 - \lambda_p / \lambda_L) \times 100\%, \tag{2-1}$$

where λ_p is the pump wavelength and λ_L is the laser wavelength. For the Yb:KGW, approximately 6% of the pump power will be converted into the heat during the lasing process. The accumulation of the heat load in the gain crystal may give rise to a large and inhomogeneous stress which finally could cause a fracture of the crystal. Usually a cooling system is necessary to remove the heat load from the crystal (Appendix A). The cooling on the crystal's surface will then result in a temperature distribution across the active area that is perpendicular to the beam's propagation direction. The temperature gradient mainly induces two effects in the crystal: thermo-optic effect and thermo-mechanical effect. The influence of these effects is visualized in Fig. 2.1. The thermo-optic effect plays its role through altering the refractive index of the crystal, while the thermo-mechanical effect generates mechanical stress inside the crystal through the thermal expansion. Under the action of a temperature gradient, the hot center of the crystal is in compression while the cooled surface is bulged in tension. In addition, these stresses could further modify the refractive index of the crystal through the photoelastic effect. As a consequence, the temperature-induced gradient of refractive indices combined with the bulging deformation of the crystal's surface result in a distortion of the optical beam path from the center to the boundary surface. In an ideal case, this distortion is parabolic and can be described by a thin lens, i.e. the so-called thermal lens. As a laser beam passes through the gain crystal with induced thermal lens, its beam size and wavefront can be both distorted. A positive thermal lens will focus the laser beam while a negative thermal lens will defocus the beam.

For an end-pumped gain medium (see Fig. 2.4), the spatial matching between the laser beam and the pump beam inside the gain medium is of critical importance with regard to the lasing efficiency. The thermal lensing induced size variation of the laser beam can break the well-designed matching, leading to a reduction of the output power and lasing efficiency. Especially in the case where the laser beam is expanded and becomes larger than the pump beam, the reabsorption losses (Chapter 3.1) in the unpumped region can

remarkably degrade the lasing performance or even stop the lasing process completely. Distortion of the beam wavefront induced by thermal lensing is a detrimental factor to the beam quality, which characterizes the imperfection of a laser beam in comparison to the perfect fundamental beam (TEM_{00} mode). In an ideal case, these distortions can be compensated easily by adjusting the distances between the cavity components. Unfortunately, in most cases, the thermal lens suffers from aberrations, resulting in a complicated wavefront distortion that is difficult to correct. Especially in many anisotropic Yb-doped crystals, such as the Yb:KGW used in this work, the strength of thermal lensing can be different for different directions, resulting in a beam astigmatism that is hard to correct. Therefore, an effective management of the thermal lensing effect in the gain medium is quite important in order to achieve high output power, high lasing efficiency as well as good beam quality.

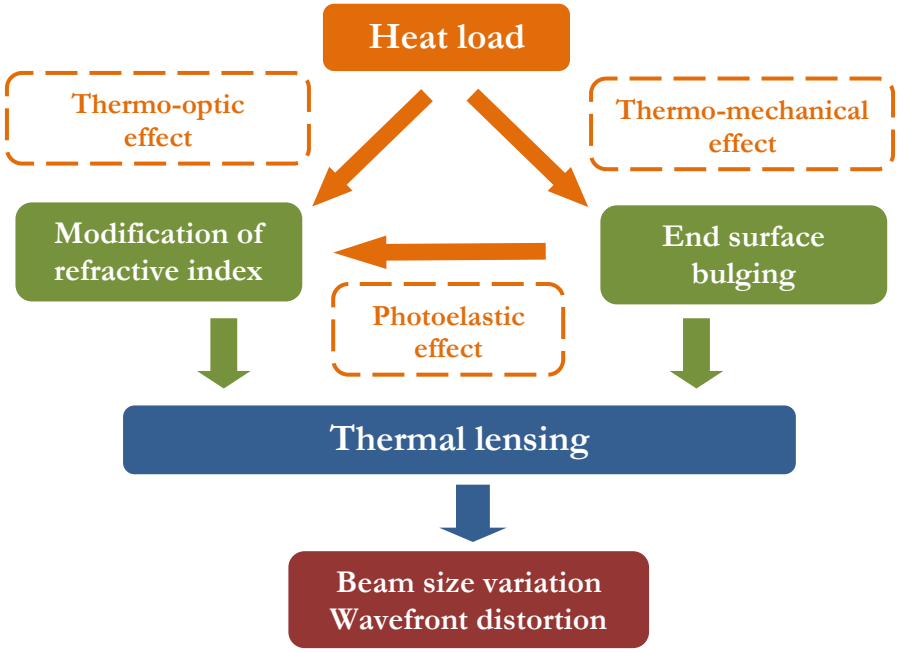

Fig. 2.1. Schematic diagram of thermal lens formation and its effects on laser beams.

2.2 Thermal lensing reduction for unpolarized pumping

In section 2.1, we discussed formation of the thermal lensing without considering the heat distribution along the beam propagation direction in the crystal. In fact, the pump absorption and hence the heat load follow an exponential decay, rather than a uniform

pattern, over the beam propagation path. This increases the strength of thermal lensing and the risk of crystal fracture since a large part of the heat load is distributed within the front part of the crystal. Under unpolarized pumping, the situation can become even worse. This will be theoretically addressed in this section by simulating the absorption profile along the propagation direction in a standard Yb:KGW crystal pumped by an unpolarized radiation. Then we will propose a new pumping scheme which is more suitable for use with the unpolarized pumping. Before presenting the theoretical calculation, we will start from a brief introduction of the absorption anisotropy of Yb:KGW crystals, which is the main reason behind the discussed problem.

2.2.1 Anisotropic absorption properties of Yb:KGW crystals

The crystals of Yb:KGW are biaxial birefringent crystals, which have three orthogonal refractive index axes labeled as N_m, N_p and N_g with $n_g > n_m > n_p$ (n is the refractive index). The commercially available crystals are usually cut along one of these refractive axes. For example, an N_g-cut crystal allows the light to propagate along the N_g-direction, while the N_m-direction and N_p-direction can be used as the polarizations for absorption and emission. Fig. 2.2 gives the absorption spectra of the Yb:KGW crystals. These spectra exhibit a strong dependence on the axis of the crystal. Among the three refractive axes, the N_m-axis exhibits the highest absorption cross section at the wavelength of 981 nm (~6 times higher than those of the N_p-axis and N_g-axis), making it the most favorable polarization for efficient pumping. The accessibility to the N_m-axis requires the use of the N_g-cut or N_p-cut Yb:KGW crystals, which have served as standard crystals in most of the reported literature [1-5].

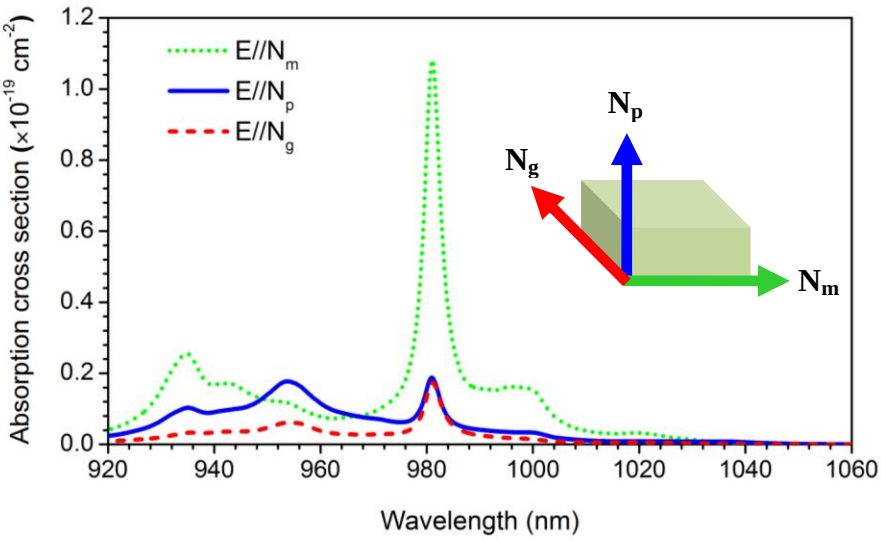

Fig. 2.2. The absorption cross sections of Yb:KGW crystals along N_m, N_p and N_g polarizations. The inset represents the coordinate system of the refractive axes.

2.2.2 Polarization-dependent absorption

As the Yb:KGW crystals are usually pumped by an unpolarized radiation, the pump power will be absorbed on the two refractive axes that are perpendicular to the propagation direction. Assuming that the power is divided equally between the two polarizations which are parallel to the two absorption axes of the crystal, the absorbed pump power can be expressed as:

$$P_{abs} = P_0\{1-\frac{1}{2}[\exp(-\alpha_i x)+\exp(-\alpha_j x)]\}\ , \tag{2-2}$$

where P_0 is the pump power, α_i and α_j are the absorption coefficients for the two absorption axes. The absorption coefficient at a certain wavelength can be derived from the absorption cross section by multiplying it by the Yb-ion concentration (which equals to 2.2×10^{20} cm^{-3} for 5 at.% Yb:KGW crystal used in this work). The first derivative of the P_{abs} with respect to the distance x indicates the power absorbed at a certain position in the crystal and can be expressed as:

$$P_{abs}{}' = \frac{dP_{abs}}{dx} = \frac{1}{2}P_0[\alpha_i \exp(-\alpha_i x)+\alpha_j \exp(-\alpha_j x)]\,. \tag{2-3}$$

The normalized P_{abs}' of an N_g-cut Yb:KGW crystal pumped by an unpolarized radiation at wavelength of 980 nm was calculated. The result is shown as the blue line in Fig. 2.3. The area below the line represents the percentage of the pump power being absorbed by the crystal. In a 7-mm-long N_g-cut crystal, approximately 94% of the pump power can be absorbed. The absorption profile, however, exhibits an apparent non-uniform feature: a large portion (about 75%) of the power is absorbed within the first 2 mm, while the remaining small portion is absorbed over a much longer length. The heat, therefore, will be released in a small volume at the front of the crystal and finally will cause strong thermal lensing effect. A very similar absorption profile can also be obtained for the N_p-cut Yb:KGW crystals.

In the simulation, the pump power was assumed to spread equally over the two polarizations. However, in real case, this assumption can be easily perturbed by the mechanical disturbance, such as moving, coiling and twisting applied to the fiber. The variation of the polarization state of the pump radiation can modify the absorption profile, therefore resulting in variable thermal lensing and unstable lasing performance.

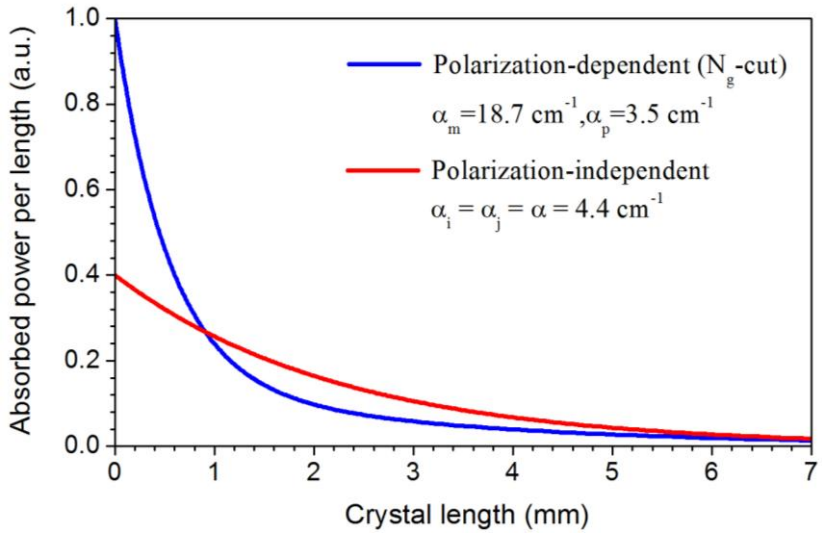

Fig. 2.3. Theoretical calculations of the absorbed pump power at different positions along the length of a crystal for polarization-dependent (N_g-cut) and polarization-independent crystal orientations.

2.2.3 Polarization-independent absorption

The non-uniform absorption profile presented in the standard Yb:KGW crystal originates from the large difference between the absorption coefficients that depend on the polarization of pump radiation. If, in an ideal situation, the two polarizations involved in the absorption have the same absorption coefficients, i.e. $\alpha_i = \alpha_j = \alpha$, the equation (2-3) can be simplified to a polarization-independent form:

$$P_{abs}{}' = \frac{dP_{abs}}{dx} = P_0 \alpha \exp(-\alpha x) . \tag{2-4}$$

In this case, a pure exponential decay of the absorption over the length of the crystal can be obtained (the red line in Fig. 2.3). In the simulation, the absorption coefficient for the two polarizations was selected such that to ensure that 94% of the pump power was absorbed by the 7-mm-long crystal as in the case before.

In comparison to the polarization-dependent absorption, this polarization-independent absorption has a much more uniform profile along the length of the crystal. Consequently, the heat can be released over a longer distance. As a result, a significant reduction of the thermal lensing effect can be expected. Moreover, the absorbed power and the heat load at the entrance surface of the crystal were reduced by more than 50%, therefore resulting in a lower risk of crystal fracture.

2.3 Experimental realization

2.3.1 Experimental design

Realization of the polarization-independent absorption requires identical absorption coefficients for the two involved polarizations. As can be seen from Fig. 2.2, this condition can be achieved by pumping a standard N_g-cut crystal at a wavelength of 967 nm or 949 nm, where the two absorption axes N_m and N_p have exactly the same absorption coefficients. Nevertheless, the shorter pump wavelength (compared to 980 nm) will introduce more heat and stronger thermal lensing, which contradicts with our initial purpose. In addition, the absorption coefficients at 967 nm are too low to achieve an efficient absorption.

In this work, we employ an Yb:KGW crystal cut for beam propagation along the N_m-axis (N_m-cut); therefore the N_p-axis and N_g-axis can serve for absorbing the pump power. At a pump wavelength of 980 nm, the absorption coefficients of these two axes are very similar to each other (as shown in Fig. 2.2). Despite the small difference between the absorption coefficients, this pumping scheme still can exhibit the feature of the polarization-independent absorption.

The proof of principle of the proposed pumping scheme was demonstrated with the N_m-cut, 2 mm × 8 mm × 1.2 mm (2 mm along the N_m-axis and 1.2 mm along the N_p-axis) Yb:KGW crystal slab (Castech) with 5 at.% doping concentration (Fig. 2.4, inset). The fiber-coupled laser diode module provided an unpolarized pumping beam with a maximum of 18 W of output power at a drive current of 23 A (Apollo Instruments Inc). The pumping beam was delivered through the two antireflection (AR) coated achromatic doublets, forming a beam spot with 250 μm diameter in the crystal. The crystal was wrapped in indium foil and held between two copper blocks, which were kept at a constant temperature of 20 ℃. The heat was efficiently removed in the direction parallel to the N_p-axis [2, 6].

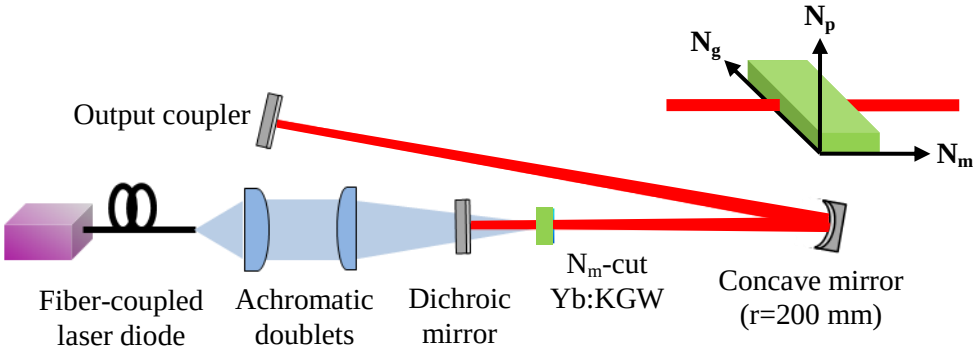

Fig. 2.4. The layout of the CW N_m-cut Yb:KGW oscillator pumped by a fiber-coupled laser diode. The inset indicates the orientation of the N_m-cut crystal with respect to the laser propagation direction.

The laser cavity, as shown in Fig. 2.4, consisted of a plane dichroic mirror, a concave mirror and a plane output coupler with 5% transmittance at the lasing wavelength. The dichroic mirror was coated for high transmission (>95%) at the pump wavelength and high reflection (>99.9%) in the 1020-1080 nm region (Laseroptik GmbH). The concave

mirror was coated for high reflection at the lasing wavelength. The distances between the cavity optics were optimized to provide a fundamental mode size of 245 μm in diameter inside the crystal, which was well matched with the pumping mode.

2.3.2 Theoretical simulations

Considering the pump power lost due to the optical components such as the achromatic doubles and dichroic mirror, the maximum pump power delivered to the crystal was measured to be 17.3 W. The absorbed power measured under non-lasing conditions was 7.8 W. The power absorption profile along the length of the crystal under these experimental conditions was modeled theoretically by using equation (2-3). At the pump wavelength of 980 nm, the absorption coefficients are α_p = 3.2 cm^{-1} and α_g = 2.7 cm^{-1}. The red line in Fig. 2.5 represents the absorption profile inside the 2-mm-long N_m-cut crystal. The area below the curve corresponds to the total absorbed power of 7.7 W, which is very close to the experimentally measured value of 7.8 W. A comparison was made with the conventional N_g-cut crystal with the same amount of power absorbed, shown as the blue line in Fig. 2.5. The graph indicates that the absorption profile along the length of the crystal is much more uniform in the N_m-cut crystal, which would further contribute to the reduction of thermal lensing. Moreover, the power absorbed at the entrance facet of the crystal was reduced by more than 50%, leading to a greatly reduced risk of crystal fracture.

Finite element analysis (FEA) for evaluation of the thermal effect was carried out with LASCAD software (LAS-CAD GmbH). The 3-D temperature distributions in the top halves of the crystal slabs with the N_m-cut and N_g-cut geometries are presented in Fig. 2.6, with the insets showing the 2-D temperature distributions of the central slides along the length of the crystals. In agreement with the absorption profile, the temperature distribution is much more uniform along the length of the N_m-cut crystal. The temperature at the center of the entrance facet of the N_m-cut crystal is 20 ℃ lower than that of the N_g-cut crystal. This difference will be more pronounced as longer crystals with higher pump power absorption percentages are used.

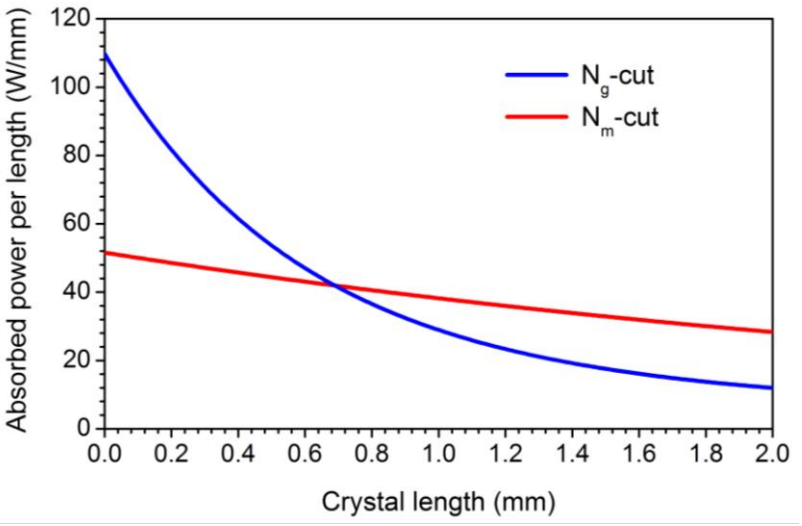

Fig. 2.5. Simulations of the absorbed pump power at different positions along the length of a crystal with the N_m-cut and N_g-cut geometries. The areas below the curves represent a total absorbed pump power of 7.7 W by the 2-mm-long crystal, which is close to the experimentally measured value of 7.8 W.

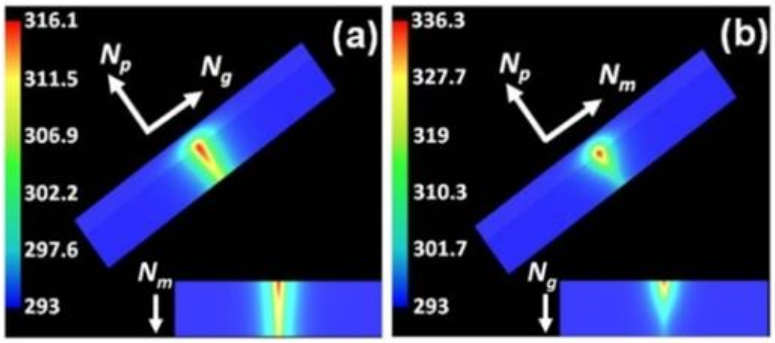

Fig. 2.6. 3-D temperature distributions in the top halves of the 2-mm-long crystals with the N_m-cut (a) and N_g-cut (b) geometries. Insets: 2-D temperature distributions along the beam propagation directions.

The focal length of the thermal lens can be estimated if the relevant thermo-optical parameters of the crystals are well known. For Yb:KGW, the thermal expansion coefficients along the different axes have been determined with good agreement by several groups [6-9]. However, another important parameter, thermo-optic coefficient *dn/dT*, has a great discrepancy not only in the value but also in the sign among the reported data [8-10]. Therefore, it is difficult to estimate the strength of the thermal lensing without a reliable *dn/dT*. In the following section, we present the strength of the

thermal lensing measured in the experiment. A detailed discussion of the *dn/dT* will be given based on the experimental results.

2.3.3 Experimental results and discussion

The lasing performance of the CW N_m-cut Yb:KGW crystal is presented in Fig. 2.7, showing the output power as a function of the input power. At a maximum incident pump power of 17.3 W the laser delivered 2 W of radiation at 1040 nm, corresponding to an optical-to-optical efficiency of 25.6% with respect to the absorbed pump power. This result is comparable with those obtained from conventional or athermal-cut crystals for the same amount of absorbed pump power [3, 11]. It is worth noting that the same output power was achieved using 1.5 times longer athermal-cut crystal [3]. The laser power measurements showed obvious nonlinearity, which is mainly caused by the redshift of the pump wavelength with increasing diode's drive current. At maximum output power, the slope efficiency is 47% with respect to the incident pump power. The measured beam quality (M^2) value at maximum output power is less than 1.2. The output was polarized along the N_p-axis, which has the broadest emission spectrum and the highest gain around 1040 nm among the three polarizations. Therefore the proposed crystal geometry will also be beneficial to the development of ultrashort pulse Yb:KGW lasers.

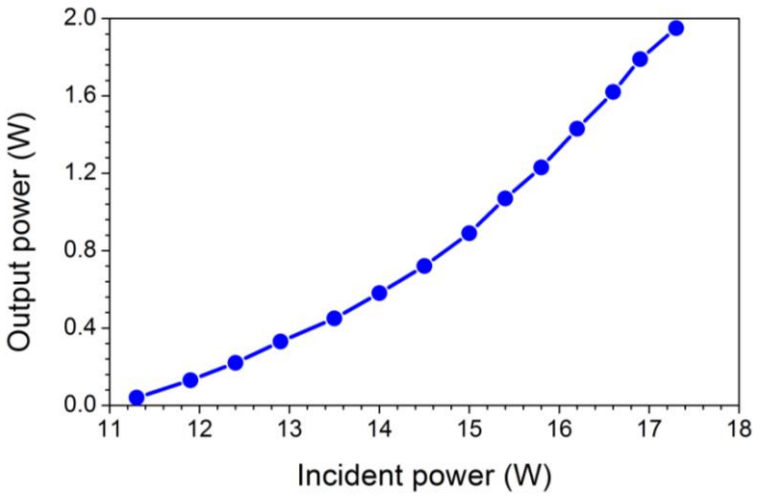

Fig. 2.7. Output power versus incident pump power for the CW N_m-cut Yb:KGW laser.

The strength of the thermal lensing was estimated by measuring the dependence of the laser beam size on the distance away from the output coupler. The measured dependence for the N_g-direction (parallel to the width of the crystal) at different absorbed pump powers is shown in Fig. 2.8. It is obvious that the laser beam in this direction was stretched as the absorbed pump power was increased. The laser beam size in the N_p-direction is not shown here, since it remained almost unchanged as the absorbed power was increased (see the right side of Fig. 2.8).

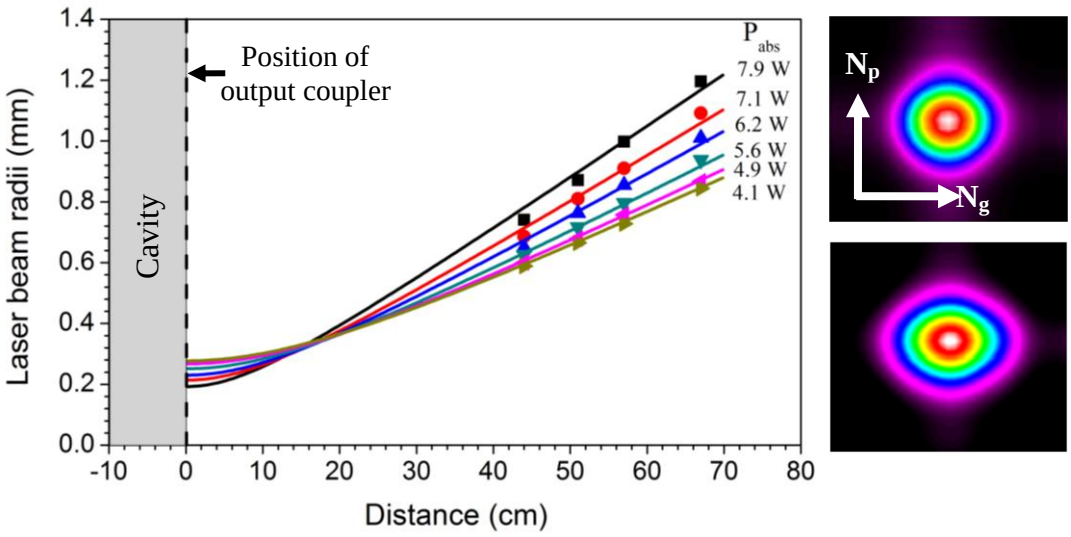

Fig. 2.8. Left: the laser beam radii as a function of the distance from the output coupler at different absorbed pump power levels for the N_g-direction of the N_m-cut Yb:KGW crystal. Right: the far-field profiles of the output beam at 5.6 W (top) and 7.8 W (bottom) of absorbed pump power. (The symbols are the experimental data, and the solid curves are theoretical fits using ABCD matrix analysis).

By using the ABCD matrix analysis, the strength of the thermal lens can be estimated. The ABCD matrix analysis is a ray tracing technique that can be used to trace the laser beam propagating inside and outside of the oscillator. Knowing the ray transfer matrix for each optical component (Appendix B) and the distances between the components, the beam size at any position can be determined. Since the beam sizes outside of the oscillator have been experimentally obtained, the fitting of the data allows us to retrieve the focal length of the induced thermal lens, which can be treated as a thin lens placed in the central plane of the gain medium.

The dots in Fig. 2.9 indicate the estimated strength of the thermal lensing at different absorbed pump power levels. The strength is indicated by the dioptric power, which is defined as the inverse of the focal length. It is clear that the thermal lens in the N_g-direction is negative, which was never reported before in literature. In this case, the negative thermo-optical coefficient *dn/dT* plays a dominant role in the formation of the thermal lens, and to some extent this is balanced by the positive effect of thermal expansion. This is in sharp contrast to the previously reported positive values of thermal lenses in [11-12] where the positive effect of thermal expansion took a dominant place over the negative thermo-optical effect (e.g. in the N_p-cut crystals), or both the thermal expansion effect and the thermo-optical effect had positive values (e.g. in the N_g-cut crystals). Although the sign of the thermal lens is negative in our case, the absolute value of the induced thermal lens is almost twice as low as that of the conventional crystal geometries and is comparable to that of the athermal-cut crystals for the same amount of absorbed pump power [3]. On the other hand, for the N_p-direction, the negative *dn/dT* has a smaller absolute value, which can be balanced by the thermal expansion to a large extent, therefore leading to a neglectable thermal lensing. The solid line in Fig. 2.9 shows the theoretical thermal lensing for the N_g-direction simulated by the LASCAD program. In the simulation, the value of *dn/dT* used was -8.7×10^{-6} K^{-1}, which is consistent with recently reported results [8-9]. The discrepancy between the experimental results and simulation is believed to mainly come from the nonlinearity of the pump power absorption induced by the wavelength shift of the pump radiation as the level of power was changed. It is worth noting that thermal lensing in combination with the Kerr effect can play a significant role in pulse shaping in the mode-locked regime [2, 13].

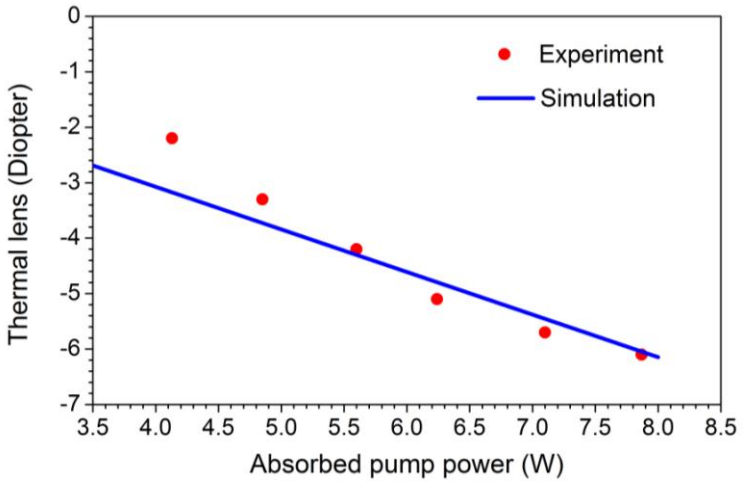

Fig. 2.9. The dioptric power of the induced thermal lens as a function of the absorbed pump power. (Dots: experimental results, line: results of simulations using LASCAD software.)

2.4 Conclusion

In summary, a new excitation technique with polarization-independent pump absorption based on the N_m-cut Yb:KGW crystal was proposed. This technique has potential for laser power scaling due to the reduced effects of thermal loading and lensing, as well as reduced output power instability caused by mechanical disturbances of the pump fiber. Initial tests were performed with a 2-mm-long Yb:KGW crystal slab. The demonstrated CW laser produced 2 W of average output power in a TEM_{00} mode at 1040 nm. Numerical and experimental results confirmed the significant reduction of thermal lensing. These successful results provide a route for the development of multi-Watt Yb:KGW lasers in both CW and ultrashort pulse regimes with improved beam quality and enhanced power stability against mechanical perturbations of the pump module.

References

[1] G. Paunescu, J. Hein, and R. Sauerbrey, "100-fs diode-pumped Yb:KGW mode-locked laser," Appl. Phys. B **79**, 555-558 (2004).

[2] G. R. Holtom, "Mode-locked Yb: KGW laser longitudinally pumped by polarization-coupled diode bars," Opt. Lett. **31**, 2719-2721 (2006).

[3] J. E. Hellström, S. Bjurshagen, V. Pasiskevicius, J. Liu, V. Petrov, and U. Griebner, "Efficient Yb:KGW lasers end-pumped by high-power diode bars," Appl. Phys. B **83**, 235-239 (2006).

[4] A. Major, R. Cisek, and V. Barzda, "Femtosecond Yb:$KGd(WO_4)_2$ laser oscillator pumped by a high power fiber-coupled diode laser module," Opt. Express **14**, 12163-12168 (2006).

[5] A. Major, D. Sandkuijl, and V. Barzda, "Femtosecond Yb: $KGd(WO_4)_2$ laser with > 100 nJ of pulse energy," Laser Phys. Lett. **6**, 779-781 (2009).

[6] I. V. Mochalov, "Laser and nonlinear properties of the potassium gadolinium tungstate laser crystal $KGd(WO_4)_2$: Nd^{3+}-(KGW:Nd)," Opt. Eng. **36**, 1660-1669 (1997).

[7] M. C. Pujol, R. Sole, J. Massons, Jna. Gavalda, X. Solans, C. Zaldo, F. Diaz, and M. Aguilo, "Structural study of monoclinic $KGd(WO_4)_2$ and effects of lanthanide substitution," J. Appl. Crystallogr. **34**, 1-6 (2001).

[8] P. A. Loiko, K. V. Yumashev, N. V. Kuleshov, G. E. Rachkovskaya, and A. A. Pavlyuk, "Thermo-optic dispersion formulas for monoclinic double tungstates $KRe(WO_4)_2$ where *Re* = Gd, Y, Lu, Yb," Opt. Mater. **33**, 1688-1694 (2011).

[9] S. Biswal, S. P. O'Connor, and S. R. Bowman, "Thermo-optical parameters measured in ytterbium-doped potassium gadolinium tungstate," Appl. Opt. **44**, 3093-3097 (2005).

[10] A. A. Lagatsky, A. Abdolvand, and N. V. Kuleshov, "Passive Q switching and self-frequency Raman conversion in a diode-pumped Yb:$KGd(WO_4)_2$ laser," Opt. Lett. **25**, 616-618 (2000).

[11] J. E. Hellstrom, V. Pasiskevicius, F. Laurell, B. Denker, B. Galagan, L. Ivleva, S. Sverchkov, I. Voronina, and V. Horvath, "Laser performance of Yb:$GdCa_4O(BO_3)_3$ compared to Yb:$KGd(WO_4)_2$ under diode-bar pumping," Laser Phys. **17**, 1204-1208 (2007).

[12] D. Stucinskas, R. Antipenkov, and A. Varanavicius, "Thermal lensing in high-power diode-pumped Yb: KGW laser," Lith. J. Phys. **50**, 191-199 (2010).

[13] A. Major, J. S. Aitchison, P. W. E. Smith, F. Druon, P. Georges, B. Viana, G. P. Aka, "Z-scan measurements of the nonlinear refractive indices of novel Yb-doped laser crystal hosts," Appl. Phys. B **80**, 199-201 (2005).

Chapter 3
Dynamic characterization of intracavity losses in broadband quasi-three-level lasers

Intrinsic losses introduced by various laser cavity components (or intracavity losses) play a fundamental role in limiting efficiency of laser performance. Currently, however, their accurate characterization is only available for the four-level laser systems [1] and only at the threshold of operation. At the same time, over the past decade quasi-three-level laser systems based on Yb-ion doped materials have become technologically important. Ytterbium ion solid-state [2] and fiber [3] lasers are revolutionizing industrial and scientific applications such as micromachining [4] and multiphoton microscopy [5]. Despite this fact, determination of parasitic intracavity losses in such laser systems remained a technological and scientific challenge. Here we demonstrate a simple, fast and accurate analysis of intracavity losses of quasi-three-level lasers based on spectral gain measurement. The technique overcomes limitations of the four-level laser model [1], enabling dynamic characterization of loss, and hence, providing a potential for real-time optimization of laser performance at any working point above the threshold.

3.1 Loss sources of a laser oscillator

In the lasing process, the steady-state operation can be reached when the losses distributed inside of an oscillator are balanced by the gain. While the gain is generated only in the lasing medium, the losses may come from a variety of sources.

3.1.1 The transmission of output coupler

The output coupler is a coated dielectric mirror that allows the lasing power to be partially extracted from the oscillator. It provides a useful loss in the lasing performance. An output coupler with low transmission leads to a low lasing threshold, while an output coupler with high transmission can extract more power from the oscillator. For the Yb-

ion solid-state laser oscillators, the optimized output coupling transmission at lasing wavelength is in the range of 1% - 15%, depending on the host materials and the cavity configurations. As an example, the reflectivity (which equals to 1-*T*, where *T* is transmittance) curve of an output coupler provided by Layertec GmbH is shown in Fig. 3.1 (a). In the wavelength range between 990 nm and 1080 nm, the output coupler has a flat reflection of 85% with ±1% variation.

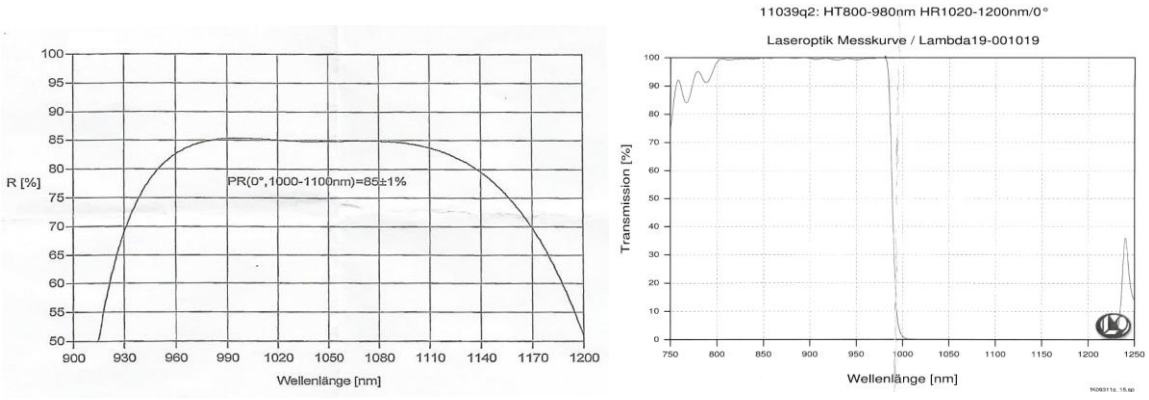

Fig. 3.1. (a) Reflection of an output coupler with 85±1% reflectivity between 990 nm and 1080 nm. (b) Transmission spectrum of a dichroic mirror with high transmission at 980 nm and high reflection in the range of 1020-1200 nm.

3.1.2 The intracavity losses

The intracavity losses are a parasitic and unavoidable factor that would degrade the lasing efficiency of a laser oscillator. Especially in some cases where an output coupler with low transmission is used (e.g. thin-disk oscillators), the output power is highly sensitive to the intracavity losses. More than a few percent of the intracavity losses may completely cease the lasing process. The intracavity losses may come from almost any component inside the cavity, and they may experience a variation as the lasing condition is changed.

(a) Losses of cavity mirrors

Although the cavity mirrors are coated to be highly reflective at lasing wavelength, the imperfection of the coating leads to a leakage of intracavity power. Especially, due to the small difference of the pump and laser wavelengths of Yb-ion lasers, dichroic coating with a very sharp separation of the transmission and reflection bands is required (Fig. 3.1

(b)). An imperfect coating may introduce more leakage through the dichroic mirrors. In addition, the dust and minor scratches on the mirrors can cause scattering and hence additional losses of the laser light.

(b) Reabsorption losses

The reabsorption losses are a drawback suffered by most of the Yb-doped gain media, which have a quasi-three-level energy structure as shown in Fig.3.2 (a). Due to the small Stark splitting of the ground energy manifold, a small portion of the electrons can be thermally excited to the terminal state (E_1) of the lasing transition, giving rise to reabsorption of the lasing photons. This transition is in sharp contrast to the behaviour in a four-level system (e.g. Nd-ion lasers), where the energy gap between the ground state (E_0) and the terminal state (E_1) is quite large such that thermal excitation of electrons and the reabsorption can be avoided (Fig. 3.2 (b)).

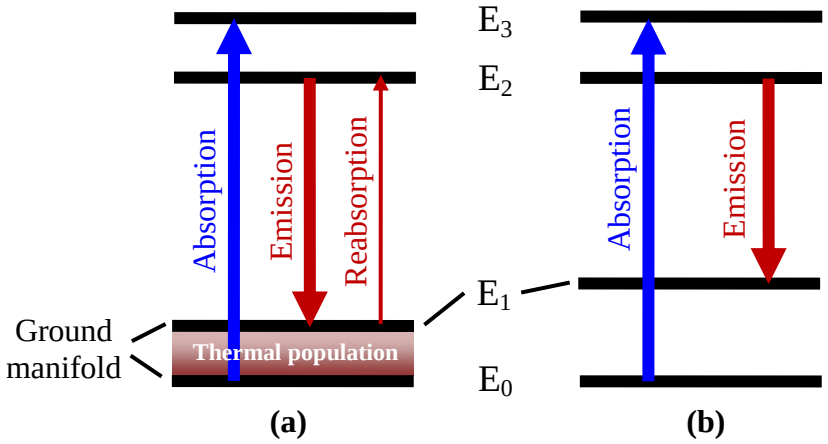

Fig. 3.2. Energy level schemes and main transitions present in the (a) quasi-three-level and (b) four-level systems.

The reabsorption losses are critically important for the quasi-three-level gain media when they are pumped longitudinally from the end surface(s). High lasing efficiency of an end-pumped oscillator requires a good spatial matching between the pump beam and laser beam inside the gain medium. With a good overlap, the reabsorption can be compensated for by pumping more power into the gain medium. However, in some cases, where a bad oscillator design or thermal lensing effect causes a laser beam to become larger than the pump beam in the gain medium, the reabsorption losses in the unpumped

regions cannot be compensated. Such reabsorption losses will contribute to the intracavity losses (Fig. 3.3).

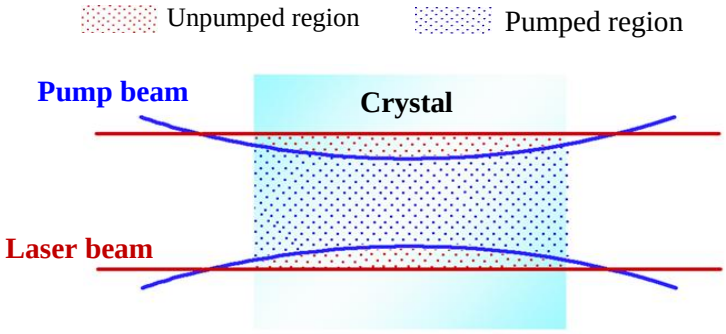

Fig. 3.3. A side view of a crystal with a pump beam and a laser beam passing through it, indicating the pumped and unpumped regions.

(c) Non-saturable losses of SESAM

Semiconductor saturable absorber mirror (SESAM) is a passive optical component that is widely used for ultrashort pulse formation (details will be given in section 5.1). Ideally, high peak power of a pulse can saturate the SESAM, allowing a 100% reflection of the incident power. However, due to the defects in the SESAM, some losses (typically 0.5-2%) can be introduced resulting from a nonsaturable absorption.

(d) Losses of laser crystals

According to the Fresnel's equations, as the laser radiation passes through an uncoated surface of the crystal, about 10% of its power will be reflected and lost. Hence, the entrance facets of the crystals are usually antireflection (AR) coated. However, like the high reflection (HR) coatings on the mirrors, the imperfection of the AR coatings will lead to a small amount of reflection and loss. This source of loss should be carefully considered because the laser beam usually has four passes through the crystal's surface in each round-trip. In addition, the damage of the AR coating at high power levels will significantly reduce the lasing efficiency or even cease the lasing process.

Besides this main source of loss, several minor losses, such as the scattering and unwanted absorption induced by impurities and defects in the crystals can also contribute to the intracavity losses.

Despite the importance of characterizing the intracavity losses in evaluating the performance of a laser oscillator, a simple arithmetic estimation of them is almost impossible because of their diversity, uncertainty and variability. An experimentally effective and accurate characterization of the intracavity losses, therefore, is highly desired in practical usage.

3.2 Traditional methods

In this section, I will briefly review the widely used methods for characterization of the intracavity losses. The limitations of these methods with the broadband quasi-three-level laser oscillators will be addressed.

3.2.1 Findlay-Clay analysis

As early as 1966, Findlay and Clay have developed the well-known method for characterizing the intracavity losses by using the relationship between the threshold pump power and the transmission of the output couplers [1]:

$$P_{th} = K(2g_l l_c) = K(L_{in} - \ln(R_{oc})). \tag{3-1}$$

In equation (3-1), P_{th} is the pump power at lasing threshold, g_l is the peak gain at lasing wavelength, l_c is the crystal length, L_{in} is the round-trip intracavity loss, R_{oc} is the reflectivity of the output coupler, and K is a constant that is related to the parameters of the pump beam, laser beam and the gain medium. In order to extract the intracavity loss, repetitive measurements with different output couplers have to be performed. The validity of this model is based on the assumption that the peak gain g_l for a particular laser transition is spectrally independent from loss L_{in}, which results in a linear plot between the logarithm of the output coupler reflectivity and the threshold pump power. The extrapolation of the linear plot to zero P_{th} indicates the intracavity losses.

While perfectly valid for a typical 4-level laser system (e.g. 1064 nm transition of Nd:YAG crystal), the assumption used in Findlay-Clay analysis is no longer valid in case of a quasi-three-level laser transition which also exhibits reabsorption loss. Unfortunately, in case of broadband quasi-three-level transitions such as those of the Yb-ions in solid matrices, the situation becomes even much more complicated because the gain and reabsorption losses are wavelength dependent. This leads to a nonlinear relationship between the threshold pump power and the introduced loss and to erroneous analysis.

Another serious limitation of the traditional Findlay-Clay analysis is that it determines the intracavity losses only at the *threshold* of laser operation. Knowledge of the intracavity losses *during* the laser operation would be particularly valuable for the quasi-three-level lasers where thermal lens induced mismatch between the pump and laser mode volumes at high pump power levels can introduce reabsorption losses in the unpumped regions of the laser mode. Such additional losses would effectively contribute to the total intracavity loss. Therefore, the ability of dynamic intracavity loss characterization can be used to ensure that a laser always operates in optimized configuration.

3.2.2 Modeling for quasi-three-level lasers

Laser performance of the end-pumped oscillator with quasi-three-level transition has been modeled by Taira *el al*. In this model, reabsorption losses were taken into account. The threshold pump power was calculated with the following equation [6] which resembles the one used in Findlay-Clay analysis:

$$P_{th} = \frac{\pi h\upsilon_p (w_p^2 + w_L^2)}{4\tau_f [\sigma_{em}(\lambda_L) + \sigma_{abs}(\lambda_L)](f_u + f_l)} (T_{OC} + L_{in} + \delta_{reabs}), \qquad (3\text{-}2)$$

where $h\upsilon_p$ is the pump photon energy, w_l and w_p are the waist size of the laser beam and pump beam, λ_p is the pump wavelength, f_u and f_l are the fractional populations in the lower and upper energy states (E_2 in Fig. 3.2), $\sigma_{abs}(\lambda_L)$ and $\sigma_{em}(\lambda_L)$ are the absorption and emission cross sections at the lasing wavelength, τ_f is the lifetime of the upper energy state, T_{oc} is the transmission of the output coupler and δ_{reabs} is the wavelength-dependent reabsorption loss. If all these parameters are well known, the intracavity losses L_{in} can be

calculated. The difficulty in estimation of the L_{in} using this model comes from the uncertainty of many parameters presented in equation (3-2).

3.3 New method: spectroscopic gain analysis

The spectral dependency of the gain and loss in broadband quasi-three-level laser transitions, on one hand, is a drawback that limits the validity of the traditional methods to characterize them. On the other hand, it provides us with an opportunity to determine them from the lasing spectrum. It is well known that in a steady state operation the overall cavity loss is balanced by the gain:

$$R_{oc}(1-L_{in})\exp[g(\lambda_L)]=1, \tag{3-3}$$

where L_{in} is the round-trip intracavity loss already defined above, R_{oc} is the reflectivity of the output coupler also defined above, and $g(\lambda_L)$ is the wavelength-dependent effective gain coefficient which takes into account the reabsorption loss. It follows from (3-3) that if gain coefficient is known, then the intracavity losses can be found. Since the gain coefficient determines the oscillating wavelength of a laser, it can be easily calculated by measuring the lasing spectrum and using the following equation from [7]:

$$g(\lambda_L)=2N_0 l_c[\beta(\sigma_{em}(\lambda_L)+\sigma_{abs}(\lambda_L))-\sigma_{abs}(\lambda_L)], \tag{3-4}$$

where N_0 is the doping concentration and l_c is the crystal length. The factor of 2 accounts for the double pass of the laser radiation in the gain medium. The value of β, which is the fractional population inversion, controls the shape and the peak wavelength of the gain spectrum and therefore is defined by the experimentally measured lasing wavelength. The sources of original data on emission and absorption spectra of a particular gain medium can be usually found in the literature.

As can be seen, the presented technique eliminates repetitive measurements (only one output coupler is needed) thus providing a simple, fast and accurate characterization of the intracavity loss. Moreover, by taking into account dependence of the emission and absorption spectra on the temperature, the estimation of losses potentially can be done at any output power level; therefore the measurements provide the current value of the

intracavity loss and can be used for dynamic monitoring of the lasing performance. In addition to loss, the laser gain coefficient is also found.

3.4 Experimental characterization

The experiments were carried out with a diode-pumped continuous wave Yb:KGW oscillator with a standard delta cavity shown in Fig. 3.4 which could support two polarizations, the N_m and N_p. The cavity was designed to have a good overlap between the pump and cavity modes. The Yb:KGW crystal slab (Eksma) with 5 mm × 8 mm × 1.2 mm dimensions and 1.5 at.% doping was cut along the N_g-axis and AR coated. A BK7 plate was used at Brewster's angle to select oscillation with polarization either along the N_m-axis or N_p-axis [8]. The pump beam from a fiber coupled laser diode was delivered through the two AR coated achromatic doublets, forming a beam spot with 375 μm diameter in the crystal. The pump absorption in the crystal was measured to be 50% under non-lasing conditions. The cavity optics were configured to provide a cavity mode size of 320 μm in diameter inside the crystal. This relatively small beam size took into account the effect of thermal lensing and ensured that the cavity mode was always within the pumped region. The output power was measured by a calibrated thermopile power meter and the lasing spectrum was recorded by a spectrum analyzer (Anritsu MS2687B) with a wavelength resolution of 0.07 nm.

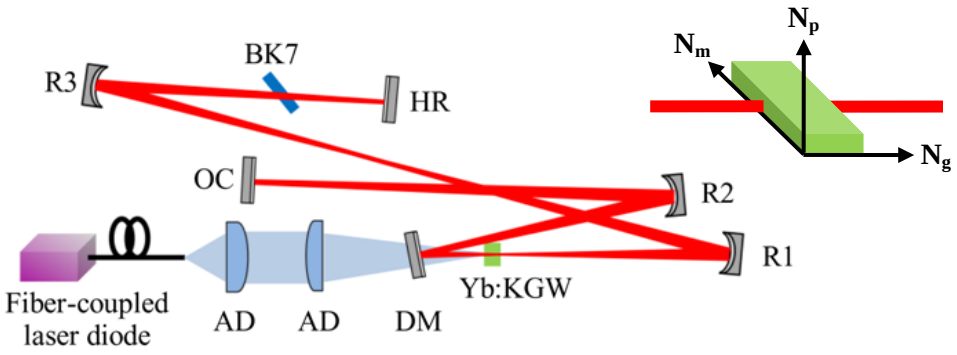

Fig. 3.4. Schematic of a continuous wave Yb:KGW laser. AD: achromatic doublet; DM, dichroic mirror; R1, R2, R3: concave mirrors with radii of curvatures of 600 mm, 600 mm and 750 mm; OC: output coupler; HR: highly reflective mirror. The inset indicates the orientation of the N_g-cut crystal with respect to the laser propagation direction.

3.4.1 Laser performance

The laser performance was evaluated with a series of output couplers with transmission ranging from 0.4% to 10%. The best performance for both polarizations (N_m and N_p) was achieved with a 5% output coupler as shown in Fig. 3.5. The output power was 3.3 W for the N_m-polarization and 3.5 W for the N_p-polarization at the pump power of 21 W (~10 W absorbed), corresponding to a slope efficiency of more than 70% with respect to the absorbed pump power. The output power plots exhibited a nonlinear behavior since the pump wavelength shifted to a longer one as the diode's drive current was increased as well as varying overlap between the cavity and pump modes as a result of thermal lensing.

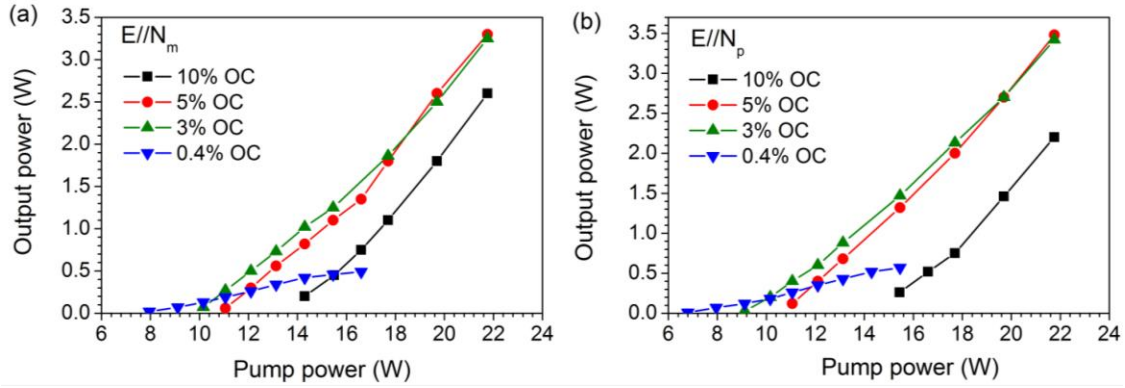

Fig. 3.5. The output power as a function of pump power for different output couplers for (a) the N_m-polarization and (b) the N_p-polarization.

3.4.2 Characterization of intracavity losses

The lasing spectra of the laser and the corresponding calculated gain spectra for the N_m-polarization and the N_p-polarization are shown in Fig. 3.6. For all output couplers the lasing spectra were recorded at the pump power of 17.5 W, and no shifts in wavelength for each output coupler were observed as the pump power was increased up to the maximum of 22 W. The lasing wavelength λ_L, the fitted population inversion β, the gain coefficient $g(\lambda_L)$ at the lasing wavelength, and the calculated intracavity losses L_{in} are listed in Table 3.1. The room-temperature data on emission and absorption spectra of the Yb:KGW crystal that were used in these calculations were published in [9] and kindly

provided to us by S. R. Bowman (Optical Sciences Division, U.S. Naval Research Laboratory).

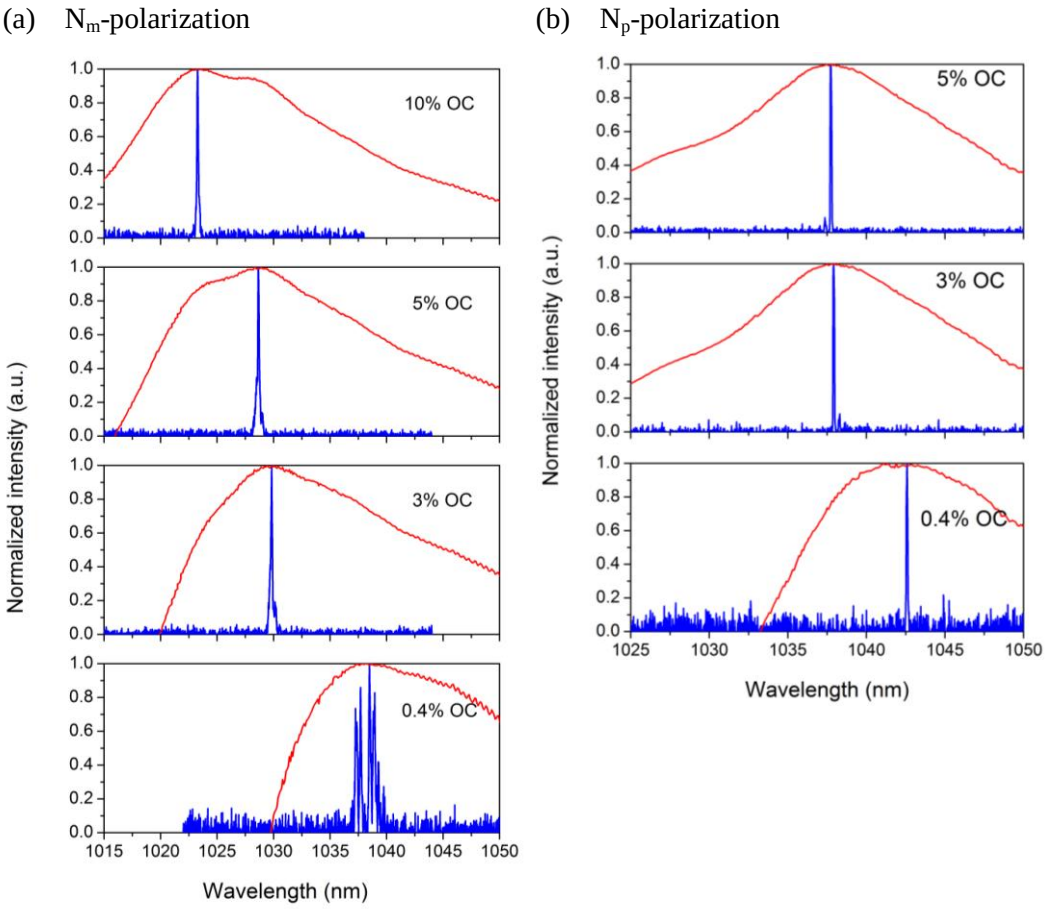

Fig. 3.6. The lasing spectra (blue lines) and the calculated gain spectra (red curves) for different output couplers: (a) for the N_m-polarization and (b) for the N_p-polarization. OC, output coupler. As the value of OC was changed, the lasing wavelength shifted to have the highest gain.

Table 3.1. Gain spectra parameters and estimated intracavity losses

T_{oc}		λ_L (nm)	β	$g(\lambda_L)$	L_{in}
10%	N_m	1023.3	0.164	0.128	0.020
	N_p	1037	-	-	-
5%	N_m	1028.7	0.13	0.073	0.021
	N_p	1037.7	0.143	0.087	0.033
3%	N_m	1029.8	0.115	0.053	0.022
	N_p	1037.9	0.113	0.058	0.026
0.4%	N_m	1038.5	0.073	0.013	0.009
	N_p	1042.6	0.062	0.013	0.009

The intracavity losses for the N_m- and N_p-polarizations have consistent values of ~2.1% and ~3.0% for the 3-10% and 3-5% output couplers, respectively. There is a number of factors that could have contributed to the uncertainty in these obtained values of intracavity loss. The difference in intracavity losses between both polarizations can be attributed to a slight misalignment of the Brewster plate during realignment procedure, which was used (in both cases) to select the N_m- or N_p-polarization. The difference in intracavity losses between the individual output couplers (for a particular polarization) could have also resulted from some residual misalignment that was left after their changing and from variation of the cavity mirror's reflectivity (including that of the output coupler) in the 1023-1043 nm wavelength range. More generally, systemic errors came from the wavelength resolution of the spectrum analyzer (0.07 nm) and of the available emission and absorption spectra (0.1 nm) of the Yb:KGW crystal. In addition, the measurement errors in the emission and absorption spectra and their dependence on the temperature and the actual level of doping concentration also can provide a degree of uncertainty. While all used highly reflective cavity optics were specified to be 99.9% reflective in the 1010-1100 nm range and had less than 0.01% change in reflectivity in the observed lasing wavelength range, we were unable to find any temperature dependent data on emission and absorption cross sections of Yb:KGW. For this reason the room-temperature data set from [9] was used in our calculations. The fact that for every output coupler no wavelength shift was observed as the pump power was increased points out that in our case the effect of temperature at least on the gain shape was negligible. It also should be noted that the level of error of the estimated intracavity loss induced by the inaccuracy of the emission and absorption data and the doping concentration depends on the gain level. A higher gain level can give rise to a larger error. For example, 1% inaccuracy of the data can produce 1% variation of the gain (according to the equation (3-4)), which consequently would result in ~6% error in the estimated intracavity loss if a 10% output coupler was used, whereas the error would be reduced to 2% if a 3% output coupler was used. We believe that a cumulative error in the estimated intracavity loss in our case did not exceed 1%. A simple estimation supports this statement: taking manufacturer's specified loss of 0.1% for highly reflecting, dichroic and crystal's AR coatings the total intracavity loss per roundtrip can be put at 1.3%. Considering the

scattering introduced by the dust particles on optics (the laser was not operated in a clean room and did not have a cover) the actual loss will be closer to the experimentally inferred values.

On the other hand, the data show a large error with 0.4% output coupler for both polarizations. This is caused by a relatively flat gain spectrum at low level of loss. This leads to a difficulty in assignment of the peak gain wavelength because of multiple wavelengths in the spectrum (N_m-polarization) or very vague peaks in the calculated gain spectrum (N_p-polarization). Another possible limitation could be due to spectroscopic data of the crystal since reabsorption at the longer wavelengths is fairly weak thus making its accurate measurement difficult. In addition, the lasing wavelength of the N_p-polarization (see Fig. 3.6 (b)) had a shorter tuning range and was clamped at 1037 nm as the cavity loss exceeded a certain level. Thus with the 10% output coupler, the population inversion and the corresponding gain spectrum could not be reliably determined. Therefore, the intracavity losses estimated by this spectroscopic method could have large errors when the output couplers induce too large or too small losses. In order to determine the range of applicable losses, the calculated lasing wavelength from equation (3-3) was plotted in Fig. 3.7 as a function of the total cavity loss (i.e. $R_{oc} + L_{in}$). At low level of loss the curves are relatively steep, corresponding to a spectrally flat gain spectrum and at high level of loss they become flat, resulting in an invariable lasing wavelength. It can be seen that the optimum ranges of total cavity losses that can be used for correct intracavity loss estimation are 2.5% - 19% for the N_m-polarization and 3.5% - 8.5% for the N_p-polarization.

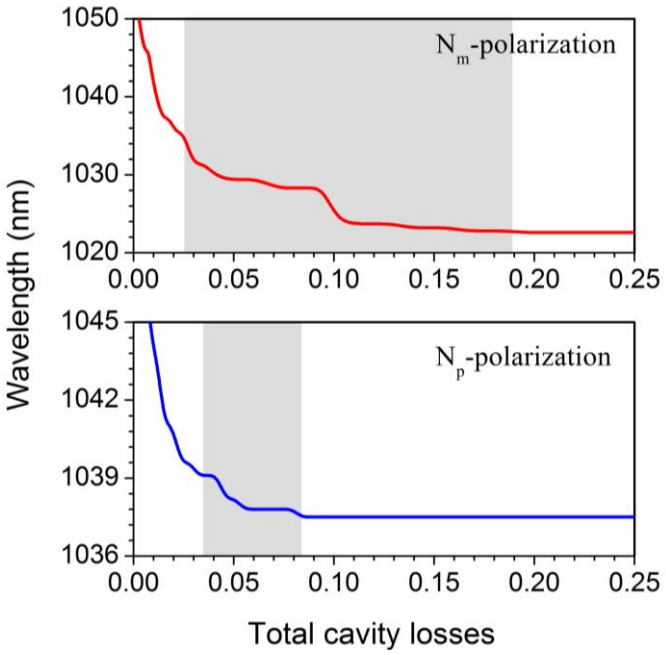

Fig. 3.7. The calculated lasing wavelength as a function of the total cavity loss. The shaded areas indicate the ranges of applicable losses which correspond to a single lasing wavelength and well defined peaks in the gain spectra.

3.4.3 Comparison with traditional methods

For comparison the Findlay-Clay analysis [1] was also performed and the data are displayed in Fig. 3.8. Considering the reabsorption losses in the quasi-three-level lasers, the equation (3-1) can be corrected as:

$$P_{th} = K(2g_l l_c) = K(L_{in} - \ln(R_{oc}) + \delta_{reabs}), \tag{3-5}$$

where K is a constant and $\delta_{reabs}=2N_0 l_c \sigma_{abs}(\lambda_L)$ is the round-trip reabsorption loss (in our case it is wavelength-dependent through $\sigma_{abs}(\lambda_L)$). For the analysis the threshold pump power could not be determined by linear fitting of the output power plots because of their obvious nonlinearity (shown in Fig. 3.5). Therefore, in this work, the threshold pump power was recorded when the lasing ceased while decreasing the pump diode's drive current. A noticeable deviation from linear behavior of the measured relationship between the P_{th} and $\ln(R_{oc})$ was observed for the N_m-polarization (see Fig. 3.8). For the N_p-polarization, owing to a narrower wavelength tuning range and almost constant level of the reabsorption loss, the relationship is closer to a linear. According to the Findlay-Clay analysis, the intercept of the linear data fit with the horizontal axis gives the overall

cavity loss (excluding the loss of the output coupler). By subtracting the reabsorption loss of about 5%, the estimated intracavity loss for the N_p-polarization is 1.8% and is close to our previous measurements. For the N_m-polarization, however, although the linear fit points to an overall cavity loss of about 10%, it is still impossible to estimate the intracavity loss because the reabsorption loss varied from 3% to 20% (see Table 3.2) for the observed oscillating wavelength range. This clearly shows the limitation of the Findlay-Clay analysis. It is worth noting that similar to the work of Findlay and Clay, Caird's analysis [10] also assumes that the lasing wavelength is spectrally independent from loss and, therefore, cannot be used for analysis of intracavity losses in broadband quasi-three-level gain media.

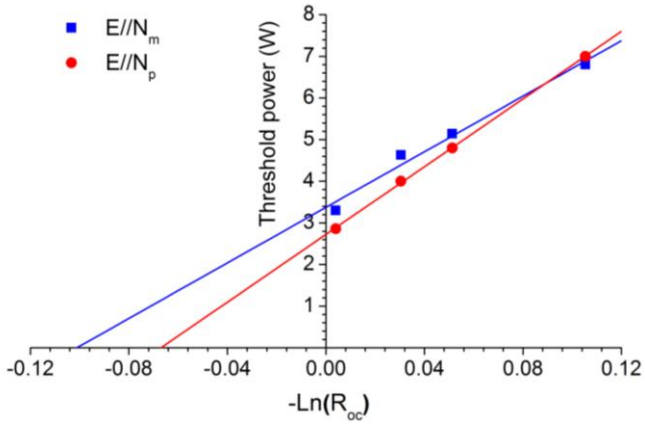

Fig. 3.8. Findlay-Clay plots for both polarizations, N_m and N_p. The intercept of the graph with the horizontal axis defines the intracavity loss.

For further comparison we also estimated the intracavity loss using the equation (3-2) derived from a numerical modeling of the quasi-three-level lasers [6]. The values of the parameters are as the follows: the pump photon energy $h\upsilon_p = 2 \times 10^{-19}$ J is the pump photon energy, the lifetime of the upper energy manifold $\tau_f = 300$ μs, $f_u = 0.75$ and $f_l = 0.04$ are determined based on the energy structure of the Yb:KGW crystal [11]. The cavity mode radius w_L of 165 μm was used when considering a weak thermal lens (~1 diopter) at the lasing threshold. Taking the pump beam quality (M^2) of 35 into consideration, an averaged pump mode radius $w_p = 205$ μm was used [12]. Other parameters, including the reabsorption loss δ_{reabs} and the emission and absorption cross sections ($\sigma_{em}(\lambda_L)$ and $\sigma_{abs}(\lambda_L)$), are all wavelength-dependent. Their values are listed in

Table 3.2. With the measured absorbed pump power (and its spectrum) at lasing threshold, the intracavity losses were calculated for each output coupler (see Table 3.2).

The data in Table 3.2 indicate that this numerical model also has large errors. This is caused by the uncertainties and approximations that were involved in the measurements and calculations. Firstly, the threshold pump power was determined in the same way as for the Findlay-Clay analysis, although the power meter itself has a finite accuracy. Secondly and most important, the effect of the overlap between the pump mode and the cavity mode had a large uncertainty since the effect of thermal lensing (even at threshold) would change the shape of the cavity mode. Most likely this is reflected in the growing intracavity losses as the output coupling was increased.

Table 3.2. Lasing parameters and intracavity losses calculated through the numerical modeling

T_{oc}		σ_{em_l} ($\times 10^{-20}$cm^2)	σ_{abs_l} ($\times 10^{-21}$cm^2)	δ_{reabs}	P_{th} (W)	L_{in}
10%	N_m	2.54	2.69	0.197	6.6	0.088
	N_p	1.37	0.79	0.058	6.7	0.048
5%	N_m	1.89	1.57	0.115	4.9	0.043
	N_p	1.36	0.74	0.054	4.66	0.035
3%	N_m	1.76	1.38	0.101	4.4	0.022
	N_p	1.35	0.73	0.053	3.75	0.027
0.4%	N_m	0.82	0.43	0.032	3.2	0.022
	N_p	0.96	0.42	0.031	2.73	0.022

As can be concluded from the above discussion, both conventional methods have serious limitations and result in large errors. More importantly, they estimate the intracavity loss only at the lasing threshold, a condition that is very different from the normal operating regime. The newly proposed method, however, was shown to be more accurate and consistent, and potentially allows one to estimate the intracavity losses at any output power levels. It can be further improved by taking into account temperature-dependent emission and absorption cross sections, spatially varying level of inversion in the crystal [13,14] as well as inhomogeneity of pumping. We anticipate that this method will be also applicable to other broadband gain media such as, for example, Yb:CaF_2, Yb:glass, and Yb:CALGO. While questionable, its application to narrowband materials

like Yb:YAG is not completely impossible and can be assessed by making calculations similar to the ones presented in Fig. 3.7 to identify a suitable range of losses.

To demonstrate dynamic application of our technique we adjusted the cavity to provide a lasing mode that would have a poor overlap with the pump mode at low pump power and a better overlap at high pump power as a result of thermal lensing. Fig. 3.9 shows the lasing spectra as the pump power was increased from the lasing threshold at 11.7 W to 24.7 W. It can be seen that the lasing wavelength shifted from 1029 nm to 1030.4 nm, corresponding to a reduction of intracavity loss from 4.6% to 2.3% as better overlap between the modes was achieved. While optimization of laser performance can be done by simply monitoring of its output power, our approach allows one to do the same in the spectral domain. It is worth noting that in many cases simple monitoring of the output power is not always objective enough criterion because the lasing efficiency may experience a loss-induced degradation despite the continuous growth of the output power (e.g. in case of thermal roll off).

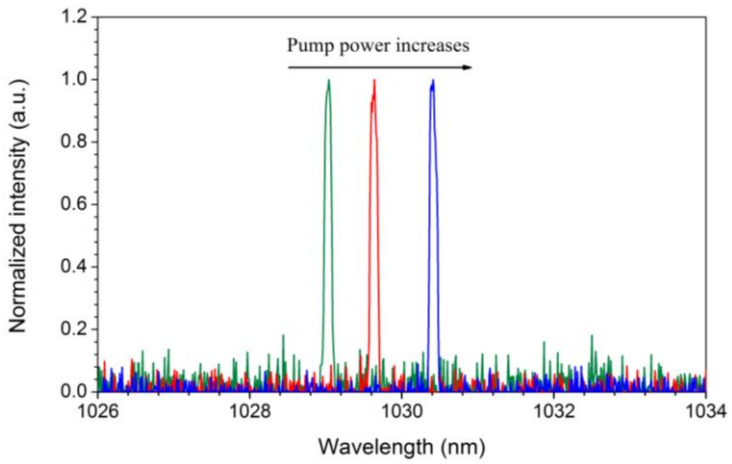

Fig. 3.9. Shift of the lasing wavelength with increase of the pump power. A 3% output coupler was used. As the pump power was increased, the lasing spectrum shifted from short wavelength (high intracavity loss) to long wavelength (low intracavity loss).

3.5 Conclusion

In conclusion, a technique to estimate the intracavity losses based on the spectroscopic gain analysis was presented. This technique can be applied to the laser oscillators based on the quasi-three-level energy structure with broad emission spectrum, where the traditional Findlay-Clay analysis is not applicable. It provides an accurate estimation of the intracavity loss based on a single measurement. More importantly, the estimation is not limited only to the lasing threshold, thus allowing one to adjust laser cavity parameters according to the dynamically varying intracavity loss. A comparison with the traditional Findlay-Clay analysis and numerical modeling method was made and limitations were discussed. An experimental test with a diode-pumped Yb:KGW laser oscillator was demonstrated. We believe that this technique will be equally important for the continuous wave as well as ultrafast lasers based on broadband quasi-three-level gain media.

References

[1] D. Findlay and R. A. Clay, "The measurement of internal losses in 4-level lasers," Phys. Lett. **20**, 277-278 (1966).

[2] T. Sudmeyer, S. V. Marchese, S. Hashimoto, C. R. E. Baer, G. Gingras, B. Witzel, and U. Keller, "Femtosecond laser oscillators for high-field science," Nature Photon. **2**, 599-604 (2008).

[3] C. Jauregui, J. Limpert, and A. Tunnermann, "High-power fibre lasers," Nature Photon. **7**, 861-867 (2013).

[4] R. R. Gattass and E. Mazur, "Femtosecond laser micromachining in transparent materials," Nature Photon. **2**, 219-225 (2008).

[5] C. Xu and F. W. Wise, "Recent advances in fibre lasers for nonlinear microscopy," Nature Photon. **7**, 875-882 (2013).

[6] T. Taira, W. M. Tulloch, and R. L. Byer, "Modeling of quasi-three-level lasers and operation of cw Yb:YAG lasers," Appl. Opt. **36**, 1867-1874 (1997).

[7] C. Hönninger, R. Paschotta, M. Graf, F. Morier-Genoud, G. Zhang, M. Moser, S. Biswal, J. Nees, A. Braun, G. A. Mourou, I. Johannsen, A. Giesen, W. Seeber, and U. Keller, "Ultrafast ytterbium-doped bulk lasers and laser amplifiers," Appl. Phys. B **69**, 3-17 (1999).

[8] A. Major, D. Sandkuijl, and V. Barzda, "A diode-pumped continuous-wave Yb:KGW laser with N_g-axis polarized output," Laser Phys. Lett. **6**, 779-781 (2009).

[9] S. R. Bowman, S. P. O'Connor, and S. Biswal, "Ytterbium laser with reduced thermal loading," IEEE J. Quantum Electron. **41**, 1510-1517 (2005).

[10] J. A. Caird, S. A. Payne, P. R. Staver, A. J. Ramponi, L. L. Chase, and W. F. Krupke, "Quantum electronic properties of the $Na_3Ga_2Li_3F_{12}:Cr^{3+}$ laser," IEEE J. Quantum Electron. **24**, 1077–1099 (1988).

[11] N. V. Kuleshov, A. A. Lagatsky, A. V. Podlipensky, V. P. Mikhailov, G. Huber, "Pulsed laser operation of Yb-doped $KY(WO_4)_2$ and $KGd(WO_4)_2$," Opt. Lett. **22**, 1317-1319 (1997).

[12] I. D. Lindsay and M. Ebrahimzadeh, "Efficient continuous-wave and Q-switched operation of a 946-nm Nd:YAG laser pumped by an injection-locked broad-area diode laser," Appl. Opt. **37**, 3961-3970 (1998).

[13] S. Yiou, F. Balembois, and P. George, "Numerical modelling of a continuous-wave Yb-doped bulk crystal laser emitting on a three-level laser transition near 980 nm," J. Opt. Soc. Am. B **22**, 572–581 (2005).

[14] B. Jacobsson, J. E. Hellström, V. Pasiskevicius, and F. Laurell, "Widely tunable Yb:KYW laser with a volume Bragg grating," Opt. Express **15**, 1003–1010 (2007).

Chapter 4

Simultaneous CW dual-wavelength operation

Many rare-earth-doped materials allow multiple longitudinal modes with different wavelengths to oscillate in a laser cavity. In normal continuous wave (CW) operation, however, only one of them with the highest gain can reach the lasing threshold and obtain amplification, resulting in a single-wavelength emission. Other longitudinal modes with weaker gain will be fully suppressed in the gain competition with the superior mode. If, in some special cases, the gain for two (or multiple) modes is equalized, both (or all) of them will oscillate in the cavity. As a consequence, a simultaneous dual-wavelength (multiple-wavelength) laser will be generated. The equalization of the gain is usually achieved by introducing a larger loss to the high-gain mode such that its net gain is comparable to that of the mode with a weaker gain. Over the recent years, the simultaneous dual-wavelength lasers have demonstrated their potential in many fields, such as precise metrology, remote sensing, frequency conversion and generation of terahertz (THz) radiation, etc [1-3]. In this Chapter, I present the generation of dual-wavelength radiation in a CW Yb:KGW laser oscillator.

4.1 Dual-wavelength operation in rare-earth-doped materials

Rare-earth-doped materials are naturally suited to be used for generation of simultaneous dual-wavelength radiation due to their diverse energy transitions between sublevels of different Stark manifolds. Among them, many Nd-doped gain media (e.g. Nd:YAG, Nd:$LuVO_4$, Nd:YVO_4, Nd:$La_2CaB_{10}O_{19}$) have been extensively investigated for this purpose [4-8]. The dual-wavelength radiation with either a wide spectral spacing (e.g. 1064 nm and 1342 nm) or a narrow spacing (e.g. 1086 nm and 1089 nm, 946 nm and 1064 nm) has been demonstrated. The gain equalization for the Nd-ion oscillators has been realized in many ways. A commonly used method is to employ two output couplers coated with different transmissions at the desired lasing wavelengths [5]. Besides, by

inserting an etalon, Huang *et al.* managed to introduce different intracavity losses for the two lasing wavelengths, leading to an equalization of their net gain [6]. For the Nd-doped crystals with quasi-three-level laser transitions (like 946 nm in Nd:YAG crystals), Lu *et al.* varied the reabsorption losses for different laser modes through controlling the temperature distribution of the crystal [7].

In contrast to the discrete and narrow gain peaks of the Nd-doped gain media, the Yb-doped gain media have continuous and broad gain spectra, each of which typically has a single peak. For many of the Yb-doped materials, however, the wavelength of the gain peak is highly dependent on the lasing polarization, making it possible to generate two wavelengths simultaneously from distinct polarizations. Fig. 4.1 shows the gain spectra for the polarizations parallel to the N_m-axis and the N_p-axis of the Yb:KGW crystal at different population inversion levels using equation (3-4) from Chapter 3. The wavelengths of the gain peaks for these two polarizations exhibit an offset with several nm (THz in frequency) spacing. Moreover, the value of the offset depends on the level of population inversion, therefore allowing a tunability of the spectral difference between the two wavelengths.

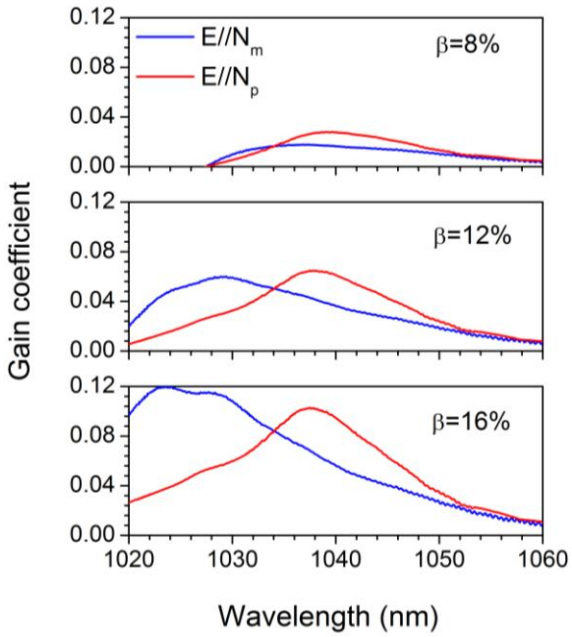

Fig. 4.1. Gain spectra of the Yb:KGW crystal for the N_m-polarization and the N_p-polarization at different population inversion levels.

So far, the potential of Yb-doped gain media in dual-wavelength operation remains underdeveloped. Yb:vanadates are one of the few where dual-wavelength emission has been observed [9-10]. In these works, however, the dual-wavelength emission was observed only at the proximity of the lasing threshold, resulting in low output power at both wavelengths. High power dual-wavelength emission (>6 W in total) was obtained from an Yb:YCOB oscillator, but with only one special output coupling [11]. Recently, the dual-wavelength operation with tunable spectral spacing was demonstrated by Brenier in an Yb:KGW oscillator [12]. However, the two laser wavelengths were actually independently generated from two regions of the Yb:KGW crystal, therefore leading to a complex setup and the requirement of additional optical components in the cavity.

In this chapter, I report on the demonstration of a high power simultaneous dual-wavelength emission from two polarizations of a simple CW Yb:KGW oscillator. Without inserting any optical components in a standard laser cavity, the gain equalization was realized by introducing additional polarization-dependent reabsorption losses to the N_m- and N_p-polarized modes. The dual-wavelength operation was achieved at different output coupler transmissions, thus allowing a tunable spacing between the two wavelengths.

4.2 Experimental design

In the presented work, the same N_g-cut Yb:KGW crystal slab (1.5 at.% doping, 5 mm × 8 mm × 1.2 mm) as described in Chapter 3 was used. The cavity configuration was similar to the one shown in Fig. 3.4 but excluded the BK7 plate. Without using any polarization selection component, both the N_m- and N_p-polarized laser modes were allowed to oscillate in the cavity. The Yb:KGW crystal was pumped by a maximum of 30 W radiation delivered from a fiber-coupled laser diode with 100 μm core diameter and 0.22 NA. The pump radiation was reimaged through the two achromatic doublets with 50 mm and 150 mm focal lengths, forming a beam waist of 300 μm in diameter at the center of the crystal.

The gain equalization for the N_m- and N_p-polarized modes was realized by introducing for each of them additional losses with different values which came from the reabsorption

in the unpumped regions of the crystal. Therefore, the laser beam was designed to be larger than the pump beam inside the crystal. As an example, the designed dimensions of the pump and laser modes inside the 5-mm-long Yb:KGW crystal, as well as the mode cross sections in the center plane of the crystal are shown in Fig 4.2 (a). The thermal lensing of the gain medium was not considered in the calculation. In fact, due to the anisotropic thermal lensing of the Yb:KGW crystal, the N_m- and N_p-polarized laser modes inside the crystal will be reshaped differently. Fig. 4.2 (b) and (d) present the N_m- and N_p-polarized laser mode profiles, respectively, at a certain distance away from the output coupler. An obvious difference in terms of the shapes and dimensions between the two modes can be observed. The modes inside the gain medium followed the same pattern, which can be traced through the ABCD matrix analysis (Appendix B). Their cross sections, as well as the pump mode in the crystal are schematically depicted in Fig. 4.2 (c) and (e). The N_m-polarized mode has an almost circular shape while the N_p-polarized mode has an elliptical shape with larger size in the horizontal direction. As a consequence, the N_p-polarized mode will suffer higher reabsorption losses in the unpumped region of the crystal.

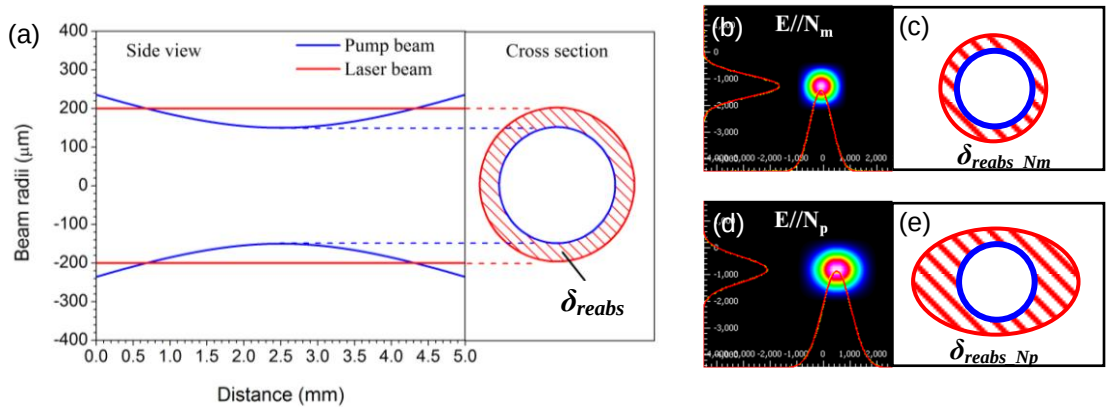

Fig. 4.2. (a) Side view and cross sections of the pump mode and the designed laser mode inside the crystal without considering the effect of anisotropic thermal lensing. (b) and (d) show the N_m- and N_p-polarized mode cross sections at a certain distance away from the output coupler; (c) and (e) schematically depict the comparison of the pump mode and the N_m- and N_p-polarized modes inside the gain medium.

The net gain at the lasing wavelength for the N_m- and N_p-polarized laser modes can be expressed as the following:

$$g_{n\_Nm}(\lambda_l) = g_{Nm}(\lambda_l) - \delta_{reabs\_Nm}, \tag{4-1}$$

$$g_{n\_Np}(\lambda_l) = g_{Np}(\lambda_l) - \delta_{reabs\_Np}. \tag{4-2}$$

The $g_{Nm}(\lambda_l)$ and $g_{Np}(\lambda_l)$ are the gain coefficients for the N_m- and N_p-polarized laser modes that are spatially well matched with the pump beam, that is, when no reabsorption in the unpumped regions was considered. Their values can be calculated from the equation (3-4). At the fractional population inversion of β < 13.2%, $g_{Np}(\lambda_l)$ higher than $g_{Nm}(\lambda_l)$ can be obtained (Fig. 4.3). The N_p-polarized mode then plays a dominant role if no special measures are taken. However, as the polarization-dependent reabsorption losses with $\delta_{reabs\_Np} > \delta_{reabs\_Nm}$ are introduced, the net gain for the N_m- and N_p-polarized modes can be equalized, allowing both of them to oscillate in the cavity. It is worth noting that since the strength of the thermal lensing depends on the pump power, the laser mode sizes and hence the introduced reabsorption losses are also power-dependent. Therefore, the dual-wavelength operation obtained using the presented method can be controlled by the pump power, and works in a certain pump power range.

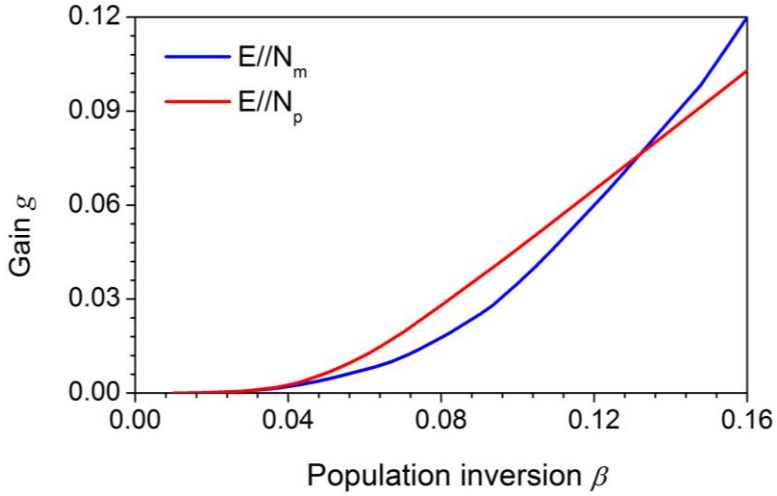

Fig. 4.3. The gain for the N_m- and N_p-polarizations at different population inversion levels.

4.3 Experimental results and discussion

4.3.1 Laser performance and dual-wavelength operation

In order to characterize the polarization state of the output laser beam, a polarizing beamsplitter cube (PBS) was placed after the output coupler. The measured output power for the N_m- and N_p-polarized modes as well as the total output power against the incident pump power is shown in Fig. 4.4. In the experiment, different output couplers with transmission of 1.6%, 3% and 5% were used. The lasing threshold was reached as the pump power was increased to 10.5 W, 12 W and 12.5 W for the three output couplers. Compared to the threshold pump power of the cavity with optimized mode matching (see Fig. 3.5), the higher threshold of the cavity presented in this work indicates the presence of additional reabsorption losses in the unpumped region. The 5% output coupler generated the highest output power of 4.6 W at the pump power of 26.8 W, of which 13.5 W was absorbed in the gain medium. This corresponds to a slope efficiency of ~75% with respect to the absorbed pump power.

The dual-wavelength operation was obtained at all three output coupler transmissions. Among them, the output coupler with a higher transmission enhanced the population inversion level and reduced the gain difference between the N_m- and N_p-polarized modes (Fig. 4.3). Correspondingly, the end HR mirror had to be moved a few millimeters away from the concave mirror R3 to obtain the dual-wavelength operation. Such movement allowed the reduction of the laser mode size in the crystal and further increase in the difference between the additional reabsorption losses introduced to the N_m- and N_p-polarized laser modes.

In the vicinity of the threshold pump power, only the N_p-polarized mode oscillated in the cavity. The N_m-polarized mode set in as the pump power was increased to 17.6 W, 16.6 W and 17.6 W for the 1.6%, 3% and 5% output couplers, respectively, leading to a competition with the N_p-polarized mode. A complete switching between the N_m- and N_p-polarized modes occurred in a relatively narrow power range, leaving only the N_m-polarized mode to oscillate in the cavity. As the pump power was increased to 21.8 W for the 1.6% output coupler and 20.7 W for the 3% output coupler, the N_p-polarized mode reappeared and coexisted with the N_p-polarized mode in much wider power ranges. The

reappearance of the N_p-polarized mode for the 5% output coupling happened at higher pump power of 24.7 W. The second switching between the two modes is believed to occur as the pump power is to increase to even higher levels.

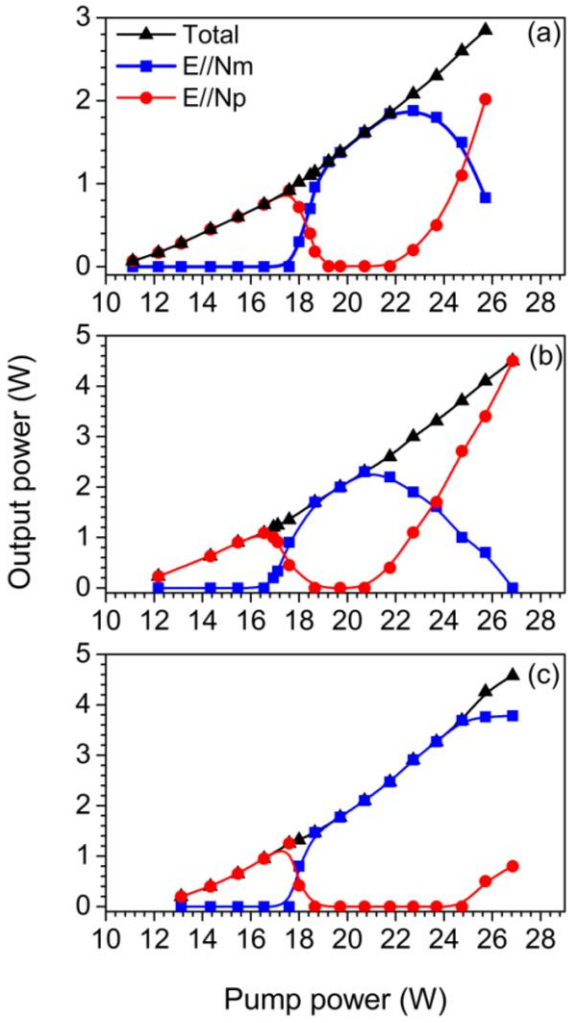

Fig. 4.4. The output power as a function of the pump power for dual-wavelength operation at different output coupler transmissions of 1.6% (a), 3% (b) and 5% (c).

The evolution of the emission spectrum at different output power for the 3% output coupler transmission is shown in Fig. 4.5. The lasing wavelength was 1029.5 nm for the N_m-polarized mode and 1037.9 nm for the N_p-polarized mode, corresponding to a spectral spacing of 8.4 nm in the dual-wavelength operation. The lasing wavelengths for the N_m- and N_p-polarized modes which oscillated at different output coupler transmissions are summarized in Table 4.1. A modest tunability of the spectral spacing can be observed.

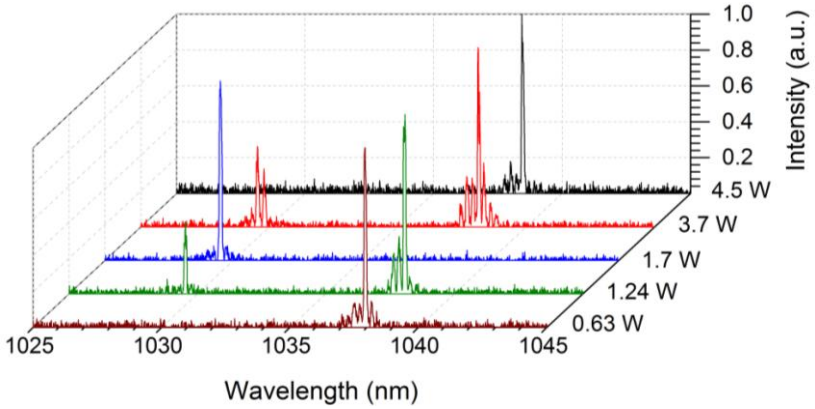

Fig. 4.5. The laser spectrum at different total output power levels (3% output coupling).

Table 4.1. Laser wavelengths for different output coupler transmissions

Output coupler transmission	**λ_m (nm) (E//N_m)**	**λ_p (nm) (E//N_p)**	**$\Delta\lambda$ (nm)**
1.6 %	1030.6	1038.4	7.8
3 %	1029.5	1037.9	8.4
5 %	1028.7	1037.5	9.1

4.3.2 Gain equalization

The observed switching and coexistence of the N_m- and N_p-polarized modes inside the cavity was attributed to the competition and equalization of their net gain at the lasing wavelength. As was mentioned, such equalization was induced by the effect of thermal lensing through reshaping of the laser modes inside the gain medium, which as a consequence, led to the polarization-dependent reabsorption losses in the unpumped regions of the crystal. In order to demonstrate this, we estimated the strength of thermal lensing and the sizes of the laser modes inside the cavity at various pump power levels (Fig. 4.6). The estimation was conducted with the 3% output coupler. As the incident pump power was increased, the thermal lensing became stronger, resulting in a reduction of the sizes of both the N_m- and N_p-polarized modes. On the other hand, the thermal lensing affected the laser modes very differently, depending not only on the polarization of the mode but also on the direction considered. In particular, the thermal lensing had a very weak effect on the horizontal direction of the N_p-polarized mode, therefore resulting in a much larger mode size and higher reabsorption in the unpumped region when compared to the N_m-polarized mode.

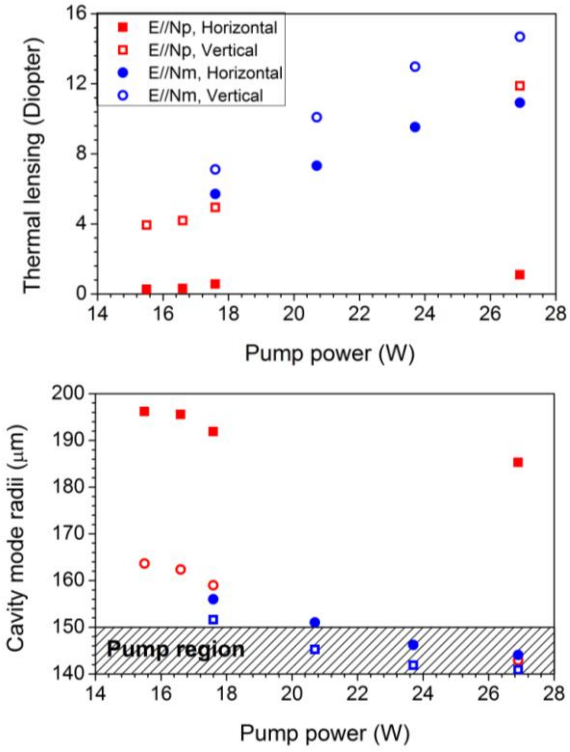

Fig. 4.6. The thermal lensing and the radii of the N_m- and N_p-polarized modes inside the gain medium as a function of the incident pump power.

At the threshold power level, both the N_m- and N_p-polarized modes were weakly focused by the thermal lensing of the gain medium. Although the N_p-polarized mode suffered higher reabsorption loss δ_{reabs_Np}, its larger gain g_{Np} at the lasing wavelength made its net gain g_{n_Np} higher when compared to that of the N_m-polarized mode g_{n_Nm} (i.e. $g_{n\_Np} > g_{n\_Nm}$). Therefore only the N_p-polarized mode oscillated in the cavity at this power level. The increase of the pump power allowed the N_m-polarized mode to be focused to smaller dimensions, leading to a reduction of the reabsorption loss δ_{reabs_Nm} and thus an increase in its net gain g_{n_Nm}. As the pump power was increased to 16.6 W (for the 3% output coupler), g_{n_Nm} was increased to a level comparable to the net gain of the N_p-polarized mode g_{n_Np} (i.e. $g_{n\_Np} \approx g_{n\_Nm}$). This equalized gain allowed both of the N_m- and N_p-polarized modes to oscillate in the cavity and started their competition as pump power was further increased. Due to the stronger thermal lensing effect for the N_m-polarized mode, it experienced larger reduction of the reabsorption loss than the N_p-polarized mode as the pump power was increased. This allowed the N_m-polarized mode to overtake the

N_p-polarized mode in the net gain competition and to become the dominant oscillating mode as the pump power was increased to 18.6 W.

At higher pump power levels (>20.7 W), the N_m-polarized mode was focused to a dimension similar to the pump mode, making its reabsorption loss in the unpumped region to reduce to a very low value close to zero. As a consequence, the gain of the N_m-polarized mode would no longer suffer additional losses, that is, the net gain was increased to its maximum value of g_{Nm} (i.e. $g_{n\_Nm} = g_{Nm}$). In contrast, the net gain of the N_p-polarized mode g_{n_Np} would continue to increase with the increase of the pump power. This allowed the g_{n_Np} reaching to a level comparable to the g_{Nm}, therefore leading to the second coexistence of both the N_m- and N_p-polarized modes. As the g_{n_Np} exceeded the g_{Nm} at higher pump power levels, the N_p-polarized mode would again play the dominant role and even fully suppress the N_m-polarized mode. In this gain equalization process, however, the reduction of the reabsorption loss δ_{reabs_Np} and thus the increase of the net gain g_{n_Np} for the N_p-polarized mode is less sensitive to the pump power, therefore allowing the coexistence of the N_m- and N_p-polarized modes to be observed in a broader pump power range.

4.4 Conclusion

In this Chapter, we reported on the simultaneous dual-wavelength emission from two orthogonal polarizations of a CW Yb:KGW oscillator. The gain equalization between the two lasing wavelengths was realized by introducing additional polarization-dependent reabsorption losses, which originated from the anisotropic thermal lensing effect owing to the reshaping of the laser modes. Two power ranges with dual-wavelength emission were obtained with the increase of the pump power. This unique feature has not been observed in other solid-state oscillators before. Moreover, the dual-wavelength emission was demonstrated with varied output coupler transmission, resulting in a modest tunability of the two lasing wavelengths as well as their spectral spacing. This technique is believed to be applicable to many other quasi-three-level Yb-doped laser materials with anisotropic lasing and thermal properties.

References

[1] Y. F. Chen, S. W. Tsai, S. C. Wang, Y. C. Huang, T. C. Lin, and B. C. Wong, "Efficient generation of continuous-wave yellow light by single-pass sum-frequency mixing of a diode-pumped Nd:YVO_4 dual-wavelength laser with periodically poled lithium niobate," Opt. Lett. **27**, 1809-1811 (2002).

[2] M. Alouini, M. Brunel, F. Bretenaker, M. Vallet, and A. Le Floch, "Dual tunable wavelength Er, Yb: glass laser for terahertz beat frequency generation," IEEE Photon. Technol. Lett. **10**, 1554 (1998).

[3] J. Yu, P. Rambaldi, and J.-P. Wolf, "Dual-wavelength diode-seeded Ti: sapphire laser for differential absorption lidar applications," Appl. Opt. **36**, 6864 (1997).

[4] L. Chen, Z. Wang, S. Zhuang, H. Yu, Y. Zhao, L. Guo, and X. Xu, "Dual-wavelength Nd:YAG crystal laser at 1074 and 1112 nm," Opt. Lett. **36**, 2554-2556 (2011).

[5] Y. F. Chen, "cw dual-wavelength operation of a diode-end-pumped Nd:YVO_4 laser," Appl. Phys. B **70**, 475–478 (2000).

[6] Y. P. Huang, C. Y. Cho, Y. J. Huang, and Y. F. Chen, "Orthogonally polarized dual-wavelength Nd:$LuVO_4$ laser at 1086 nm and 1089 nm," Opt. Express **20**, 5644-5651 (2012).

[7] Y. Lu, B. Zhang, E. Li, D. Xu, R. Zhou, X. Zhao, F. Ji, T. Zhang, P. Wang, and J. Yao, "High-power simultaneous dual-wavelength emission of an end-pumped Nd:YAG laser using the quasi-three-level and the four-level transition," Opt. Commun. **262**, 241–245 (2006).

[8] A. Brenier, Y. Wu, P. Fu, J. Zhang, and Y. Zu, "Diode-pumped laser properties of Nd^{3+}-doped $La_2CaB_{10}O_{19}$ crystal including two-frequency generation with 4.6 THz separation," Opt. Express **17**, 18730-18737 (2009).

[9] J. Liu, V. Petrov, H. Zhang, J. Wang, and M. Jiang, "High-power laser performance of a-cut and c-cut Yb:$LuVO_4$ crystals," Opt. Lett. **31**, 3294-3296 (2006).

[10] J. Liu, X. Mateos, H. Zhang, J. Wang, M. Jiang, U. Griebner, and V. Petrov, "Characteristics of a continuous-wave Yb:$GdVO_4$ laser end pumped by a high-power diode," Opt. Lett. **31**, 2580-2582 (2006).

[11] J. Liu, H. Zhang, J. Wang, and V. Petrov, "Output-coupling-dependent polarization state of a continuous-wave Yb:$YCa_4O(BO_3)_3$ laser," Opt. Lett. **32**, 2909-2911 (2007).

[12] A. Brenier, "Tunable THz frequency difference from a diode-pumped dual-wavelength Yb^{3+}:$KGd(WO_4)_2$ laser with chirped volume Bragg gratings," Laser Phys. Lett. **8**, 520–524 (2011).

Chapter 5

Powerful 67 fs Kerr-lens mode-locked prismless Yb:KGW oscillator

Instead of being delivered continuously in time, the lasing photons in ultrafast oscillators are constrained in a circulating "package" and are delivered in a periodic temporal manner, namely, in a train of laser pulses. The fundamental mechanism that forces the formation of laser pulses is the so-called mode locking (Section 5.1), which was firstly identified by Hargrove *el al.* in a He-Ne laser in 1964 [1]. Development of the mode locking techniques over the last several decades dramatically shortened the pulse duration, allowing sub-10 fs pulses to be routinely generated from Ti:sapphire laser oscillators [2-4].

For Yb-doped oscillators, operation at high average power (>1 W) with sub-100 fs pulses, however, still remains quite challenging. Such a mode locking regime is accompanied by an increased influence of nonlinear effects, which necessitates careful management of the intracavity dispersion. At the same time, uncompromised performance of the mode locking mechanism is needed to sustain ultrashort pulse generation effectively and to alleviate increased pulse instabilities. This is a nontrivial task for semiconductor saturable absorber based pulse generation (Section 5.1.1) and as a result higher output power usually comes at the cost of longer pulse duration. For example, Yb:KGW lasers have produced 10 W of output power with 433 fs pulses [5] and 126 mW with 100 fs pulses [6]. Similarly, a laser based on a sister material, Yb:KYW, generated 14.6 W and 450 fs pulses [7] while 65 fs pulses were produced at 22 mW [8]. The same trend is found in thin-disk oscillators [9]. As an alternative to semiconductor saturable absorbers, Kerr-lens mode locking (KLM) (Section 5.1.2) is a well-established technique that produces ultrashort pulses and is routinely used for the generation of sub-10 fs pulses from Ti:sapphire oscillators [2-4]. Unlike semiconductor absorbers, KLM exhibits a purely electronic response, thus acting as a fast saturable

absorber. This is beneficial for enhanced pulse shortening and increased mode locking stability against the continuous wave background radiation present in a cavity. Therefore, the fast saturable absorber-like action of KLM is attractive for the generation of intense ultrashort pulses.

In this Chapter, I report on a powerful mode-locked Yb:KGW bulk oscillator, which is based on dual action of Kerr-lens and saturable absorber (KLAS) mode locking. The mode locking was initiated by a semiconductor saturable absorber. The laser cavity in the optimized mode-locked regime delivered pulses with 67 fs duration at a repetition rate of 77 MHz. The average output power reached 3 W, which to the best of my knowledge, makes it the most powerful Yb-ion bulk laser oscillator at this level of pulse duration.

In the first section of this chapter, the principles of mode locking (especially in the passive way), including the two widely used mode locking techniques are outlined. The dispersion management, which is a key factor for obtaining very short pulses, will also be addressed. Then the design and optimization of the oscillator operated in the mode-locked regime are discussed. The obtained laser performance will be shown and compared to the previously reported results from other Yb-ion bulk oscillators.

5.1 Principles of mode locking

Mode locking, as implied by its name, refers to "locking" of the longitudinal laser modes in phase such that they can interfere constructively in a cavity to form very short pulses. In a Fabry-Parot cavity with length L, multiple discrete longitudinal modes are allowed to exist with a frequency interval $\Delta f=c/2L$, where c is the speed of light. In a free-running laser, these longitudinal modes have neither well-defined amplitude nor phase relationship. The output light is a statistical average of all oscillating modes, which in this case will exhibit series of chaotic spikes around an average value. If all the longitudinal modes, on the other hand, are forced to establish a coherent phase relationship, their constructive superposition at one point will finally form an intense ultrashort laser pulse (Fig. 5.1). According to the Fourier theorem, the pulse width is inversely proportional to the number of modes that are oscillating in the cavity, i.e. to the spectral bandwidth. Assuming a transform-limited pulse with Gaussian intensity profile, its temporal width

(FWHM, Full width at half maximum) τ_p and spectral bandwidth (FWHM) $\Delta\nu$ follow the relation:

$$\tau_p \Delta\nu = 0.44\,. \tag{5-1}$$

For a transform-limited pulse with hyperbolic secant ($sech^2$) intensity profile, the product of its temporal width τ_p and spectral bandwidth $\Delta\nu$ yields:

$$\tau_p \Delta\nu = 0.315\,. \tag{5-2}$$

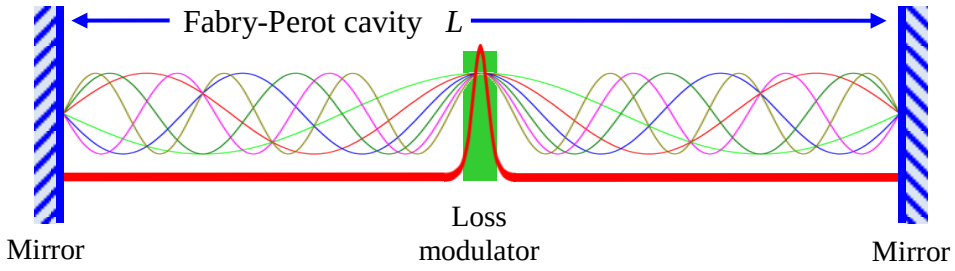

Fig. 5.1. Schematic illustration of the pulse formation in a Fabry-Perot cavity with six longitudinal modes locked in phase. Each sinusoidal wave with a specific wavelength corresponds to a longitudinal mode. The longitudinal modes have a frequency interval $\Delta f=c/2L$.

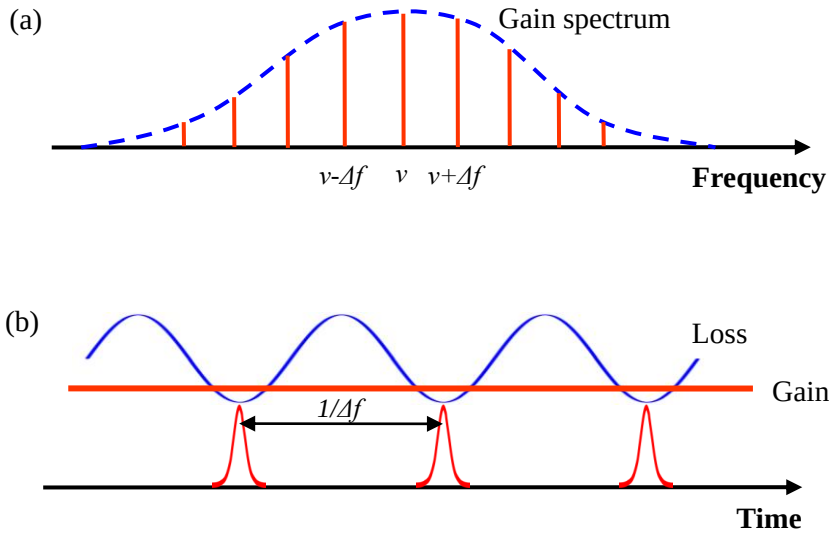

Fig. 5.2. The mode locking process in frequency domain (a) and time domain (b).

A general method for "locking" of the laser modes is to introduce a weak and periodic loss that is synchronized with the round-trip circulation time ($1/\Delta f$) of the pulse, either by an external signal applied to an intracavity modulator (i.e. active mode locking) or by an internal saturable absorber (i.e. passive mode locking). The active mode locking is usually achieved by incorporating an acousto-optic or electro-optic modulator, which uses the externally applied driving signal to modulate either the amplitude or the phase of the modes at a frequency of Δf, leading to a periodic loss of the light energy. In the frequency domain (Fig. 5.2 (a)), the modulation of a mode with frequency v generates sidebands with frequencies $v+\Delta f$ and $v-\Delta f$, allowing the energy to partially flow from the parent mode to the sideband modes. In this way, more sidebands with frequencies $v+n\Delta f$ and $v-n\Delta f$ (n=1, 2, 3…) will be generated until the frequency is out of the lasing gain bandwidth of the oscillator. The injection of the sidebands to their neighboring modes will couple all the modes in phase, resulting in their constructive interference and pulse formation.

The understanding of the mode locking process in time domain (Fig. 5.2 (b)) is based on the synchronization of the pulse round-trip circulation time and the loss modulation period, which defines a zero-loss window (or net gain window) with short duration. Only the circulating energy that passes through the modulator at the "correct" time in each round-trip would experience zero-loss window and would be amplified, while the rest would be attenuated or phased out of the gain profile. The pulse width obtained in this way is limited only to the picosecond range because the modulators cannot be operated at a very fast modulating rate.

If the net gain window is controlled by the pulses themselves rather than by the external electrical signal, its timescale will be at the same level with the pulses. Therefore the passive way of achieving the mode locking can generate extremely short pulses in the femtosecond regime. In this case, a saturable absorber is employed as the loss modulator, which is driven by the generated laser pulses. The shorter the pulses, the faster the loss modulation rate can be obtained. At present, the saturable absorber is usually provided in the two forms: 1) the slow saturable absorber, e.g. semiconductor saturable absorber mirror (SESAM), and 2) the fast saturable absorber, e.g. Kerr lensing effect. In the following, I will briefly introduce these two passive mode locking techniques, and then

will give a comparison between them, which can provide us with a guideline in the designing of a mode-locked oscillator.

5.1.1 SESAM mode locking

In general, SESAM is an integrated version of an InGaAs or GaAs quantum-well and a Bragg reflector on a single wafer [10]. The former one acts as a saturable absorber, while the later one acts as a highly reflective mirror. The saturable absorber exhibits a nonlinear transmission depending on the intensity of the incident radiation. As a pulse is incident onto the SESAM, its leading edge with low intensity would be absorbed while the intense central part would cause saturation of the absorption and thus bleach the absorber, allowing it to pass the absorber without experiencing any loss (ideally). However, the complete recovery of the bleached absorber requires much longer time (on picosecond or nanosecond time scale) than the pulse duration. The loss modulation, therefore, has its effect only on the leading edge of the incident pulses but not on the trailing edge. So the SESAM is usually used to initiate and maintain the mode locking. In order to shorten the pulses, the SESAM mode locking necessitates operation in the soliton regime by introducing intracavity negative group velocity (GVD) dispersion [11]. During propagation through the gain medium, the pulses will be chirped with a red-shifted frequency at the leading edge and a blue-shifted frequency at the trailing edge. Appropriate amount of negative GVD compensation then can remove the acquired group delay between the different frequency components, leading to the formation of a soliton pulse circulating in the cavity.

The ability of SESAM to initiate the mode locking facilitates the simplicity and flexibility of the laser cavity design and operation, allowing for the mode locking to be self-starting and for the laser to operate at the center of the cavity stability region. Nevertheless, the saturation and slow bleaching recovery dynamics of the SESAM can cause the onset of mode locking instabilities. The Q-switched mode-locking (QML) and multi-pulsing mode locking are the two major instabilities that one might encounter. Unlike the CW mode locking regime, the peak intensity of the pulses in the Q-switched mode locking is modulated and the pulses are enclosed in a modulated envelope with a much longer duration (~μs-ms). Such phenomenon is not desired owing to its large pulse

width and low repetition rate. It can be suppressed simply by increasing the intracavity pulse energy to satisfy the following condition [12]:

$$E_{in}^2 > E_{sat,G} E_{sat,A} \Delta R, \tag{5-3}$$

where E_{in} is the intracavity pulse energy, $E_{sat,G}$ is the saturation energy of the gain medium, and $E_{sat,A}$ is the saturation energy of the absorber. ΔR is the modulation depth of the SESAM, which indicates the maximum loss difference between the high intensity and low intensity light.

Very high intracavity pulse energy, on the other hand, would increase the possibility of multi-pulsing instability, i.e. where one pulse breaks into two or multiple pulses with lower energy [10]. One possible reason is attributed to the small modulation depth (typically 0.5-2%) of the SESAM, which can be not sufficient to discriminate the mode locking against the CW background present in a cavity. The growth of the continuous wave background at high power (energy) levels would completely destabilize the desired single pulse mode locking. As a consequence, the multi-pulsing instability limits the output power (energy) that can be reached. Introducing a larger amount of GVD compensation in the cavity can suppress this instability albeit at the expense of longer pulse duration.

5.1.2 Kerr-lens mode locking

Kerr lensing usually comes from the third-order nonlinearity of the gain medium. In contrast to the SESAM, the Kerr lens acts as a fast saturable absorber with a very short absorption recovery time (as short as 10^{-15} s). Considering an oscillating pulse with Gaussian intensity profile *I(r,t)*, the intense pulse can modulate the originally homogeneous refractive index of the gain medium through the third-order nonlinear refractive index n_2:

$$n(r,t) = n_0 + n_2 I(r,t). \tag{5-4}$$

The modulated refractive index usually makes the gain medium to act as a positive lens. The central part of the pulse with higher intensity, both temporally and spatially, experiences stronger focusing than the peripheral parts. An aperture placed behind the gain medium can then bring a loss modulation to the pulse: only the very central part with high enough intensity to focus the beam to a smaller size can pass through the aperture

freely and get amplified, while the leading and trailing edges of the pulse with weak intensity will be cut off by the aperture, leading to a shortened pulse (Fig. 5.3). The aperture can either be a real one (a.k.a. hard aperture) or an artificial one (a.k.a. soft aperture). The latter one is realized by tightly focusing the pump beam into the gain medium to create a small gain volume. Only the very central part of the lasing pulse can be focused into the gain region and get amplified, leading to an extremely short pulse.

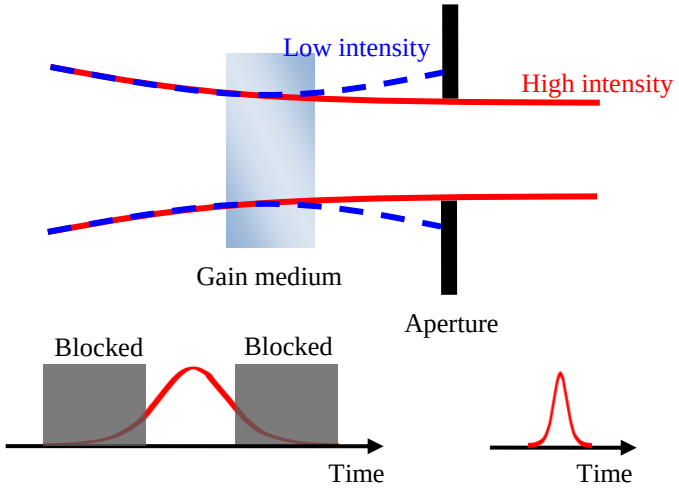

Fig. 5.3. Pulse formation in hard aperture Kerr-lens mode locking.

Besides the self-focusing, the pulse induced modulation of the refractive index has another important effect to consider: self-phase modulation (SPM). This results in the broadening of the pulse spectrum, which brings the KLM an additional benefit of shortening of the generated pulse. On the other hand, in order to achieve an efficient aperturing, the KLM laser is usually operated near the stability limits of the cavity, making it quite sensitive to the disturbance and misalignment of the optical components. Additionally, unlike the SESAM mode locking, the KLM cannot usually start by itself, and often a slight tapping of one of the end mirrors is needed.

5.1.3 KLAS mode locking

As was mentioned above, the low saturation energy and long absorption recovery time of SESAM, on one hand, relax the energy requirement of initially long pulses during the build-up period of the mode locking, therefore allowing for SESAM mode locking to be easily initiated and operated at the center of the cavity's stability region. On the other

hand, SESAM mode locking suffers from instabilities at high power level as more noise is allowed to pass through the absorber within the long absorption recovery window. In contrast, the fast closure of the saturation window in case of the KLM prevents the noise from passing through therefore resulting in higher stability and thus allowing generation of higher energy pulses.

The idea of KLAS mode locking which was developed in this thesis combines the advantages from both mode locking mechanisms, i.e. the SESAM initiates and maintains the mode locking while KLM suppresses the QML and multi-pulse mode locking instabilities at high power levels. Besides, the KLM with its ultrafast response dynamics and spectral broadening effect (through SPM) will play a significant role in pulse shaping. As a consequence, KLAS mode locking is very promising to generate sub-100 fs pulses at high power levels which will be demonstrated in this and the next Chapters.

KLAS abbreviation was used specifically to distinguish this new mode locking regime from the pure KLM, SESAM or SESAM-assisted KLM. The latter usually refers to the KLM configured lasers (i.e. operating near the stability edge of a cavity) where saturable absorbers are used only to ensure self-starting KLM behavior. The SESAM used in such a case could have a modulation depth as low as <0.1% [13]. In such lasers pure KLM can still be achieved even without saturable absorber in the cavity and usually requires some mechanical perturbation (like a tap on a mirror) to start the mode locking. The mode locking in the pure KLM regime behaved very similar to its counterpart with the assistance of a SESAM [13-14]. The developed KLAS mode locking regime is different from this situation because in it the mode locking is basically divided between the SESAM and KLM and it is not possible to achieve one mode locking process without the other. It will be shown in 5.3.2 that although the KLM suppressed the mode locking instabilities and broadened the spectral bandwidth, this process could not be achieved without the SESAM, since the laser was operated at the middle of a large cavity's stability range. This means that, unlike in the SESAM-assisted KLM case, the parameters of the SESAM play a significant role in the KLAS mode locking regime. Therefore, the observed regime can be described as a dual action of the Kerr-lens and saturable absorber (KLAS) mode locking mechanisms, extending the parameter space of these two mode locking techniques.

5.1.4 Dispersion management

In the mode-locked operation, a broadband pulse that passes through a gain medium and other intracavity components (even the air) will be temporally stretched due to the velocity mismatch between the different spectral components, i.e. the group velocity dispersion (GVD). Stabilization of the pulses, in most cases, necessitates an introduction of appropriate amount of negative dispersion to counteract the positive dispersion, which originates mainly from the gain medium and the self-phase modulation. One approach is to incorporate a pair of intracavity prisms, which are cut at Brewster's angle to minimize the insertion losses. The first prism provides angular dispersion and the second one recollimates different spectral components, therefore effectively introducing a negative dispersion. A round-trip of the prism sequence leaves a spectrally recombined but temporally compressed pulse. In fact, besides the negative dispersion, the prisms also provide some positive dispersion (but relatively small amount) arising from the pulse travelling through the material of the prisms.

An alternative approach for dispersion compensation is to use Gires–Tournois interferometer (GTI) mirrors, which are composed of a partially reflective front mirror and a highly reflective (ideally 100%) rear mirror, forming a Fabry-Perot resonator in between. Different spectral components of an incident pulse will be changed in phase, allowing the reflection of a negatively dispersed pulse. Compared to the prism pair, the GTI mirrors have very low insertion losses (reflectivity > 99.9%) and low sensitivity to misalignment, making them well suited to be employed for reliable generation of high power ultrashort pulses. As an example, the reflectivity and dispersion spectra of a GTI mirror (Layertec GmbH) with -250 ± 75 fs^2 GVD in the 980-1100 nm region are shown in Fig. 5.4.

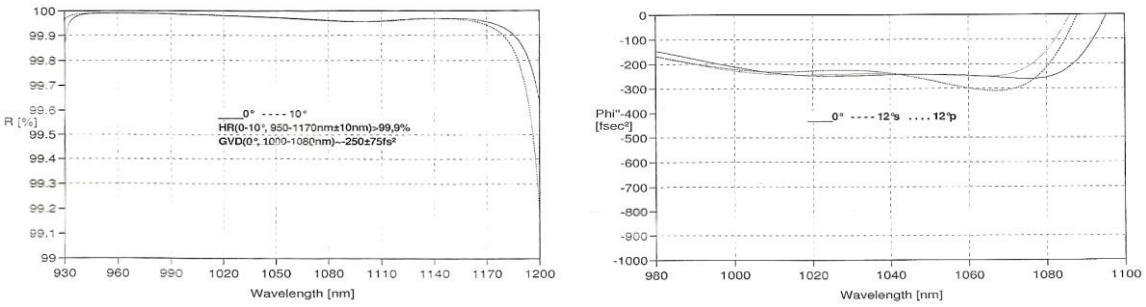

Fig. 5.4. The reflectivity and dispersion spectra of a GTI mirror coated for high reflection (> 99.9%) in the 950-1170 nm region, and introducing a negative dispersion of 250 ± 75 fs^2 in the 980-1100 nm region.

5.2 Experimental setup

The Yb:KGW crystal (Eksma) used in the experiment had a slab geometry which was 5 mm long (along the beam propagation direction) and 1.2 mm thick. The crystal with 1.5 at.% doping level was antireflection coated and cut along the N_g-axis. When compared to the commonly used 5 at.% doped crystals, the lower doping level is more adequate for generating shorter pulses since a higher level of population inversion can be reached under the same pump conditions, leading to spectral broadening of the gain [15]. The crystal was pumped at normal incidence with a maximum of 30 W of pump radiation delivered from a fiber-coupled diode laser (100 μm core diameter, 0.22 NA). The pump beam was reimaged into the crystal by a 1:3 imaging module consisting of two achromatic doublets, forming a beam waist of 300 μm at the center of the crystal. To optimize the spatial matching between the pump and cavity modes, the Z-fold cavity depicted in Fig. 5.5 was designed. The crystal was placed between two highly reflective (HR) concave mirrors R1 and R2 (radii of curvature r = 300 mm), resulting in a cavity mode size of around 300 μm inside the crystal. The collimated cavity mode in the long arm was further focused by a third HR concave mirror R3 (r = 500 mm) onto the output coupler. The distance between the output coupler and R3 could be precisely adjusted through a micrometer driven translation stage. This allowed for continuous control of the cavity mode size inside the crystal.

The initial “cold” cavity design was optimized for KLM performance by treating the Kerr effect as an additional positive intracavity lens [16] with variable focal length. All HR cavity mirrors were designed to exhibit low group velocity dispersion at the laser wavelength (Laseroptik GmbH). Two Gires-Tournois interferometer (GTI) mirrors (Layertec GmbH) were inserted into the long arm, providing a negative round-trip dispersion of 3200 fs^2 to balance the positive dispersion of about 1700 fs^2 introduced by the crystal and the additional chirp due to self-phase modulation.

The short arm of the cavity was terminated with a semiconductor saturable absorber mirror (SESAM, Batop GmbH) which was designed for 1040 nm wavelength with a modulation depth of 2%. The SESAM was used to initiate KLM operation. The spot size on the SESAM was designed to be about 500 μm in diameter in order to tolerate the high intracavity power. To achieve high output power an output coupler with higher transmittance should be used. On the other hand, lower transmittance is desirable for obtaining shorter pulses in the mode locking regime because of the lower laser gain [15]. Considering these contradictory requirements, an output coupler with 10% transmittance at the lasing wavelength was chosen. The cavity length resulted in a repetition rate of 77 MHz in single pulse mode-locked operation.

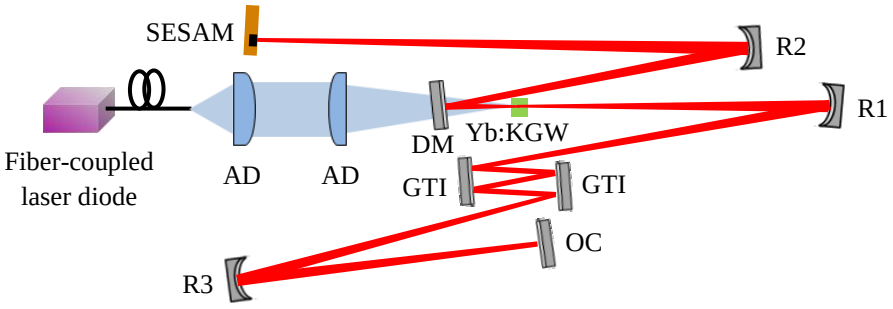

Fig. 5.5. Experimental setup of Kerr-lens mode-locked Yb:KGW oscillator. AD: achromatic doublets; DM, dichroic mirror; GTI: Gires-Tournois interferometer; R1, R2, R3: concave mirrors; OC: output coupler.

5.3 Experimental results

5.3.1 CW operation

In preliminary experiments the cavity was optimized for operation in the CW regime by using an HR mirror in the short cavity arm instead of the SESAM. The CW output power reached 6 W with 30 W of pump power incident on the crystal. The laser radiation was polarized parallel to the N_m-axis. The pump power absorption under non-lasing conditions was measured to be 50-60%, depending on the power level. A pump-power-dependent thermal lens, along with the Kerr lens, is always present as a parasitic factor when the laser operates in the pulsed regime, which affects the cavity's stability, beam astigmatism and starting of the KLM. The thermal lens strength was estimated in the CW regime by measuring the variation of the beam size away from the output coupler and then finding the lens strength using the ABCD matrix method as was described in Chapter 2. With 30 W of pump power incident on the crystal (~18 W absorbed), the thermal lens strength was determined to be about 10 diopters. Taking the thermal lensing into account, the cavity was designed to be operated close to the center of the stability region and the cavity mode was well matched with the pump mode inside the crystal. The output beam had an almost circular spatial profile (see Fig. 5.8).

5.3.2 Mode locking regimes

As the HR mirror was replaced by the SESAM, a Q-switched mode locking (QML) regime with large fluctuations in the envelope amplitude was instantly observed. The average power dropped to 4 W because of the large non-saturable loss of ~2% of the SESAM. The strong tendency towards QML instability was caused by the large spot size on the SESAM, leading to a low fluence of ~200 $\mu J/cm^2$, which is less than 3 times its saturation fluence (~70 $\mu J/cm^2$). In this case, the QML regime was purely initiated and governed by the SESAM. The spectral width of the QML pulses was ~5 nm. As the cavity length was adjusted so that the cavity mode size became larger than the pump spot, a soft aperturing via the Kerr lensing effect was effectively introduced, leading to an increased discrimination between the CW/QML and mode-locked regimes. During this procedure, the Kerr lensing effect gradually became stronger such that the KLM began to play more important role in suppressing the instabilities. Along with the SESAM mode

locking, the KLM eventually stabilized the mode locking in a single-pulse regime. This can be seen in Fig. 5.6 which shows different mode locking regimes during the optimization of the cavity length at maximum pump power of 30 W: QML was followed by a multi-pulse operation, which eventually led to a stable mode locking with a single pulse inside the cavity.

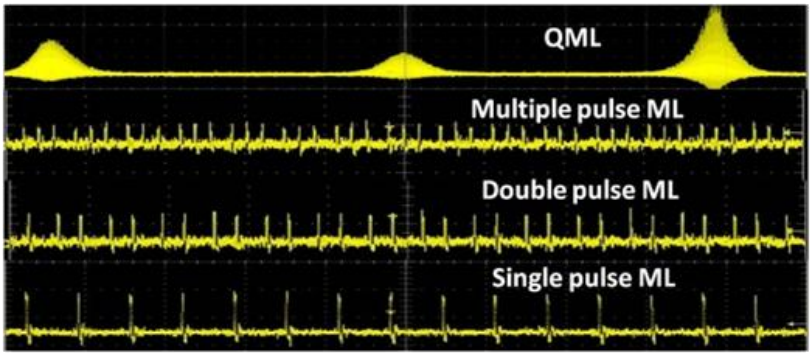

Fig. 5.6. Shape of the pulse trains in different mode locking regimes.

Initially, as the output coupler was translated several millimeters closer to R3, the QML instability was suppressed and gave way to multiple-pulse mode locking. According to the soliton theory [11], this regime is caused by incomplete discrimination between mode locking and amplification of the continuum. In this regime the average output power decreased to 3.6 W and the spectrum was broadened to ~9 nm. With further increase of the cavity mode size, the double-pulsing regime was reached, indicating better suppression of the multiple-pulse instabilities by the Kerr lensing. In this domain, the emission spectrum was measured to be ~11 nm wide and the average output power further decreased to 3.5 W. As the cavity was completely optimized (at ~20 mm away from the starting point), the multiple-pulse instability was fully suppressed, resulting in the oscillation of a single pulse inside the cavity. As a result a broad spectrum with a bandwidth of 16.8 nm (FWHM) centered at 1032 nm was obtained (Fig. 5.7). At this point the SESAM was weakly saturated with a fluence of only ~170 $\mu J/cm^2$, indicating the critical role of KLM in stabilization of the single-pulse mode locking. Besides, the largely broadened spectrum of the pulses demonstrated the role of KLM in pulse shaping in the sub-100 fs regime. On the other hand, it should be noted that pure KLM without the SESAM was not achieved in this experiment. This indicates that this laser resulted

from the KLAS mode locking approach (as described in 5.1.3) which combined the KLM for shaping and stabilizing the sub-100 fs pulses with a SESAM for self-starting and maintaining of the mode locking. A similar transition from multiple-pulse SESAM-based mode locking to single-pulse KLM operation was also observed in Yb:Sc_2O_3/Y_2O_3 laser [17].

To illustrate the effect of Kerr lensing on pulse duration, an additional experiment was performed where stable SESAM-based mode locking was achieved in a cavity that was not optimized for KLM. The output power was similar. The spectral bandwidth of the mode-locked pulses, however, was only to 5-6 nm, which is consistent with previously reported results [18].

5.3.3 Characterization of single pulsed regime

The autocorrelation trace of the pulses was acquired by using a commercial long range (200 ps) autocorrelator (Femtochrome, FR-103XL) and is shown in Fig. 5.7. The longer time ranges were monitored with a fast photodiode and an oscilloscope with combined resolution of ~100 ps. Assuming a *sech*^{2} temporal shape, the typical pulse duration at the output of the laser was determined to be 68 fs. The time-bandwidth product was calculated to be 0.32, indicating transform-limited operation. The average output power was 3 W, resulting in a pulse energy of more than 38 nJ and a peak power of more than 570 kW. This is, to the best our knowledge, the highest average output power achieved with such a short pulse duration from an Yb-ion based bulk laser oscillator. The optical-to-optical efficiency with respect to the incident pump power was 10%. The shortest measured pulse duration was 67 fs at the same output power level.

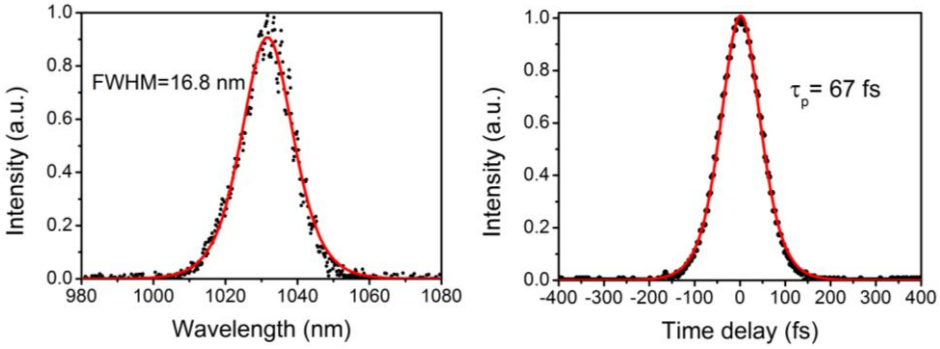

Fig. 5.7. Measured spectrum and autocorrelation trace of the pulses with fits assuming a sech2 profile. The pulse duration was determined to be 67 fs.

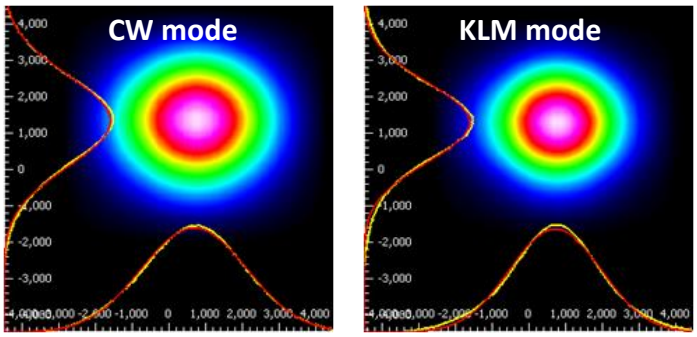

Fig. 5.8. Beam profiles of the CW and mode-locked output beams.

In Fig. 5.8 the output beam intensity profiles in the CW and KLAS mode locking regimes are displayed. The beam shape in the KLAS mode locking regime had an almost circular profile, but with a smaller diameter than the output beam in the CW regime due to self-focusing of the cavity mode inside the crystal. The beam quality factor M^2 was measured to be close to 1.1. In contrast to traditional KLM lasers, which usually operate at the edge of the stability region in order to maximize self-amplitude modulation, the laser described in this article operated close to the center of the stability region. In this case the self-amplitude modulation responsible for the initiation of the mode locking process was effectively provided by the SESAM. Unlike KLM cavities with tightly focused laser beams inside the crystal, the described cavity had a much broader stability range and lower sensitivity to optical misalignment, leading to much easier alignment and better performance on a daily basis.

The peak intensity of the oscillating pulse inside the cavity was calculated to be ~0.8 GW/cm^2. Such high intensity may cause additional nonlinear loss in the Yb:KGW crystal because of its large coefficient of stimulated Raman scattering. During the experiments, however, no stimulated Raman scattering was observed. This can be explained by the transient nature of the process, which leads to an increased threshold of this process [19].

5.4 Comparison with previous results

As a comparison, the performance of previously reported Yb-ion bulk lasers is summarized in Fig. 5.9 [8, 17, 20-27]. Very short pulses with durations of <70 fs have been generated by many Yb-doped materials, either with a SESAM or Kerr-lens mode

locking. In most cases, however, the average output power was limited to tens or hundreds of mW. As a notable exception, in Tokurakawa's work KLM proved its potential in power scaling of ultrashort pulse generation, demonstrating 66 fs pulses at an average output power of 1.5 W from a dual-gain medium (Yb:Sc_2O_3 and Yb:Y_2O_3) [17]. In contrast, in this work only a single gain medium was used and the average output power was improved by a factor of two with similar pulse duration. In another recent KLM experiment, 2.3 W were produced from an Yb:CaF_2 laser with 75 fs pulses and extracavity compression down to 68 fs. This laser, however, was not directly diode-pumped and required a diffraction limited pump beam [27].

The output power of our setup was limited by the available pump power and the non-saturable losses of the SESAM. Power scaling beyond 10 W may be possible with Kerr-lens mode-locked thin-disk oscillators, where 17 W of average output power with 200 fs pulse duration was reported using an Yb:YAG crystal [13]. Alternatively, generation of even shorter powerful pulses may require the use of a broadband gain medium such as Yb:CALGO, which was recently shown to produce 80 fs pulses at 8 W output power in a bulk configuration [28], and 62 fs pulses at 5.1 W output power in a thin-disk configuration [29].

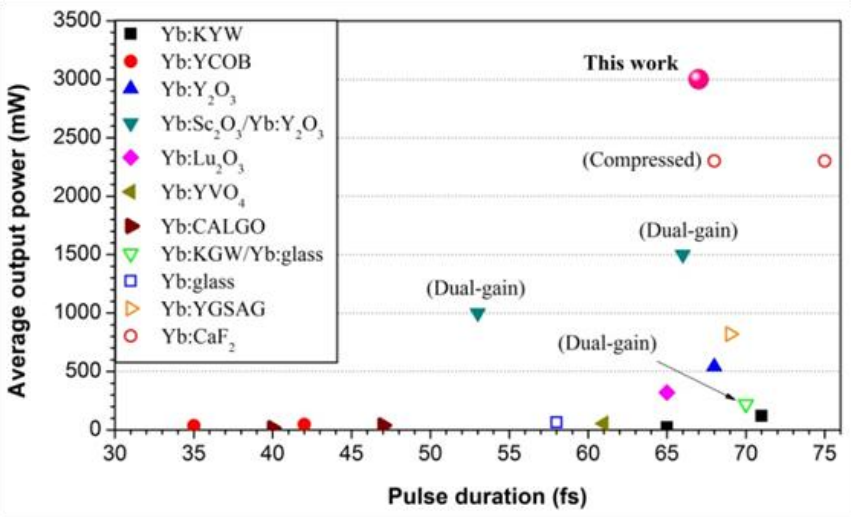

Fig. 5.9. Average output power of mode-locked Yb-ion bulk lasers versus pulse duration.

5.5 Conclusion

In conclusion, we have demonstrated a high power KLAS mode-locked Yb:KGW laser. With optimized dispersion compensation, the laser delivered pulses with 67 fs duration at a repetition rate of 77 MHz. The average output power reached 3 W, which to the best of our knowledge makes it the most powerful Yb-ion bulk laser oscillator at this level of pulse duration. Correspondingly, a pulse energy of >38 nJ and a peak power of >570 kW has been reached. Excellent performance of this laser system has prompted further research into its power scaling, which will be discussed in the work presented in the next chapter (Chapter 6).

References

[1] L. E. Hargrove, R. L. Fork, and M. A. Pollack, "Locking of He-Ne Laser Modes Induced By Synchronous Intracavity Modulation." Appl. Phys. Lett. **5**, 4-6 (1964).

[2] U. Morgner, F. X. Kärtner, S. H. Cho, Y. Chen, H. A. Haus, J. G. Fujimoto, E. P. Ippen, V. Scheuer, G. Angelow, and T. Tschudi, "Sub-two-cycle pulses from a Kerr-lens mode-locked Ti:sapphire laser," Opt. Lett. **24**, 411-413 (1999).

[3] R. Ell, U. Morgner, F. X. KÃÂrtner, J. G. Fujimoto, E. P. Ippen, V. Scheuer, G. Angelow, T. Tschudi, M. J. Lederer, A. Boiko, and B. Luther-Davies, "Generation of 5-fs pulses and octave-spanning spectra directly from a Ti:sapphire laser," Opt. Lett. **26**, 373-375 (2001).

[4] L. Xu, G. Tempea, A. Poppe, M. Lenzner, Ch. Spielmann, F. Krausz, A. Stingl, and K. Ferencz, "High-power sub-10-fs Ti:sapphire oscillators," Appl. Phys. B **65**, 151-159 (1997).

[5] G. R. Holtom, "Mode-locked Yb: KGW laser longitudinally pumped by polarization-coupled diode bars," Opt. Lett. **31**, 2719-2721 (2006).

[6] G. Paunescu, J. Hein, and R. Sauerbrey, "100-fs diode-pumped Yb:KGW mode-locked laser," Appl. Phys. B **79**, 555-558 (2004).

[7] A.-L. Calendron, K.S. Wentsch, and M.J. Lederer, "High power cw and mode-locked oscillators based on Yb:KYW multi-crystal resonators," Opt. Express **16**, 18838-18843 (2008).

[8] A. Schmidt, S. Rivier, V. Petrov, U. Griebner, G. Ebert, A. Gross, V. Wesemann, S. Vernay and D. Rytz, "65 fs diode-pumped diffusion-bonded Yb:$KY(WO_4)_2$/ $KY(WO_4)_2$ laser," Electron. Lett. **46**, 641-643 (2010).

[9] C. J. Saraceno, O. H. Heckl, C. R. E. Baer, C. Schriber, M. Golling, K. Beil, C. Kränkel, T. Südmeyer, G. Huber, and U. Keller, "Sub-100 femtosecond pulses from a SESAM modelocked thin disk laser," Appl. Phys. B **106**, 559-562 (2012).

[10] U. Keller, K. J. Weingarten, F. X. Kärtner, D. Kopf, B. Braun, I. D. Jung, R. Fluck, C. Hönninger, N. Matuschek, and J. Aus der Au, "Semiconductor saturable absorber mirrors (SESAM's) for femtosecond to nanosecond pulse generation in solid-state lasers," IEEE J. Sel. Top. Quantum Electron. **2**, 435-453 (1996).

[11] F. X. Kartner, I. D. Jung, and U. Keller, "Soliton mode-locking with saturable absorbers," IEEE J. Quantum Electron. **2**, 540-556 (1996).

[12] U. Keller, "Recent developments in compact ultrafast lasers," Nature **424**, 831-838 (2003).

[13] O. Pronin, J. Brons, C. Grasse, V. Pervak, G. Boehm, M.-C. Amann, V. L. Kalashnikov, A. Apolonski, and F. Krausz, "High-power 200 fs Kerr-lens mode-locked Yb:YAG thin-disk oscillator," Opt. Lett. **36**, 4746-4748 (2011).

[14] D. H. Sutter, G. Steinmeyer, L. Gallmann, N. Matuschek, F. Morier-Genoud, U. Keller, V. Scheuer, G. Angelow, and T. Tschudi, "Semiconductor saturable-absorber mirror assisted Kerr-lens mode-locked Ti:sapphire laser producing pulses in the two-cycle regime," Opt. Lett. **24**, 631-633 (1999).

[15] C. Hönninger, R. Paschotta, M. Graf, F. Morier-Genoud, G. Zhang, M. Moser, S. Biswal, J. Nees, A. Braun, G. A. Mourou, I. Johannsen, A. Giesen, W. Seeber, and U. Keller, "Ultrafast ytterbium-doped bulk lasers and laser amplifiers," Appl. Phys. B **69**, 3-17 (1999).

[16] A. Major, J. S. Aitchison, P. W. E. Smith, F. Druon, P. Georges, B. Viana, and G. P. Aka, "Z-scan measurements of the nonlinear refractive indices of novel Yb-doped laser crystal hosts," Appl. Phys. B **80**, 199-201 (2005).

[17] M. Tokurakawa, A. Shirakawa, K. Ueda, H. Yagi, M. Noriyuki, T. Yanagitani and A. A. Kaminskii, "Diode-pumped ultrashort-pulse generation based on Yb^{3+}:Sc_2O_3 and Yb^{3+}:Y_2O_3 ceramic multi-gain-media oscillator," Opt. Express **17**, 3353-3361 (2009).

[18] A. Major, R. Cisek and V. Barzda, "Femtosecond Yb:$KGd(WO_4)_2$ laser oscillator pumped by a high power fiber-coupled diode laser module," Opt. Express **14**, 12163-12168 (2006).

[19] A. Major, J. S. Aitchison, P. W. E. Smith, N. Langford, and A. I. Ferguson, "Efficient Raman shifting of high-energy picosecond pulses into the eye-safe 1.5 μm spectral region using a $KGd(WO_4)_2$ crystal," Opt. Lett. **30**, 421-423 (2005).

[20] H. Liu, J. Nees, and G. Mourou, "Diode-pumped Kerr-lens mode-locked Yb:$KY(WO_4)_2$ laser," Opt. Lett. **26**, 1723-1725 (2001).

[21] A. Yoshida, A. Schmidt, H. Zhang, J. Wang, J. Liu, C. Fiebig, K. Paschke, G. Erbert, V. Petrov, and U. Griebner, "42-fs diode-pumped Yb:$Ca_4YO(BO_3)_3$ oscillator," Opt. Express **23**, 24325-24330 (2010).

[22] M. Tokurakawa, A. Shirakawa, K. Ueda, H. Yagi, S. Hosokawa, T. Yanagitani, and A. A. Kaminskii, "Diode-pumped 65 fs Kerr-lens mode-locked Yb^{3+}:Lu_2O_3 and nondoped Y_2O_3 combined ceramic laser," Opt. Lett. **33**, 1380–1382 (2008).

[23] A. A. Lagatsky, A. R. Sarmani, C. T. A. Brown, W. Sibbett, V. E. Kisel, A. G. Selivanov, I. A. Denisov, A. E. Troshin, K. V. Yumashev, N. V. Kuleshov, V. N. Matrosov, T. A. Matrosova, and M. I. Kupchenko, "Yb^{3+}-doped YVO_4 crystal for efficient Kerr-lens mode locking in solid-state lasers," Opt. Lett. **30**, 3234-3236 (2005).

[24] A. Agnesi, A. Greborio, F. Pirzio, G. Reali, J. Aus der Au, and A. Guandalini, "40-fs Yb^{3+}:$CaGdAlO_4$ laser pumped by a single-mode 350-mW laser diode" Opt. Express. **20**, 10077-10082 (2012).

[25] Y. Zaouter, J. Didierjean, F. Balembois, G. Lucas Leclin, F. Druon, P. Georges, J. Petit, P. Goldner, and B. Viana, "47-fs diode-pumped Yb^{3+}:$CaGdAlO_4$ laser," Opt. Lett. **31**, 119-121 (2006).

[26] M. Tokurakawa, H. Kurokawa, Ae. Shirakawa, K. Ueda, H. Yagi, T. Yanagitani, and A. A. Kaminskii, "Continuous-wave and mode-locked lasers on the base of partially disordered crystalline Yb^{3+}:$\{YGd_2\}[Sc_2](Al_2Ga)O_{12}$ ceramics," Opt. Express. **18**, 4390-4395 (2010).

[27] G. Machinet, P. Sevillano, F. Guichard, R. Dubrasquet, P. Camy, J.-L. Doualan, R. Moncorgé, P. Georges, F. Druon, D. Descamps, and E. Cormier, "High-brightness fiber laser-pumped 68 fs–2.3 W Kerr-lens mode-locked Yb:CaF_2 oscillator," Opt. Lett. **38**, 4008-4010 (2013).

[28] A. Greborio, A. Guandalini, and J. Aus der Au, "Sub-100 fs pulses with 12.5 W from Yb:CALGO based oscillators," *Solid State Lasers XXI: Technology and Devices,* in SPIE Photonics West 2012, paper 8235-11.

[29] A. Diebold, F. Emaury, C. Schriber, M. Golling, C. J. Saraceno, T. Südmeyer, and U. Keller, "SESAM mode-locked Yb:$CaGdAlO_4$ thin disk laser with 62 fs pulse generation," Opt. Lett. **38**, 3842-3845 (2013).

Chapter 6

Megawatt peak power level sub-100 fs Yb:KGW oscillators

Over the past decade there has been significant effort devoted to the development of ultrashort pulse lasers with high peak powers [1]. Of particular interest there were laser oscillators that could deliver Megawatt peak powers with sub-100 fs pulses [2,3]. In the work presented in Chapter 5, I have demonstrated 67 fs pulses with 3 W of average output power at a repetition rate of 77 MHz from an Yb:KGW bulk oscillator [4]. The enhanced performance of this laser resulted from the KLAS mode locking approach which combined the fast saturable absorber-like action of Kerr-lens mode locking (KLM) with the self-starting operation of a SESAM. This laser system forms an excellent platform to explore its potential in scaling of the peak power through the pulse energy at lower repetition rates. In this Chapter, I report on the generation of sub-100 fs pulses with MW peak power level directly from the extended cavity Yb:KGW bulk oscillators operated at either 36 MHz or 18 MHz.

6.1 Extended cavity oscillators

In a mode-locked laser oscillator, there is only one pulse that oscillates in the cavity. The peak power of the pulse can be expressed as the following equation:

$$P_{peak} = \frac{E_p}{\tau_p} = \frac{P_{ave}}{\tau_p f}, \tag{6-1}$$

where E_p is the pulse energy, τ_p is the pulse duration, P_{ave} is the average output power and f is the repetition rate of the pulse train. It is obvious that the peak power can be scaled by 1) increasing the average output power, 2) reducing the pulse duration or 3) lowering the repetition rate.

Owing to their ability to produce sub-10 fs pulses, Megawatt peak power has been reached by Ti:Sapphire lasers almost two decades ago [5-7]. However, it remained very challenging for the crystalline Yb-ion based diode-pumped lasers because of their relatively narrow gain bandwidths and hence relatively long pulse duration. On the other hand, performance of a broadband gain medium like Yb:glass was limited by its poor thermal properties. Therefore, there was a trade-off between the increase of the average output power and the reduction of the pulse duration for the Yb-ion based lasers. This situation changed only very recently with the development of a broadband Yb:CALGO laser crystal with greatly improved thermal conductivity [8], which was used with a semiconductor saturable absorber mirror (SESAM) mode locking to produce 94 fs pulses with 1.6 MW of peak power and 62 fs pulses with 1.1 MW from bulk [9] and thin-disk [10] oscillator configurations, respectively.

An alternative approach to scale the peak power is through lowering the repetition rate *f*, which can be expressed as:

$$f = \frac{c}{2L}, \tag{6-2}$$

where *c* is the speed of light and *L* is the length of a cavity. It follows from equation (6-2) that the repetition rate can be lowered by extending the length of the cavity. The extended cavity oscillators can be straightforwardly implemented by incorporating pure optical components such as intracavity Herriott-type multipass cells (MPCs) and 1:1 imaging telescopes [11-14], which are schematically depicted in Fig.6.1.

Generally, both configurations contain two concave mirrors. In a Herriott-type MPC, the input beam undergoes multiple bounces between the two concave mirrors. Under certain design conditions, the output beam returns back to the entrance on the mirror. More importantly, the q parameter (Appendix B), which contains the information of a Gaussian beam including its radius and radius of curvature of the wavefront, is invariant between the input and output beams. This allows the MPC to be inserted conveniently at any position in a cavity without changing the stability region of the cavity. This is critically important for pure KLM lasers because they are usually operated at the edge of a stability region, a slight change of which may make the KLM difficult to start.

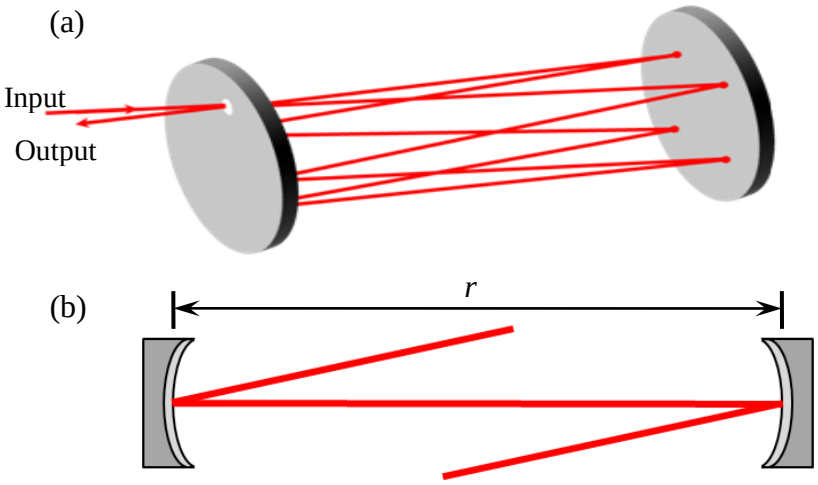

Fig. 6.1. Schematic configuration of (a) a simple Herriott-type multipass cell, and (b) a 1:1 imaging telescope.

A 1:1 imaging telescope, on the other hand, uses simple optics to extend the length of a cavity. In such configuration, two concave mirrors with the same radii of curvature *r* are placed at a distance equal to *r*, resulting in a total length of 4*r* added to the cavity in a single round-trip. Like the MPC, the 1:1 imaging telescope can also be inserted at any position in the cavity because the q parameter of the input beam can be preserved as it passes through.

At present, there is still a trade-off between the pulse duration and the peak power (or pulse energy) for the extended cavity oscillators due to the increased influence of the nonlinear effects at high peak power levels. For example, pulses with 2.3 MW peak power (1 μJ energy) have been delivered from a 10 MHz Yb:KYW bulk oscillator [15]. The pulse duration, however, was limited to 430 fs. Similarly, pulses with 1.3 MW peak power and 323 fs duration were generated from a 23.7 MHz Yb:CALGO bulk oscillator [9]. On the other hand, short pulses with 145 fs duration but at a reduced peak power of 0.16 MW (24 nJ energy) were demonstrated directly from a 27 MHz Yb:CALGO bulk oscillator [16]. In work presented in this Chapter, I developed an extended cavity Yb:KGW bulk oscillator that could reach the MW peak power level and maintain a pulse duration of less than 100 fs. This laser was based on KLAS mode locking presented in Chapter 5.

6.2 Experimental setup

The experiments were carried out with a 1.5 at.%-doped Yb:KGW crystal slab (Eksma). The 5-mm-long and 1.2-mm-thick slab was antireflection coated and cut for beam propagation along the N_g-axis. The excitation was provided by a fiber-coupled laser diode, which offered an unpolarized pump mode with a maximum power of 30 W at 980 nm. The pump mode was launched into the crystal through a pair of achromatic doublets, forming a mode waist of 300 μm at the center of the crystal. The laser cavity setup is schematically depicted in Fig. 6.2. Three Gires–Tournois interferometer (GTI) mirrors (Layertec GmbH) with different negative group velocity dispersions (GVD) of -250 fs^2, -550 fs^2 and -1300 fs^2 were combined, providing a variable round-trip dispersion ranging from -3400 fs^2 to -5200 fs^2. All high reflection (HR) coated cavity mirrors were designed to exhibit low group velocity dispersion (GVD) at the laser wavelength (Laseroptik GmbH). A SESAM with 2% modulation depth and 70 μJ/cm^2 fluence saturation was used to assist in the initiation of the mode locking. The SESAM was placed on a micrometer driven translation stage. Adjusting the distance between the SESAM and R3 mirror allowed for continuous control of the cavity mode size inside the crystal.

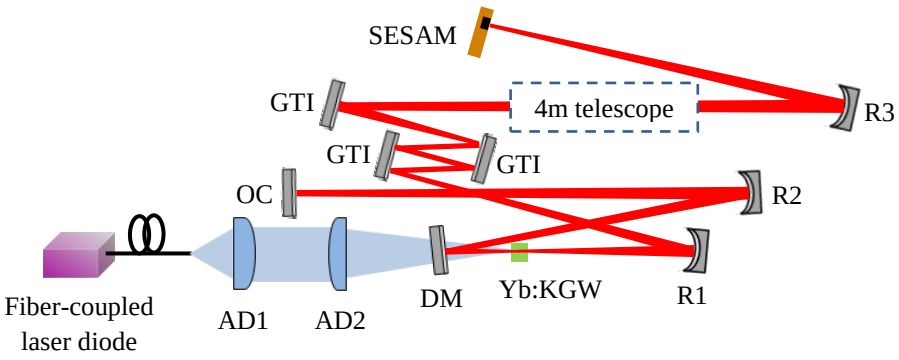

Fig. 6.2. Schematic layout of a laser cavity operated at low repetition rates. AD1 and AD2 are the achromatic doublets with focal lengths of 50 mm and 150 mm, respectively. DM is the dichroic mirror coated for high transmission (>95%) at pump wavelength and high reflection (>99.9%) in the 1020-1200 nm region. R1, R2 and R3 are the concave mirrors with radii of curvature of 600 mm, 600 mm and 750 mm, respectively. GTI is the Gires-Tournois interferometer mirror. OC is the output coupler. The 4 m telescope was composed of two concave mirrors with radii of curvature of 2 m and a folding plane HR mirror.

6.3 Results and discussion

6.3.1 Comparison of thermal lens and Kerr lens

To optimize the KLM as well as the spatial matching between the pump and cavity modes for efficient lasing, we estimated the strength of the thermal and Kerr lenses, which are the two main factors that influence the focusing of a cavity mode inside the crystal. The strength of the thermal lens was determined experimentally by measuring the beam size variation of the cavity mode away from the output coupler and then modeling it with the ABCD matrix analysis (Appendix B). Due to the anisotropic thermal properties of the Yb:KGW crystals, the thermal lens was estimated to be 10-15 diopters at the maximum pump power, depending on the measured directions (along the N_m-axis or N_p-axis). The relatively large cavity mode size inside the Kerr medium resulted in a lowered strength of the Kerr lens, which can be estimated through the following equation [17]:

$$D = \frac{4n_2 L_c I_p}{w^2}. \tag{6-3}$$

Using the following parameters: the nonlinear index of refraction n_2=20 ×10^{-16} cm^2/W [18], the crystal length L_c=5 mm, the pulse peak intensity I_p=15 GW/cm^2, and the cavity mode size w=150 μm, the strength of the Kerr lens was calculated to be 27 diopters. Since the Kerr lens is about twice stronger than the thermal lens, this illustrates that it is an important factor in consideration of the soft gain aperturing and mode matching.

6.3.2 The 36 MHz cavity

The initially designed cavity (without intracavity telescopes) had a round-trip length of 8 m, leading to a repetition rate of 36 MHz. At low pump power levels, the cavity performed with degraded lasing efficiency because the pump power dependent thermal lensing was not strong enough to focus the cavity mode for efficient mode matching in the crystal. The mode locking was initiated by the SESAM and the Kerr lensing was optimized at the maximum pump power level, where the thermal lens was treated as a parasitic factor that exhibited a constant value. In the optimum KLAS mode locking regime, pulses with 78 fs duration (assuming a *sech*^{2} temporal shape) and 1.8 W of average output power were directly generated from the oscillator. The autocorrelation

trace of the pulses was acquired using a commercial long range (200 ps) autocorrelator (Femtochrome, FR-103XL) and is shown in Fig. 6.3 (a). Considering the repetition rate of 36 MHz, the pulse energy of 50 nJ and peak power of 0.65 MW were obtained. The transmission of the output coupler was 10%, which indicated 0.5 μJ of intracavity pulse energy circulated in the oscillator. For optimizing the GVD at such an energy level, two GTI mirrors with -250 fs^2 and -550 fs^2 dispersions were placed for two bounces in each single trip, and an HR mirror with close to zero dispersion was placed instead of the third GTI mirror, allowing for a total round-trip dispersion of -3200 fs^2 to be compensated. The corresponding emission spectrum was centered at 1032 nm with a FWHM of 15 nm (Fig. 6.3 (b)), yielding a time-bandwidth product of 0.32. The laser's output radiation was polarized along the N_m-axis.

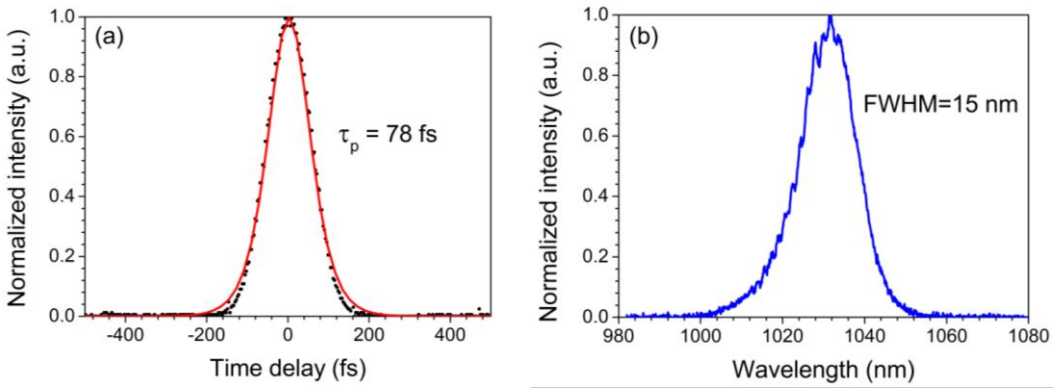

Fig. 6.3. The autocorrelation trace of the pulses obtained from the 36 MHz oscillator with fitting assuming a *sech*^{2} temporal profile (a), and the corresponding emission spectrum (b).

The laser optimized for the KLAS mode locking could be operated at higher intracavity pulse energy levels at the cost of pulse duration as more GVD was introduced. Fig. 6.4 shows the output power and the pulse duration at different compensated GVD levels. It should be noted that all of these results were obtained at the highest pump power of 30 W. As the round-trip negative dispersion of 5200 fs^2 was added into the cavity, we obtained pulses with an average output power of 2.2 W, which corresponds to a pulse energy of 60 nJ. The pulse duration at this level of energy was 100 fs, resulting in a slightly reduced peak power of 0.61 MW.

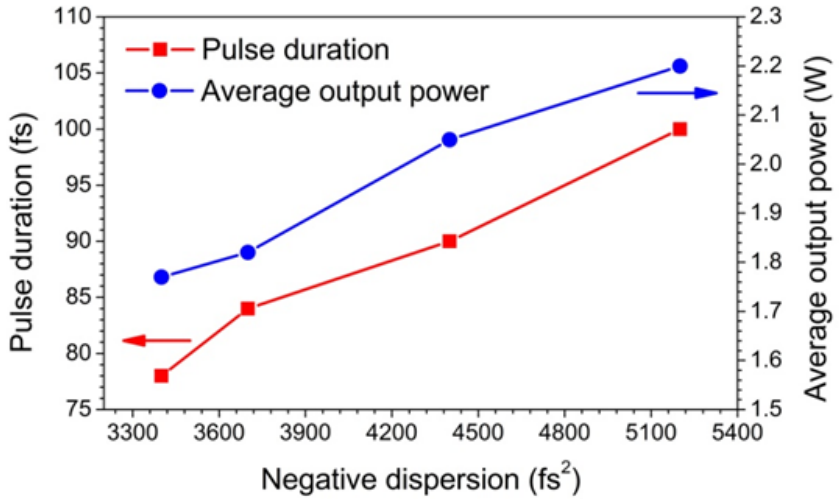

Fig. 6.4. Pulse duration and average output power obtained from the 36 MHz oscillator as a function of the compensated negative dispersion.

In order to understand the effect of Kerr lensing on stabilization of the single-pulsed mode locking, we studied the mode locking regimes with different cavity mode sizes inside the gain medium by translating the SESAM. As the distance between the SESAM and the concave mirror R3 was increased, the cavity mode size inside the crystal was decreased, allowing for a better spatial mode matching and therefore increased output power. From the point of view of self-amplitude modulation (SAM), however, the decrease of the cavity mode size reduced its gain aperturing effect, therefore resulting in lower effective modulation depth. As a consequence, the laser started suffering from the multiple-pulse instability. At the same time, the spectral bandwidth experienced a significant narrowing. For example, as the SESAM was translated around 4 mm away from the optimum position for Kerr lensing, the double-pulsed mode locking regime was observed. The output power increased to 2.5 W (which corresponds to 70 nJ of pulse energy), and the emission spectrum was narrowed to 13 nm. Further translation of the SESAM (about 4 mm) led to the increase of the output power to 3.3 W (91 nJ of pulse energy). In this case the laser operated in multiple-pulse regime with 7 nm of spectral bandwidth. At this point, the mode locking was believed to be purely dominated by the SESAM, since the cavity mode size was very close to the pump mode size when 10 diopters of thermal lensing was taken into account. As the pump power was decreased, single pulses could be generated without broadening of the spectrum. Similar to our

previous work [4], no pure KLM was achieved when the SESAM was replaced with an HR mirror. This supports the fact that in our case mode locking in the sub-100 fs regime is achieved and sustained only by the dual action of the SESAM and the KLM.

6.3.3 The 18 MHz cavity

In order to reduce the repetition rate, a 4 m long 1:1 imaging telescope was inserted into the cavity. As a result the cavity was lengthened to 16 m, which allowed generation of a pulse train at a repetition rate of 18 MHz. Since more mirrors were added, the optimized value of negative dispersion was increased to 3700 fs^2. At the maximum pump power, the oscillator optimized for the KLAS mode locking generated 80 fs pulses at an average output power of 1 W. The corresponding pulse energy was 55 nJ and the intracavity pulse energy was 0.55 μJ, which was close to the one obtained with the 36 MHz oscillator. To extract more energy from the cavity, we used an output coupler with higher transmission of 15%. The average output power and the pulse energy were enhanced to 1.5 W and 83 nJ, respectively. The obtained pulses showed a slightly longer duration of 85 fs (Fig. 6.5 (a)). The 14 nm of spectral bandwidth (see Fig. 6.5 (b)) resulted in almost transform-limited time-bandwidth product of 0.33. At this point, the corresponding peak power as high as 1 MW was reached.

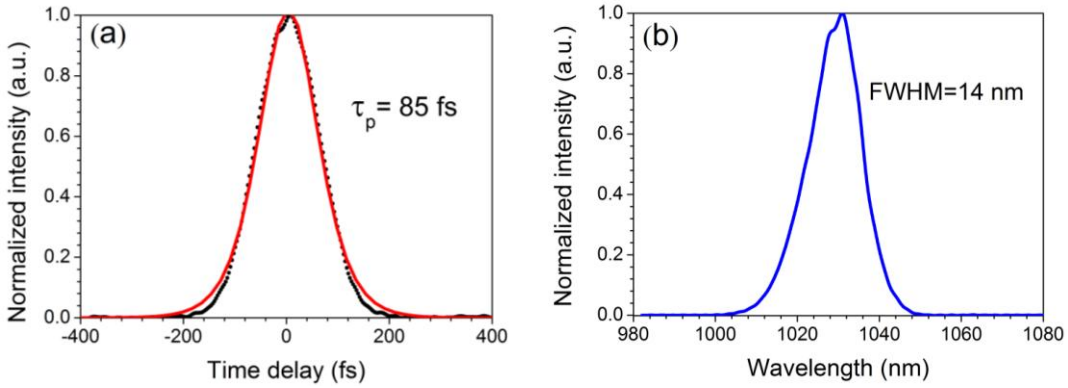

Fig. 6.5. The autocorrelation trace of the pulses obtained from the 18 MHz oscillator with 15% output coupling. The trace is fitted assuming a *sech*^{2} temporal profile. (b) The corresponding emission spectrum.

6.3.4 Comparison with previous results

As a comparison, we summarized the previously reported laser performance from the extended-cavity Yb-ion laser oscillators in Fig. 6.6 [9, 13-16, 19-27]. These laser oscillators were usually operated at repetition rates ranging from 10 MHz to 40 MHz. However, pulses with sub-100 fs duration have never been delivered directly from the oscillator. The Yb:CALGO crystals with broad spectral bandwidth seem quite promising to reach this goal, allowing the generation of pulses with 145 fs duration directly from the oscillator and 93 fs duration after external compression [16]. Nonetheless, such short pulse duration was obtained at the cost of much lower pulse energy and peak power, which were limited to 17 nJ and 180 kW. In this work, sub-100 fs pulses were generated directly from the oscillator. Moreover, the peak power increased by more than 5 times.

Another comparison can be made with the thin-disk oscillators which, in many cases, were operated at similar repetition rates with high peak powers. In most cases, however, the pulses delivered from such lasers suffered from the long duration of >200 fs. Moreover, despite the higher peak power that can be reached from the thin-disk oscillators, much higher pump power is needed. For example, producing 1 MW of peak power required only 30 W of pump power in the extended cavity Yb:KGW bulk oscillator presented in this Chapter, whereas about 140 W of pump power was needed for a Yb:KLuW thin-disk oscillator [22].

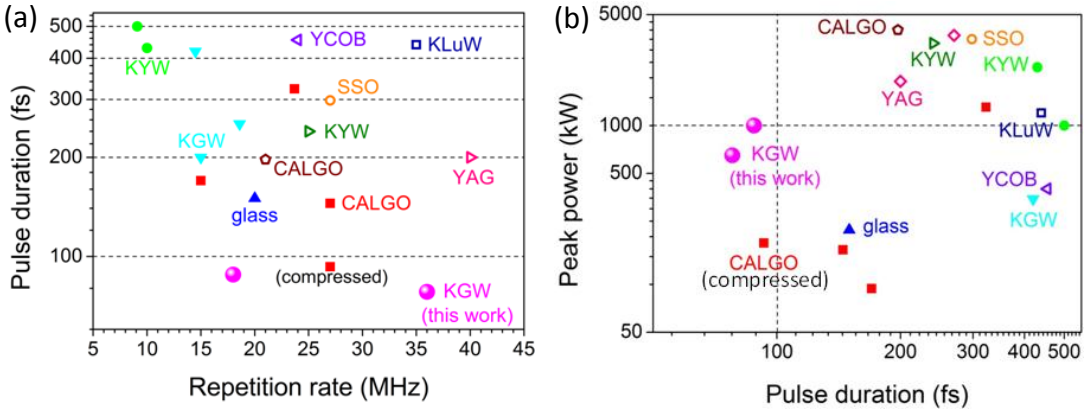

Fig. 6.6. Previously reported laser performance of the extended cavity bulk and thin-disk oscillators. (a) The pulse duration vs. the repetition rate. (b) The peak power vs. the pulse duration. The solid symbols represent the bulk oscillators and the hollow symbols represent the thin-disk oscillators.

Considering only sub-100 fs regime with Megawatt peak powers (regardless of the repetition rate), recently Yb:CALGO bulk and thin-disk oscillators generated 94 fs pulses with 1.6 MW of peak power [9] and 62 fs pulses with 1.1 MW [10], respectively. The former oscillator required >62 W and the later >71 W of pump power. As can be seen, our approach allows us to reach similar operating regime with more than twice lower amount of pump power which can be explained in part by the high gain of the used Yb:KGW crystal. In this case it also can be instructive to define a simple figure of merit, peak-to-pump power efficiency, which shows how many kWs of peak power can be generated per each Watt of the used pump power and therefore has the units of kW/W. This figure of merit is more universal than the optical-to-optical efficiency because it also takes into account the duration of the generated pulses. The Yb:CALGO bulk [9] and thin-disk [10] oscillators have 26.4 kW/W and 15.3 kW/W peak-to-pump power efficiencies, respectively, as compared to the higher efficiency of 33.3 kW/W obtained in this work. We believe that further optimization of the pulse duration and power scaling of the broadband Yb-ion based oscillators can result in multi-MW peak power laser systems in the sub-100 fs regime.

6.4 Conclusion

In conclusion, we have demonstrated the generation of high peak power sub-100 fs pulses from the extended cavity Yb:KGW bulk oscillators. Pulses with 78 fs duration and 0.65 MW peak power were delivered at a repetition rate of 36 MHz. At a lower repetition rate of 18 MHz, 85 fs pulses with peak power as high as 1 MW were generated. To the best of our knowledge, this is the first demonstration of sub-100 fs pulses from the extended cavity Yb-ion based oscillators.

References

[1] W. Sibbett, A. A. Lagatsky and C. T. A. Brown, "The development and application of femtosecond laser systems," Opt. Express **20**, 6989-7001 (2012).

[2] T. Sudmeyer, S. V. Marchese, S. Hashimoto, C. R. E. Baer, G. Gingras, B. Witzel, and U. Keller, "Femtosecond laser oscillators for high-field science," Nature Photon. **2**, 599-604 (2008).

[3] T. Südmeyer, C. Kränkel, C. R. E. Baer, O. H. Heckl, C. J. Saraceno, M. Golling, R. Peters, K. Petermann, G. Huber, U. Keller, "High-power ultrafast thin disk laser oscillators and their potential for sub-100-femtosecond pulse operation," Appl. Phys. B **97**, 281-295 (2009).

[4] H. Zhao, and A. Major, "Powerful 67 fs Kerr-lens mode-locked prismless Yb:KGW oscillator," Opt. Express **21**, 31846-31851 (2013).

[5] L. Xu, G. Tempea, A. Poppe, M. Lenzner, Ch. Spielmann, F. Krausz, A. Stingl, K. Ferencz, "High-power sub-10-fs Ti:sapphire oscillators," Appl. Phys. B **65**, 151-159 (1997).

[6] S. Naumov, A. Fernandez, R. Graf, P. Dombi, F. Krausz, and A. Apolonski, "Approaching the microjoule frontier with femtosecond laser oscillators," New J. Phys. **7**, 216 (2005).

[7] S. Dewald, T. Lang, C. D. Schröter, R. Moshammer, J. Ullrich, M. Siegel, and U. Morgner, "Ionization of noble gases with pulses directly from a laser oscillator," Opt. Lett. **31**, 2072-2074 (2006).

[8] J. Petit, P. Goldner and B. Viana, "Laser emission with low quantum defect in Yb:$CaGdAlO_4$," Opt. Lett. **30**, 1345-1347 (2005).

[9] A. Greborio, A. Guandalini, and J. Aus der Au, "Sub-100 fs pulses with 12.5 W from Yb:CALGO based oscillators," Solid State Lasers XXI: Technology and Devices, in SPIE Photonics West 2012, paper 8235-11.

[10] A. Diebold, F. Emaury, C. Schriber, M. Golling, C. J. Saraceno, T. Südmeyer, and U. Keller, "SESAM mode-locked Yb:$CaGdAlO_4$ thin disk laser with 62 fs pulse generation," Opt. Lett. **38**, 3842-3845 (2013).

[11] R. Herriott, H. Kogelnik, and R. Kompfner, "Off-axis paths in spherical mirror interferometers," Appl. Opt.**3**, 523-526 (1964).

[12] A. Sennaroglu, and J. G. Fujimoto, "Design criteria for Herriott-type multi-pass cavities for ultrashort pulse lasers," Opt. Express **11**, 1106-1113 (2003).

[13] A. Major, V. Barzda, P. A. E. Piunno, S. Musikhin, and U. J. Krull, "An extended cavity diode-pumped femtosecond Yb:KGW laser for applications in optical DNA sensor technology based on fluorescence lifetime measurements," Opt. Express **14**, 5285-5294 (2006).

[14] A. Major, R. Cisek, D. Sandkuijl, and V. Barzda, "Femtosecond Yb:$KGd(WO_4)_2$ laser with >100 nJ of pulse energy," Laser Phys. Lett. **6**, 272–274 (2009).

[15] E. P. Mottay, and C. Hönninger, "MicroJoule level diode-pumped femtosecond oscillator," Commercial and biomedical applications of ultrafast lasers VII, Proc. SPIE **6460**, San Jose, USA, 64600I (2007).

[16] D. N. Papadopoulos, F. Druon, J. Boudeile, I. Martial, M. Hanna, P. Georges, P. O. Petit, P. Goldner, and B. Viana, "Low-repetition-rate femtosecond operation in extended-cavity mode-locked Yb:CALGO laser," Opt. Lett. **34**, 196-198 (2009).

[17] K. X. Liu, C. J. Flood, D. R. Walker, and H. M. van Driel, "Kerr lens mode locking of a diode-pumped Nd:YAG laser," Opt. Lett. **17**, 1361-1363 (1992).

[18] A. Major, I. Nikolakakos, J.S. Aitchison, A.I. Ferguson, N. Langford, P.W.E. Smith, "Characterization of the nonlinear refractive index of the laser crystal Yb:$KGd(WO_4)_2$", Appl. Phys. B **77**, 433-436 (2003).

[19] C. Hoenninger, A. Courjaud, P. Rigail, E. Mottay, M. Delaigue, N. Dguil-Robin, J. Limpert, I. Manek-Hoenninger, and F. Salin, "0.5µJ Diode Pumped Femtosecond Laser Oscillator at 9 MHz," in Advanced Solid-State Photonics, Vienna 2008, ME2.

[20] K. E. Sheetz, E. E. Hoover, R. Carriles, D. Kleinfeld, and J. A. Squier, "Advancing multifocal nonlinear microscopy: development and application of a novel multibeam Yb:$KGd(WO_4)_2$ oscillator," Opt. Express **16**, 17574-17584 (2008).

[21] F. Hoos, S. Pricking, and H. Giessen, "Compact portable 20 MHz solid-state femtosecond white light-laser," Opt. Express **14**, 10913-10920 (2006).

[22] G. Palmer, M. Schultze, M. Siegel, M. Emons, U. Bünting, and U. Morgner, "Passively mode-locked Yb:$KLu(WO_4)_2$ thin-disk oscillator operated in the positive and negative dispersion regime," Opt. Lett. **33**, 1608-1610 (2008).

[23] F. Brunner, T. Südmeyer, E. Innerhofer, F. Morier-Genoud, R. Paschotta, V. E. Kisel, V. G. Shcherbitsky, N. V. Kuleshov, J. Gao, K. Contag, A. Giesen, and U. Keller, "240-fs pulses with 22-W average power from a mode-locked thin-disk Yb:$KY(WO_4)_2$ laser," Opt. Lett. **27**, 1162-1164 (2002).

[24] K. S. Wentsch, L. Zheng, J. Xu, M. A. Ahmed, and T. Graf, "Passively mode-locked Yb^{3+}:$ScSiO_5$ thin-disk laser," Opt. Lett. **37**, 4750-4752 (2012).

[25] O. H. Heckl, C. Kränkel, C. R. E. Baer, C. J. Saraceno, T. Südmeyer, K. Petermann, G. Huber, and U. Keller, "Continuous-wave and modelocked Yb:YCOB thin disk laser: first demonstration and future prospects," Opt. Express **18**, 19201-19208 (2010).

[26] O. Pronin, J. Brons, C. Grasse, V. Pervak, G. Boehm, M.-C. Amann, V. L. Kalashnikov, A. Apolonski, and F. Krausz, "High-power 200 fs Kerr-lens mode-locked Yb:YAG thin-disk oscillator," Opt. Lett. **36**, 4746-4748 (2011).

[27] S. Ricaud, A. Jaffres, K. Wentsch, A. Suganuma, B. Viana, P. Loiseau, B. Weichelt, M. Abdou-Ahmed, A. Voss, T. Graf, D. Rytz, C. Hönninger, E. Mottay, P. Georges, and F. Druon, "Femtosecond Yb:$CaGdAlO_4$ thin-disk oscillator," Opt. Lett. **37**, 3984-3986 (2012).

Chapter 7

Ultrafast OPOs pumped at 1.04 μm

Optical parametric oscillators (OPO) are widespread and versatile sources for generating wavelength-tunable coherent continuous or pulsed radiation in a broad spectral range that spans from the infrared to the ultraviolet [1]. When pumped by Yb:KGW lasers with 1 μm radiation, a continuous tuning of near-IR wavelength can be obtained. Such laser sources are especially useful for many biological and medical applications. In this chapter, the feasibility of developing such laser sources are demonstrated through a thorough theoretical analysis of the near-IR properties of two promising periodically poled OPO materials: $KTiOPO_4$ (PPKTP) and stoichiometric MgO-doped $LiTaO_3$ (MgO:PPSLT).

7.1 Optical parametric oscillators

7.1.1 Induced nonlinear polarization

The interaction of radiation with a medium is manifested through the induced electric dipoles, each of which served as a contributor to a new radiation. Macroscopically, this effect is described by the induced polarization (which is defined as the dipole moment density):

$$P(t) = \varepsilon_0 \chi^{(1)} E(t) + \varepsilon_0 \chi^{(2)} E(t)^2 + \varepsilon_0 \sum_{n=3}^{\infty} \chi^{(n)} E(t)^n \,, \tag{7-1}$$

where ε_0 is the vacuum permittivity, $\chi^{(n)}$ is the n-th order susceptibility tensor of the medium and $E(t)$ is the time-dependent electrical field of the light. The first term on the right hand side of the equation is related to the linear response of the medium, while the rest of the terms are related to the nonlinear response. Since the higher orders of $\chi^{(n)}$ ($n \geqslant 2$) are much smaller than $\chi^{(1)}$, only light with high enough intensity (e.g. femtosecond laser) can excite the nonlinear terms, causing a nonlinear response of the polarization to the electrical field of the incident light.

Optical parametric oscillation is a process related to the second order response of the induced polarization. Fig. 7.1 shows a scheme of an optical parametric process as an intense radiation with frequency ω_p propagates through the medium. From the energy point of view, an incident pump photon with energy of $\hbar\omega_p$ is split into two photons with energies of $\hbar\omega_s$ and $\hbar\omega_i$. The resulting two new waves with frequencies ω_s and ω_i are called signal and idler, respectively. The energy conservation condition requires the satisfaction of the relationship $\omega_p=\omega_s+\omega_i$.

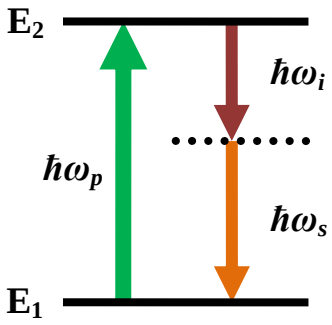

Fig. 7.1. Scheme of an optical parametric process.

7.1.2 Phase matching

If the incident wave and output waves are matched in phase, the incident energy will efficiently flow from it to the output waves; otherwise the energy will flow in an opposite way. In the case of an optical parametric process, the phase mismatch between incident and output waves can be quantified as:

$$\Delta\vec{k} = \vec{k}_p - \vec{k}_s - \vec{k}_i, \tag{7-2}$$

where $\vec{k}_p$, $\vec{k}_s$ and $\vec{k}_i$ are the wave vectors of the pump, signal and idler waves. In a collinear propagation, this equation can be rearranged as:

$$\Delta k = \frac{n_p\omega_p}{c} - \frac{n_s\omega_s}{c} - \frac{n_i\omega_i}{c}, \tag{7-3}$$

where n is the wavelength-dependent refractive index, and c is the speed of light in vacuum. When Δk=0, the phase of the waves are perfectly matched, resulting in the highest conversion efficiency. The conventional method to achieve the phase-matching is to take advantage of the optical birefringence of the crystals, known as birefringent phase-matching (BPM) technique. In this method, the polarization of laser radiation,

incident angle and crystal temperature are adjusted such that the phase velocity mismatch between the interacting waves is compensated. Nonetheless, this approach has some problems and restrictions in practical applications, such as spatial walk-off effect and inconvenient phase-matching temperatures and angles. More importantly, BPM cannot be realized in plenty of nonlinear media with good nonlinear properties.

An alternative way of achieving the phase-matching condition is the so-called quasi-phase-matching (QPM) technique by using periodic stacks of nonlinear crystals that have opposite signs of $\chi^{(2)}$ [2]. These stacks of crystals are called periodically poled crystals, and their structure is schematically shown in Fig. 7.2 (a). By applying a high voltage electric field to the patterned electrodes, the nonlinearity of the ferroelectric crystal is modulated with a period twice of the coherence length of the nonlinear interaction. In QPM technique, all of the interacting waves have the same polarization, resulting in a certain amount of phase mismatch ($\Delta k \neq 0$) in each ferroelectric domain. The phase mismatch would cause the energy to flow back to the pump wave beyond the coherence length if no controls are implemented (red line in Fig. 7.2 (b)). Since in periodically poled crystals the $\chi^{(2)}$ nonlinear coefficient is reversed over a distance that equals to the coherence length, the phase mismatch is compensated in the next domain, resulting in the continuous energy flow from the pump wave into the newly generated signal and idler waves (blue line in Fig. 7.2 (b)). When compared with the BPM, QPM has several advantages:

1) Since all the interacting waves are polarized in the same direction, the effect of spatial walk-off is eliminated;
2) The largest elements on the diagonal of the nonlinear coefficient tensor ($d_{ijk} = \chi^{(2)}_{ijk} / 2$) can be utilized, resulting in a larger conversion efficiency;
3) QPM offers noncritical phase-matching at any wavelength within the transparency region of the material. This enables a very large wavelength tuning range.
4) QPM largely extends the variety of nonlinear crystals that can be used for parametric frequency conversion.

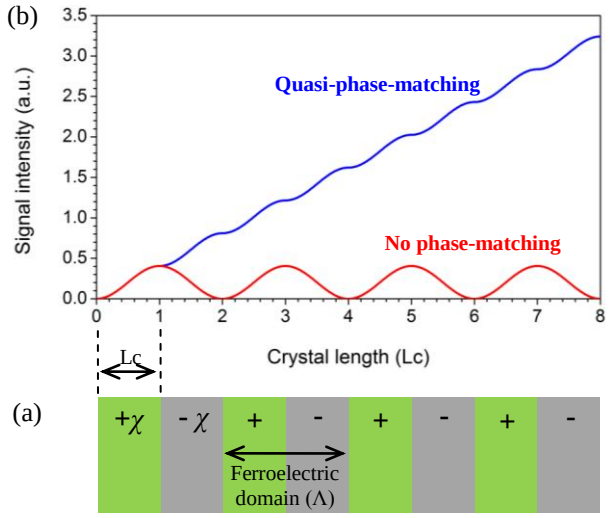

Fig. 7.2. (a) Schematic structure of a periodically poled crystal; (b) the generated wave intensity within eight coherent lengths (Lc) under quasi-phase-matched and non-phase-matched conditions.

7.1.3 Optical parametric oscillators

With optical feedback provided by the mirrors for the parametric process, an OPO system is formed. Under the QPM condition, the signal (idler) wavelength can be tuned by varying the poling period or the temperature of the crystal. The oscillation starts from the randomly generated signal and idler photon pairs in the medium. When the generation of the photon pairs surpasses the loss in the cavity, the signal and idler waves get amplified. For ultrashort pulse pumping as in our case, regime of synchronous pumping scheme is commonly used (Fig. 7.3) [3-4]. In this configuration, the OPO cavity length is designed to match the cavity length of a pumping source such that the signal (idler) pulse produced by the pump pulse could meet the next incoming pump pulse in the nonlinear crystal. Due to the high peak intensity of the pulses, the threshold for a singly resonant oscillation can be easily achieved. Therefore such OPOs usually operate in singly resonant oscillation mode where only signal (or idler) beam is coupled out.

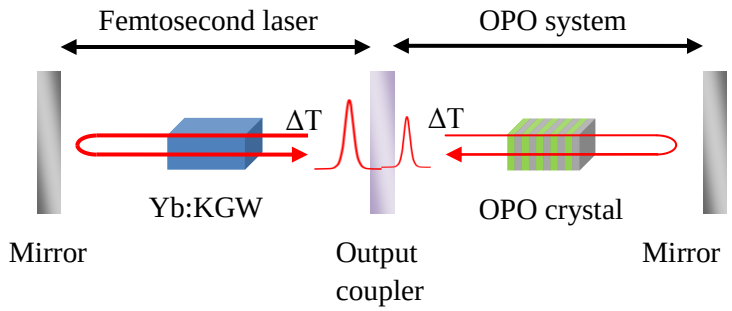

Fig. 7.3. Schematic configuration of an ultrafast OPO system synchronously pumped by an ultrafast Yb:KGW laser.

7.1.4 Dispersion management

For operation on a femtosecond time scale, the dispersive characteristics of the nonlinear crystals become an important factor that need to be considered carefully. As the interacting pulses have very different wavelengths, they will propagate through the crystal with different group velocities. This will lead to the so-called temporal walk-off, which affects the pulse duration and shape. Consequently the effective interaction length in the crystal and the output power are limited by this factor [5]. The group velocity mismatch (GVM) is a quantitative description of the temporal walk-off effect. The GVM can be calculated using the following formula:

$$GVM = \frac{1}{v_i} - \frac{1}{v_j}, \tag{7-4}$$

where v_i and v_j correspond to the group velocities of the two interacting pulses, i.e. pump-idler pulses or pump-signal pulses.

For each single pulse, due to its large spectral bandwidth, different frequency components travel through the medium with different velocities, resulting also in the spreading of the pulse in time domain. This effect can be estimated by the group velocity dispersion (GVD) using the equation:

$$GVD = \frac{\lambda^3}{2\pi c^2}\frac{d^2 n_e(\lambda)}{d\lambda^2}, \tag{7-5}$$

where $n_e(\lambda)$ is the wavelength-dependent extraordinary refractive index of the crystal, and c is the speed of light. Positive GVD in the crystal produces a linear chirp that increases the duration of the output pulses.

7.2 Selection of periodically poled materials

By using the QPM technique, a large variety of materials can be utilized as the frequency converting media. In this work, we mainly concentrate on two promising ones: PPKTP and PPSLT. A comparison of these materials with the commonly used PPcLN (periodically poled congruent $LiNbO_3$) is shown in Table 7.1. Among them, PPcLN has a large effective nonlinear coefficient of 17 pm/V when the $e \rightarrow e+e$ interaction is employed (e represents the extraordinary polarization) [1]. However, PPcLN suffers from some drawbacks that limit its usage in many applications. Firstly, due to its low photorefractive resistance, PPcLN crystals are easily damaged by the high intensity light. This problem can be dealt by either heating the medium to above 100 ℃ or doping the crystal with MgO [6-7]. Secondly, the coercive field, which is used for modulating the nonlinearity of the crystal domains, is quite large. Thus the thickness of the PPcLN or MgO:PPcLN crystals is limited to 0.5 mm.

Table 7.1. Comparison of nonlinear crystals

Material	λ_{trans} **(μm)**	d_{eff} **(pm/V)**	D_{th}	V_{co} **(kV/mm)**	***Ref***
PPcLN	0.35-5.2	17	Low	21	[8-9]
PPKTP	0.35 - 3.5	9.5	High	2	[1,10-11]
MgO:PPSLT	0.27 - 6	11	High	1.7	[12-14]

λ_{trans}: transparent wavelength; d_{eff}: effective nonlinear coefficient ($d_{eff}=2d_{33}/\pi$, where d_{33} is an element in the nonlinear coefficient tensor); D_{th}: photorefractive damage threshold; V_{co}: coercive field.

PPKTP and MgO:PPSLT crystals are considered as two promising substitutions to PPcLN and MgO:PPcLN crystals. Their nonlinear coefficients are twice smaller than that of PPcLN crystal, but they are still much larger than those utilized in birefringent phase matching [10, 13]. Besides, the coercive fields of these two materials are more than ten times lower than that for PPcLN crystal: 2 kV/mm for PPKTP and 1.7 kV/mm for MgO:PPSLT, allowing thicker crystals to be obtained [11,14]. More importantly, PPKTP and MgO:PPSLT have much higher photorefractive damage threshold. High power operation, therefore, can be carried out even at room temperature.

7.3 Theoretical studies of material properties for near-IR OPOs

Before experimentally developing an OPO system based on the materials listed above, a theoretical calculation is necessary to determine the dependence of wavelength tuning on the parameters of the crystals and the cavity, as well as the dispersive characteristics to select a suitable crystal length. Generally, there are mainly four parameters that can be adjusted for wavelength tuning: pump wavelength, cavity length, crystal poling period, and crystal temperature. Since the Yb:KGW lasers have very limited wavelength tunability and the cavity length tuning strongly depends on experimental conditions, our theoretical calculations are mainly focused only on the last two methods.

7.3.1 Phase matching properties

In order to calculate phase-matching ranges of the QPM-based OPO as a function of grating period or temperature, two conditions should be met simultaneously:

$$\frac{1}{\lambda_s}+\frac{1}{\lambda_i}=\frac{1}{\lambda_p}, \tag{7-6}$$

$$\frac{n_e(\lambda_p,T)}{\lambda_p}-\frac{n_e(\lambda_s,T)}{\lambda_s}-\frac{n_e(\lambda_i,T)}{\lambda_i}-\frac{1}{\Lambda(T)}=0 \tag{7-7}$$

The first condition is the energy conservation and the second one is the momentum conservation, which is also called QPM condition. Under the QPM condition, an extra term $1/\Lambda(T)$ related to the phase compensation from the modulated nonlinearity is added when comparing with equation (7-3). In these two equations, the subscript "*s*" represents the signal wave, "*i*" the idler wave and "*p*" the pump wave. λ_s, λ_i and λ_p are the signal, idler and pump wavelengths, respectively. $\Lambda(T)$ is the temperature-dependent grating period of the crystal that takes into account thermal expansion [15-16]. $n_e(\lambda_s,T)$, $n_e(\lambda_i,T)$ and $n_e(\lambda_p,T)$ are the extraordinary refractive indices of the signal, idler and pump waves, respectively. They are calculated from the temperature corrected Sellmeier equations. The detailed Sellmeier equations and $\Lambda(T)$ equations for PPKTP and MgO:PPSLT crystals are described in the Appendix C.

Presented in Fig. 7.4 (a) are the calculated wavelength tuning ranges as a function of grating period for the PPKTP and MgO:PPSLT crystals pumped at 1040 nm. The temperatures used in the calculations are the ones where usually no obvious

photorefractive damage to the crystals is observed. The lower branch of the curve is the signal radiation and the upper branch is the idler radiation. The degeneracy can be observed at the point where the signal wavelength is equal to the idler wavelength, i.e. at 2080 nm. The degeneracy point occurs at 38.24 μm and 31.94 μm for PPKTP and MgO:PPSLT, respectively. It should be noticed that for PPKTP, because of the limited transparency range, the wavelength can be tuned only from 1.480 μm to 3.500 μm, corresponding to the grating period range of 34.84-38.24 μm.

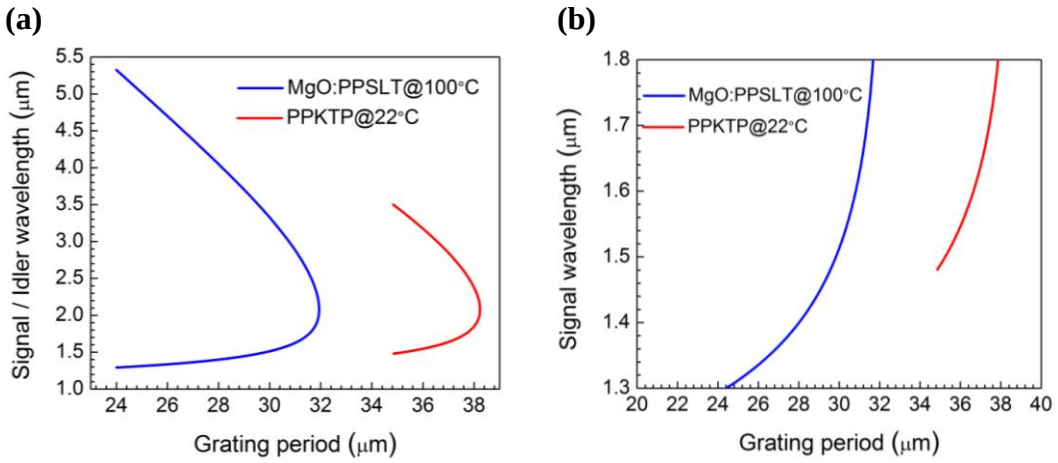

Fig. 7.4. (a) Signal and idler wavelength tuning curves as a function of grating period for MgO:PPSLT and PPKTP crystals. (b) Signal wavelength tuning within 1.3-1.8 μm as a function of grating period for MgO:PPSLT and PPKTP crystals. The pump wavelength is 1040 nm.

7.3.2 Wavelength tuning characteristics

A closer view of the wavelength tuning in the 1.3-1.8 μm range, which is attractive for biomedical applications, is presented in Fig. 7.4 (b). It shows the signal tuning in this range by changing the grating periods. It can be seen that different grating periods should be chosen for generating the desired signal wavelength. For example, to generate 1.55 μm signal wavelength the grating periods of 35.24 μm for PPKTP and 29.84 μm for MgO:PPSLT should be chosen. It also can be seen that the tuning curve is quite steep, indicating that the change of grating periods is a coarse way of wavelength tuning. However, this can be compensated by the finer temperature tuning.

Temperature tuning of the signal wavelength in the 1.3-1.8 μm range for different grating periods in MgO:PPSLT and PPKTP are displayed in Fig. 7.5 and Fig. 7.6. By changing the temperature between 20 ℃ and 200 ℃, continuous tuning over tens of nanometers is possible with a single grating. By choosing grating periods that have an overlap in their individual tuning ranges, such as in the grating periods shown in the figures, it is possible to achieve continuous wavelength tunability over a much wider range. It is apparent that the variation of the signal wavelength with the temperature becomes more pronounced as the wavelength gets closer to the degeneracy point. Please note again that the wavelength tuning range of PPKTP is restricted by its transparency range, i.e. absorption of idler at wavelengths longer than 3.5 μm. Therefore, PPKTP is not suitable for generation of signal wavelengths shorter than 1.48 μm.

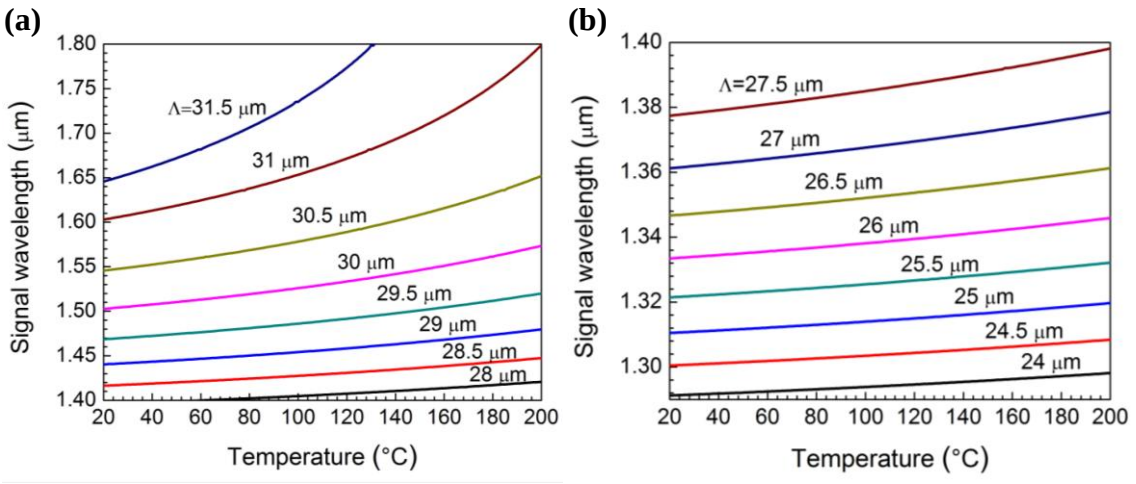

Fig. 7.5. Signal wavelength tuning as a function of temperature for MgO:PPSLT in (a) 1.40 to 1.80 μm range and (b) 1.29-1.4 μm range . The pump wavelength is 1040 nm.

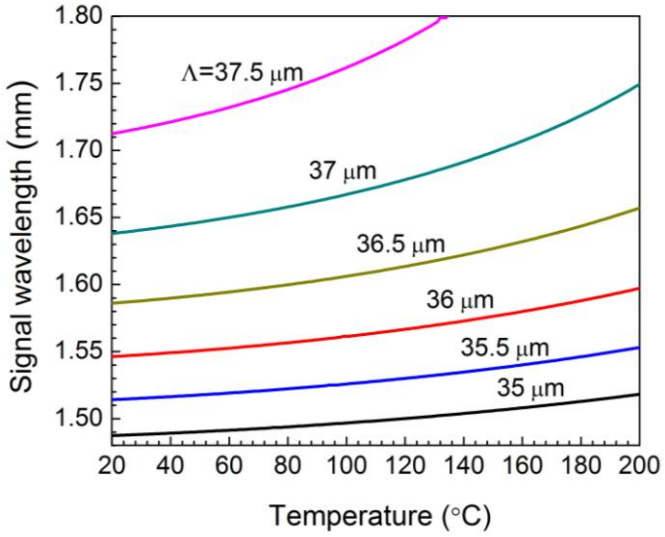

Fig. 7.6. Signal wavelength tuning as a function of temperature for PPKTP in 1.48-1.8 μm range. The pump wavelength is 1040 nm.

It also should be noted that because of the imperfectness of the Sellmeier equation for PPKTP there is a temperature difference of approximately 25 ℃ between the theoretical and experimental values of wavelength tuning [15]. In order to determine the exact temperature shift, a comparison between the theoretical and experimental results was made [17-18]. Since there are no experimental results for the wavelength tuning of PPKTP excited at 1040nm, the closest pump wavelength of 1064 nm from the Nd-doped lasers was selected. The results suggest that the temperature used for the calculation should be 18 ℃ lower than that for the experiment, i.e. if the crystal is set to operate at 50 ℃ in the experiment, then 32 ℃ should be used for calculating the output wavelength. All the calculations for PPKTP listed above introduced this temperature shift for correctness.

7.3.3 Dispersive properties

The GVM data in the near-IR region between the pump (1.040 μm) and signal as well as the pump and idler for PPKTP and MgO:PPSLT are plotted in Fig. 7.7. It can be seen that at the idler wavelength of around 3.2-3.4 μm (which corresponds to the signal wavelength of around 1.55 μm), the GVM between the pump and idler beams equals to zero, which means that both of them travel at the same group velocity. The idler

wavelengths for the zero-GVM point are slightly different. The zero-GVM point results from the non-monotonicity of the group velocity curve as a function of wavelength.

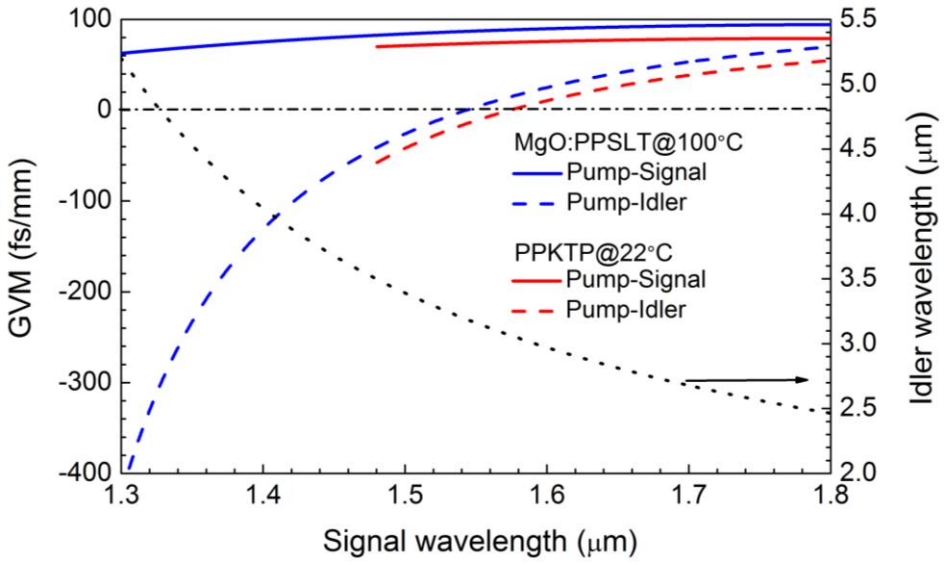

Fig. 7.7. GVM between the pump and signal and the pump and idler for MgO:PPSLT and PPKTP pumped at 1.040 μm. The dotted line indicates the idler wavelength.

The data in Fig. 7.7 can be used to estimate the length of the nonlinear crystal for a particular duration of the pump pulses. The average GVM between the pump and the signal is about 75 fs/mm for PPKTP (for MgO:PPSLT it is about 20% larger). This translates into a temporal delay between the pump and signal of 300 fs (a typical duration of pulses for an Yb-ion laser) after propagation in a 4 mm long crystal. At the same time for PPLN the average GVM between the pump and signal is about 100 fs/mm, thus reducing the crystal length to 3 mm for the same pump pulse duration [8]. In order to restrict the pulse broadening to ~10%, the temporal walk-off between the pump and the signal should be kept at half the initial pump pulse width [4], i.e. in this case a crystal length of ~2 mm should be chosen for both PPKTP and MgO:PPSLT. When pumped by the 70 fs pulses generated from our developed laser oscillator presented in Chapter 5, crystals with ~0.5 mm length should be chosen for PPKTP and MgO:PPSLT and with ~0.3 mm length for PPLN to produce sub-100 fs signal pulses. The interaction length obtained with an excitation source at 800 nm (e.g. Ti:sapphire laser) is even shorter.

The GVD curves for these materials were calculated and shown in Fig. 7.8. It was found that the GVD of MgO:PPSLT is larger than that of PPKTP and they both decrease

with the increase in wavelength. The GVD becomes zero at 1.83 μm for MgO:PPSLT and at 1.80 μm for PPKTP. Intracavity GVD compensation mechanism, such as a prism pair, should be used in the femtosecond OPOs to keep the duration of pulses at a minimum value [19]. Commonly, glasses such as SF10 and SF14 with high dispersion are used for this purpose [5, 20].

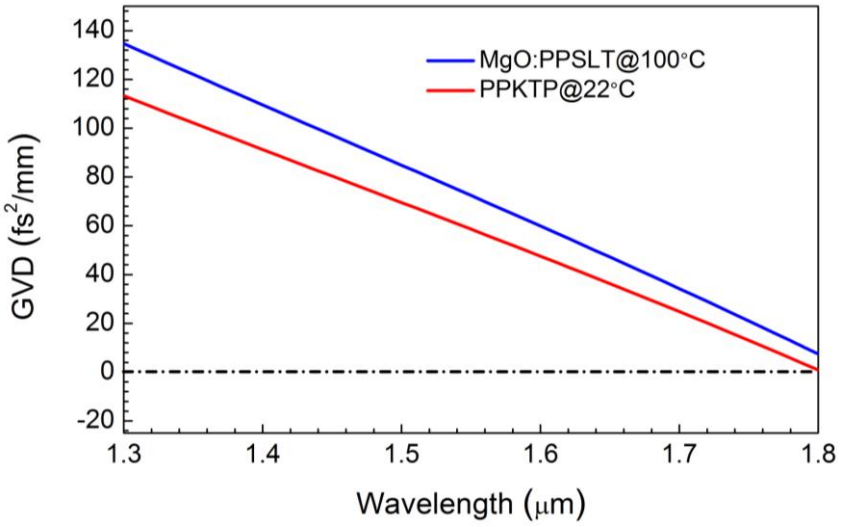

Fig. 7.8. GVD for MgO:PPSLT and PPKTP in the 1.3–1.8 μm wavelength range.

7.4 Conclusion

In conclusion, a detailed analysis of the optical, phase-matching, wavelength tuning, and dispersive properties of PPKTP and MgO:PPSLT materials for generation of near-infrared radiation in the 1.3-6.0 μm range was presented. To the best of our knowledge, this is the first detailed account of PPKTP and MgO:PPSLT crystal properties relevant to the optical parametric interactions in the near-IR. The work also discussed advantages of these two promising periodically poled materials with respect to the more common PPcLN crystal. The results of the presented analysis will provide a thorough reference for the practical design of PPKTP- or MgO:PPSLT-based OPOs pumped by the ultrafast Yb-ion lasers.

References

[1] M. H. Dunn, and M. Ebrahimzadeh, "Parametric Generation of Tunable Light from Continuous-Wave to Femtosecond Pulses," Science **286**, 1513-1517 (1999).

[2] J. A. Armsrong, N. Bloembergen, J. Ducuing, and P. S. Pershan, "Interactions between Light Waves in a Nonlinear Dielectric," Phys. Rev. **127**, 1918-1939 (1962).

[3] Q. Fu, G. Mak, and H. M. van Driel, "High-power, 62-fs infrared optical parametric oscillator synchronously pumped by a 76-MHz Ti:sapphire laser," Opt. Lett. **17**, 1006-1008 (1992).

[4] A. Nebel, C. Fallnich, R. Beigang, and R. Wallenstein, "Noncritically phase-matched continuous-wave mode-locked singly resonant optical parametric oscillator synchronously pumped by a Ti:sapphire laser," J. Opt. Soc. Am. B **10**, 2195-2200 (1993).

[5] C. McGowan, D. T. Reid, Z. E. Penman, M. Ebrahimzadeh, W. Sibbett, and D. H. Jundt, "Femtosecond optical parametric oscillator based on periodically poled lithium niobate," J. Opt. Soc. Am. B **15**, 694-701 (1998).

[6] L. E. Myers, R. C. Eckardt, M. M. Fejer, R. L. Byer, W. R. Bosenberg, and J. W. Pierce, "Quasi-phase-matched optical parametric oscillators in bulk periodically poled $LiNbO_3$," J. Opt. Soc. Am. B **12**, 2102-2116 (1995).

[7] O. Paul, A. Quosig, T. Bauer, M. Nittmann, J. Bartschke, G. Anstett, and J. A. L'huillier, "Temperature-dependent Sellmeier equation in the MIR for the extraordinary refractive index of 5% MgO doped congruent $LiNbO_3$," Appl. Phys. B **86**, 111-115 (2007).

[8] I. T. Lima Jr., V. Kultavewuti, A. Major, "Phasematching properties of congruent MgO-doped and undoped periodically poled $LiNbO_3$ for optical parametric oscillation with ultrafast excitation at 1 μm," Laser Phys. **20**, 270-275 (2010).

[9] J.-P. Meyn1, C. Laue1, R. Knappe, R. Wallenstein, M. M. Fejer, "Fabrication of periodically poled lithium tantalate for UV generation with diode lasers," Appl. Phys. B **73**, 111–114 (2001).

[10] D. R. Weise, U. Ströβner, A. Peters, J. Mlynek, S. Schiller, A. Arie, A. Skliar, G. Rosenman, "Continuous-wave 532-nm-pumped singly resonant optical parametric oscillator with periodically poled $KTiOPO_4$," Opt. Commun. **184**, 329-333 (2000).

[11] T. Kartaloğlu, K. G. Kğprülü, O. Aytür, M. Sundheimer, and W. P. Risk, "Femtosecond optical parametric oscillator based on periodically poled $KTiOPO_4$," Opt. Lett. **23**, 61-63 (1998).

[12] I. Dolev, A. Ganany-Padowicz, O. Gayer, A. Arie, J. Mangin, and G. Gadret, "Linear and nonlinear optical properties of MgO:$LiTaO_3$," Appl. Phys. B **96**, 423-432 (2009).

[13] S. Bahbah, F. Bretenaker, and C. Drag, "Single-frequency quasi-continuous red radiation generated by a green-pumped singly resonant optical parametric oscillator," Opt. Lett. **31**, 1283-1285 (2006).

[14] T. Hatanaka, K. Nakamura, T. Taniuchi, H. Ito, Y. Furukawa, and K. Kitamura, "Quasi-phase-matched optical parametric oscillation with periodically poled stoichiometric $LiTaO_3$," Opt. Lett. **25**, 651-653 (2000).

[15] S. Emanueli and A. Arie, "Temperature-Dependent Dispersion Equations for $KTiOPO_4$ and $KTiOAsO_4$," Appl. Opt. **42**, 6661-6665 (2003).

[16] A. Bruner, D. Eger, M. B. Oron, P. Blau, M. Katz, and S. Ruschin, "Temperature-dependent Sellmeier equation for the refractive index of stoichiometric lithium tantalate," Opt. Lett. **28**, 194-196 (2003).

[17] J. Hellström, V. Pasiskevicius, F. Laurell, and H. Karlsson, "Efficient nanosecond optical parametric oscillators based on periodically poled KTP emitting in the 1.8–2.5-μm spectral region," Opt. Lett. **24**, 1233-1235 (1999).

[18] M. Peltz, U. Bäder, A. Borsutzky, R. Wallenstein, J. Hellström, H. Karlsson, V. Pasiskevicius, and F. Laurell, "Optical parametric oscillators for high pulse energy and high average power operation based on large aperture periodically poled KTP and RTA," Appl. Phys. B **73**, 663-670 (2001).

[19] R. L. Fork, O. E. Martinez, and J. P. Gordon, "Negative dispersion using pairs of prisms," Opt. Lett. **9**, 150-152 (1984).

[20] K. C. Burr, C. L. Tang, M. A. Arbore, and M. M. Fejer, "High-repetition-rate femtosecond optical parametric oscillator based on periodically poled lithium niobate," Appl. Phys. Lett. **70**, 3341-3343 (1997).

Chapter 8
Conclusion

Passively mode-locked laser oscillators based on Yb-doped materials provide an ideal platform for delivering extremely short pulses in femtosecond regime. Of particular interest is the generation of multiwatt sub-100 fs pulses, which is still a challenging task today. The work presented in this thesis is devoted to such challenge by developing and investigating a number of high power Yb:KGW bulk oscillators in both CW and mode-locked regimes.

The research was started from addressing two fundamental issues that are critically important in power scaling of the Yb:KGW oscillators. In Chapter 2 we explored the feasibility of an N_m-cut Yb:KGW crystal to achieve reduction of the thermal lensing effect and its potential in producing high power lasers. The proof of principle of the proposed pumping scheme was demonstrated with the development of a diode-pumped laser oscillator based on a 2-mm long N_m-cut Yb:KGW crystal slab. At the pump power of 17.3 W (~7.8 W absorbed), the laser delivered 2 W average output power at 1040 nm. A detailed analysis has shown the reduced strength of the thermal lensing in the N_m-cut Yb:KGW crystal when compared to the previously reported results based on the traditional N_p- or N_g-cut Yb:KGW crystals.

In Chapter 3, we proposed a new technique to characterize the intracavity loss, which is another fundamental factor in determining the performance of a laser. This technique is based on the spectral gain measurement and can be applied to many other broadband quasi-three-level lasers, where the traditional methods are not applicable. Moreover, this technique potentially can be used at any laser output power levels, thus allowing a dynamic optimization of laser performance. Successful experimental demonstration was carried out with a diode-pumped N_g-cut Yb:KGW CW oscillator. A comparison with traditional Findlay-Clay analysis and numerical modeling was also made.

Chapter 4 described the simultaneous dual-wavelength lasing operation observed in a diode-pumped N_g-cut Yb:KGW CW oscillator during the optimization of its performance. Without inserting any optical elements for polarization control, the N_m- and N_p-polarized modes, each of which possessed a distinct wavelength, switched twice and coexisted in two power regimes during the increase of the pump power. The two wavelengths and their separation varied slightly for different output couplings. The wavelength switching and coexistence were studied and explained by considering the thermal and spectral anisotropy of the Yb:KGW crystals, which further led to the polarization-dependent reabsorption loss in the unpumped region of the crystal.

In Chapter 5, I reported on the generation of 67 fs pulses from a diode-pumped mode-locked Yb:KGW bulk laser oscillator. The enhanced performance of this oscillator benefitted from the dual action of Kerr-lens and saturable absorber (KLAS) mode locking. The mode locking was initiated by a SESAM with 2% modulation depth at 1040 nm. With the Kerr lensing effect present, instabilities such as the Q-switched mode locking or multipulse mode locking were suppressed, which led to a stable mode locking with a single pulse inside the cavity. In the single pulse mode-locked regime, Fourier transform-limited pulses with 67 fs duration and 16.8 nm of bandwidth (FWHM) were obtained. The average output power reached 3 W, corresponding to >38 nJ of pulse energy and >570 kW of peak power. To the best of our knowledge, this is the highest average output power produced to date from Yb-ion based bulk lasers with such a short pulse duration.

In Chapter 6, the KLAS mode locking was transferred to Yb:KGW laser oscillators with low repetition rates in order to scale the peak power of the pulses. The 36 MHz oscillator delivered 78 fs pulses with pulse energy of 50 nJ and peak power of 0.65 MW. The cavity was extended by inserting a 1:1 imaging telescope, allowing 85 fs pulses to be generated at a repetition rate of 18 MHz. The pulse energy up to 83 nJ was reached, corresponding to a peak power as high as 1 MW. To the best of our knowledge, this work also for the first time demonstrated sub-100 fs pulses directly from the diode-pumped mode-locked Yb:KGW bulk oscillators operated at a low repetition rate.

Pumping of the optical parametric oscillators (OPOs) with the ultrafast lasers allows generation of the wavelength-tunable pulses in femtosecond regime. In Chapter 7, we theoretically discussed the feasibility of employing new nonlinear crystals, including periodically poled KTiOPO4 (PPKTP) and stoichiometric MgO-doped LiTaO3 (MgO:PPSLT), for optical parametric oscillation pumped by the powerful femtosecond Yb:KGW oscillators developed in this work. The optical, phasematching, wavelength tuning, and dispersive properties of these crystals for parametric interactions are analyzed. The results formed a useful reference for the selection of materials and operating conditions for the practical design of high power femtosecond optical parametric oscillators with excitation at 1 μm.

We believe the performance of the Yb:KGW bulk oscillators based on KLAS mode locking presented in this thesis was limited by the pump power launched into the crystal. As higher pump power becomes available, sub-100 fs pulses with higher average output power and peak power can be expected. Of course, this also necessitates further optimization of the oscillator in both CW and mode-locked regimes. For example, at higher pump power levels, the thermal lensing of the laser crystal will become stronger, leading to a change of the cavity stability regions. Correspondingly, the cavity geometry has to be adjusted to allow the laser to be operated within the stability region. Moreover, stronger Kerr lensing should be introduced to suppress the multipulse mode locking at higher powers. In addition, a thorough investigation on the Kerr-lens sensitivity against the pump power as well as the effect of the fluence on the SESAM would be helpful for the improvement of the lasing performance. The next step could be to experimentally pump the PPKTP and MgO:PPSLT based OPOs with these powerful Yb:KGW femtosecond oscillators. High power sub-100 fs pulses with tunable wavelength in the range of 1.3-1.8 μm are expected to be produced and will be attractive for various applications.

Appendix A

Bulk and thin disk laser geometries

In an end-pumped bulk laser geometry, as shown in Fig. A.1, the crystal is usually wrapped in indium foil and sandwiched between two water-cooled copper or aluminum heat sinks. In such laser system, the pump and the laser beam travel parallel to each other in the crystal. A good spatial overlap between them is one of the critical factors to achieve an efficient lasing process. Typical dimensions of the crystal and the laser beam are also shown in Fig. A.1. In a lasing process, the main portion of the generated heat flows two-dimensionally over the planes perpendicular to the propagation direction of the laser beam. As was explained in Chapter 2, this heat flow forms a temperature gradient inside the crystal, making it to act as a thermal lens. In order to remove the heat load effectively, a thin crystal with ~1 mm thickness is usually used. Depending on the absorption coefficient and the length of the crystal, up to 100% of the pump power can be absorbed in a single pass. To obtain an efficient pumping and lasing, both the pump and the laser beams are tightly focused to a dimension of 100-300 μm in diameter in the crystal.

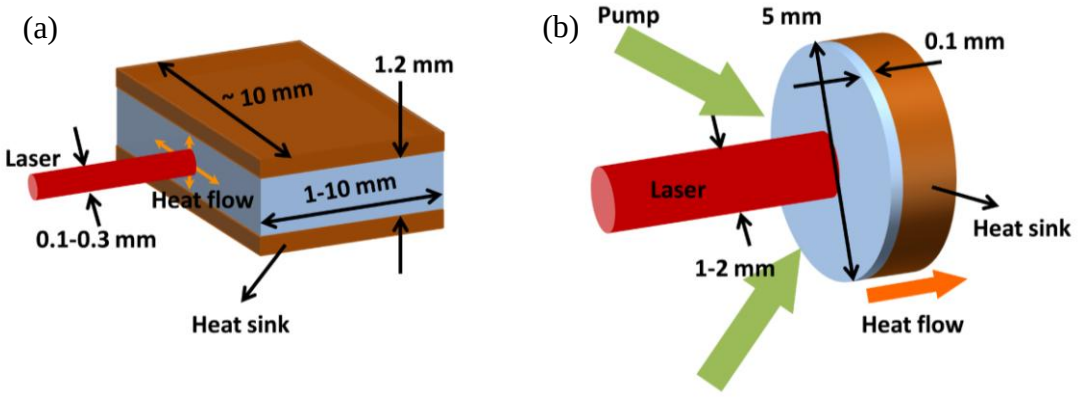

Fig. A.1. Scheme of the bulk (a) and the thin disk (b) laser geometry with typical dimensions.

The thin disk laser geometry, which was firstly demonstrated by Giesen in 1993, recently has also been widely employed for the generation of high power lasers in both CW and pulsed regimes [1]. In such a laser system, the crystal is shaped as a very thin disk with 100-200 μm of thickness and is usually mounted or glued on a water-cooled copper heat sink. This allows the generated heat in the lasing process to be removed efficiently. The heat flows coaxially along the propagation direction of the laser beam, therefore forming a one-dimensional temperature gradient. On the other hand, the surface of the crystal has a uniform temperature and hence less deformation. Therefore, the thin disk geometry suffers less from thermal issues when compared to the bulk laser geometry.

The crystal is usually AR-coated on the front surface and HR-coated at the back surface (contacts to the heat sink) at both of the pump and the laser wavelength. The pump radiation incident into the crystal will be reflected from the back surface. However, due to the short travel distance of the pump in the crystal, only a small amount of pump power can be absorbed in a single reflection. In order to achieve an efficient absorption, the pump radiation usually recycled to have multiple reflections in the crystal, which requires a complex design of the pump system. This is a disadvantage of using the thin disk laser geometry.

For the laser beam, the lasing process with a single reflection in the crystal requires an output coupling with low transmission to reach high round-trip gain. Therefore, the intracavity loss (Chapter 3) needs to be considered carefully and be kept at very low level. In some cases, output coupling with high transmission was used to extract more power (or energy) from the cavity [2-3]. However, complex cavities were needed to allow the laser beam to be reflected multiple times through the crystal in one round-trip. Power scaling of the thin disk lasers can also be achieved by proportionally increasing the pump and laser beam spots (typically 1-2 mm) incident onto the crystal.

Appendix B

Ray transfer matrix

For a Gaussian beam, its radius *w(z)* and wavefront radius of curvature *r(z)* can be integrated into the so-called complex q parameter, which can be expressed as the following:

$$\frac{1}{q(z)} = \frac{1}{r(z)} - \frac{i\lambda}{\pi w(z)^2}. \tag{B-1}$$

As a Gaussian beam travels through an optical component, the q parameters of the input and output beams are related by:

$$q_{out} = \frac{q_{in}A + B}{q_{in}C + D}, \tag{B-2}$$

where A, B, C, and D are the four elements of the ray transfer matrix $\begin{pmatrix} A & B \\ C & D \end{pmatrix}$ of the optical component. The following lists the matrices of some important optical components used in this work.

Propagation in free space	$\begin{pmatrix} 1 & d \\ 0 & 1 \end{pmatrix}$	d is the distance
Propagation in the crystal	$\begin{pmatrix} 1 & l_c/n \\ 0 & 1 \end{pmatrix}$	l_c is the crystal length n is the refractive index
Reflection from flat mirror	$\begin{pmatrix} 1 & 0 \\ 0 & 1 \end{pmatrix}$	
Reflection from concave mirror	$\begin{pmatrix} 1 & 0 \\ 2/r & 1 \end{pmatrix}$	r is the radius of curvature, $r<0$
Thermal or Kerr lens	$\begin{pmatrix} 1 & 0 \\ -2/f & 1 \end{pmatrix}$	f is the focal length, $f>0$

Appendix C

Sellmeier equation and thermal expansion equation

The Sellmeier equation describes the wavelength dependence of the refractive indices of the crystals. Since the refractive indices also change with the crystal temperature, a temperature corrected Sellmeier equations should be used. The following section lists wavelength and temperature dependent Sellmeier equations for extraordinary axes of MgO:PPcLN, MgO:PPSLT and PPKTP crystals.

Sellmeier equation for MgO:PPcLN [4]:

$$n_e^2(\lambda,T) = a_1 + b_1 f(T) + \frac{a_2 + b_2 f(T)}{\lambda^2 - [a_3 + b_3 f(T)]^2} + \frac{a_4 + b_4 f(T)}{\lambda^2 - a_5^2} - a_6\lambda^2, \qquad \text{(C-1)},$$

where *f(T)* is the temperature correction term which is expressed as:

$$f(T) = (T - 24.5)(T + 570.82). \qquad \text{(C-2)}$$

Other parameters are listed in Table C.1.

Table C.1. Sellmeier equation coefficients for MgO:PPcLN

a_1	a_2	a_3	a_4	a_5	a_6	b_1	b_2	b_3	b_4
5.756	0.0983	0.2020	189.32	12.52	1.32×10^{-2}	2.860×10^{-6}	4.7×10^{-8}	6.113×10^{-8}	1.516×10^{-4}

Sellmeier equation for MgO:PPSLT [5]:

$$n_e^2(\lambda,T) = a_1 + \frac{a_2 + f_1(T)}{\lambda^2 - [a_3 + f_2(T)]^2} + \frac{a_5}{\lambda^2 - a_6^2} + \frac{a_7}{\lambda^2 - a_8^2} + a_4\lambda^2. \qquad \text{(C-3)}$$

The temperature correction term $f_1(T)$ and $f_2(T)$ are expressed as

$$f_1(T) = \alpha(T + 273.15)^2, \quad f_2(T) = \beta(T + 273.15)^2. \qquad \text{(C-4)}$$

The parameters used are listed in Table C.2.

Table C.2. Sellmeier equation coefficients for MgO:PPSLT

a_1	a_2	a_3	a_4	a_5	a_6	a_7	a_8
4.528254	0.012962	0.242783	-0.02288	0.068131	7.061878	1.307470	7.061878
α		3.483933×10^{-8}		β		1.607839×10^{-8}	

Sellmeier equation for PPKTP [6-7]:

$$n_e(\lambda,T) = n_e(\lambda) + n_1(\lambda)(T-25) + n_2(\lambda)(T-25)^2, \tag{C-5}$$

$$n_e^2(\lambda) = a_1 + \frac{a_2}{1-\frac{a_3}{\lambda^2}} + \frac{a_4}{1-\frac{a_5}{\lambda^2}} - a_6\lambda^2, \tag{C-6}$$

$$n_1(\lambda) = \sum_{m=0}^{3}\frac{b_m}{\lambda^m}, \quad n_2(\lambda) = \sum_{m=0}^{3}\frac{c_m}{\lambda^m}. \tag{C-7}$$

The parameters used are listed in Table C.3.

Table C.3. Sellmeier equation coefficients for PPKTP

a_1	a_2	a_3	a_4	a_5	a_6
2.12725	1.18431	5.14852×10^{-2}	0.6603	100.00507	9.68956×10^{-3}
b_0		b_1	b_2		b_3
9.9587×10^{-6}		9.9228×10^{-6}	-8.9603×10^{-6}		4.1010×10^{-6}
c_0		c_1	c_2		c_3
-1.1882×10^{-8}		10.459×10^{-8}	-9.8136×10^{-8}		3.1481×10^{-8}

Thermal expansion equation

Since the thermal expansion of the crystals would affect the poling periods, which in turn changes the output wavelength from the OPO system, it also should be considered in the calculations. The thermal expansion equation can be expressed as:

$$\Lambda(\Lambda_0,T) = \Lambda_0[1+\alpha(T-T_0)+\beta(T-T_0)^2], \tag{C-8}$$

where Λ_0 and T_0 are the initial poling period and temperature. The thermal expansion coefficients α and β for different crystals are listed in Table C.4.

Table C.4. Thermal expansion coefficients

	α	β	reference
MgO:PPcLN	1.54×10^{-5}	5.3×10^{-9}	[4]
MgO:PPSLT	1.6×10^{-5}	7×10^{-9}	[8]
PPKTP	6.7×10^{-6}	11×10^{-9}	[6]

References

[1] A. Giesen, H. Hügel, A. Voss, K. Wittig, U. Brauch, and H. Opower, "Scalable concept for diode-pumped high-power solid-state lasers," Appl. Phys. B **58**, 365-372 (1994).

[2] J. Neuhaus, J. Kleinbauer, A. Killi, S. Weiler, D. H. Sutter, and T. Dekorsy, "Passively mode-locked Yb:YAG thin-disk laser with pulse energies exceeding 13 μJ by use of an active multipass geometry," Opt. Lett. **33**, 726-729 (2008).

[3] J. Neuhaus, D. Bauer, J. Zhang, A. Killi, J. Kleinbauer, M. Kumkar, S. Weiler, M. Guina, D. H. Sutter, and T. D ekorsy, "Subpicosecond thin-disk laser oscillator with pulse energies of up to 25.9 microjoules by use of an active multipass geometry," Opt. Express **16**, 20530-20539 (2008).

[4] D. H. Jundt, "Temperature-dependent Sellmeier equation for the index of refraction, n_e, in congruent lithium niobate," Opt. Lett. **22**, 1553-1555 (1997).

[5] V. Z. Kolev, M. W. Duering, and B. Luther-Davies, "Corrections to refractive index data of stoichiometric lithium tantalate in the 5-6 μm range," Opt. Lett. **31**, 2033-2035 (2006).

[6] S. Emanueli and A. Arie, "Temperature-dependent dispersion equations for $KTiOPO_4$ and $KTiOAsO_4$," Appl. Opt. **42**, 6661-6665 (2003).

[7] K. Fradkin, A. Arie, A. Skliar, and G. Rosenman, "Tunable midinfrared source by difference frequency generation in bulk periodically poled $KTiOPO_4$," Appl. Phys. Lett. **74**, 914-916 (1999).

[8] A. Bruner, D. Eger, M. B. Oron, P. Blau, M. Katz, and S. Ruschin, "Temperature-dependent Sellmeier equation for the refractive index of stoichiometric lithium tantalate," Opt. Lett. **28**, 194-196 (2003).